Faculty of Mechanical Engineering,
High Tech Systems & Materials

Influence of print speed on the microstructure and mechanical properties of AA6060 FSEAM builds

D.H. Strik

M.Sc. Thesis
March 16, 2023

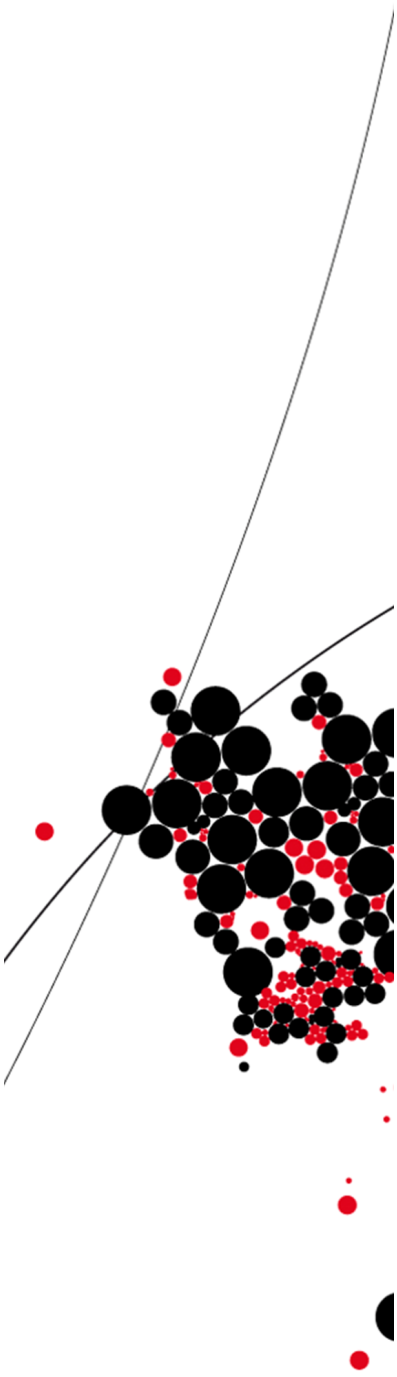

The committee:
dr. ir. T. C. Bor
dr.ir. L. Warnet
dr. D.T.A. Matthews
S. Sayyad Rezaeinejad MSC

Production Technology Engineering Group
Faculty of Mechanical Engineering
University of Twente

Aknowledgement

Throughout my thesis I received support from many people. I would like to take this opportunity to express how thankfull I am for receiving their help.

Staring with my supervisor Ton Bor, who I would like to thank for all the constructive feedback, on the writing and the thermal model in particular. I always felt free to ask questions and address situations which were troubling me, and I am really grateful for it. Besides, I can only admire the enthusiasm about the process, every time a small step forward is taken.

Additionally, I would like to express my gratitude to Saed Sayyad Rezaeinejad for supporting me during the experiments and the experimental analysis. Without his help I would not have been able to gather this many results, and I value the subtle hints in which direction I had to think to set the next step.

Next, I would like to thank all the members of the horst workshop staff. Who have helped me countless times with reproducing or fixing parts of the FSEAM setup to get it up and running again.

In the sample analysis I received a lot of help and knowledge from the supporting staff, Nick and Bert. Both have guided me in the usage of many machines in the production technology labs and where always available to answer my questions.

I would also like to express my gratitude to the examination committee for their invested time and effort.

Finally, I would like to thank my friends and family. Especially my roommates, who have helped me check the writing of my thesis.

Summary

Additive manufacturing using aluminium can be a valuable technology in industries that require lightweight parts, such as aerospace and automotive. However, state-of-art approaches that involve melting the feedstock material pose a challenge for many aluminium alloys due to metallurgical problems that occur during the melting and solidification phases. A solid-state approach that avoids the liquid phase and related problems is a potential solution.

Within the Production Technology chair, a new solid-state process has been developed, called Friction Screw Extrusion Additive Manufacturing (FSEAM). It employs a rotating screw in a stationary housing to deposit aluminium feedstock at much lower temperatures providing a fine-grained microstructure without porosity for a broad range of alloys. However, the influence of various parameters on microstructure and mechanical properties is still unknown. This work focuses on the effect of printing speed during manufacturing.

Four builds were successfully produced of AA6060 T6 with printing speeds of 100, 150, 200, and $250\,\mathrm{mm/min}$. The average temperature at the print head increased with printing speed. No macro-scale defects were observed, but SEM microscopy showed the presence of micro-scale defects. Furthermore, EBSD revealed substantial grain refinement for all samples.

The builds' hardness decreased by about 50% compared to the feedstock material. Tensile tests showed a decrease in yield and tensile strength

but an increase in elongation at break after the additive manufacturing process. Tensile strength tended to increase with print speed. The mechanical properties differed significantly between samples extracted in the build and deposition directions. The former often showed premature failure related to unfavorable micro-scale defects, while the latter displayed consistent and relatively large ductility values, hardly or not affected by defects. Further process improvement is required to prevent interfacial defects and improve interlayer bonding.

A closer look at the stress-strain curves from builds with an average build temperature above $400\,^{\circ}\mathrm{C}$ (150-$250\,\mathrm{mm/min}$) revealed serrated stress-strain behavior in the plastic region. This behavior was ascribed to the dissolution of strengthening precipitates at elevated temperatures within the print head during deposition, with only partial recovery occurring in the subsequent deposition process.

Lastly, a 2D thermal model of the build was developed to gain a better understanding of the builds' thermal history. The model calculations confirmed the impact of deposition speed on heat generation and temperature development.

Contents

List of acronyms

FSEAM	Friction Screw Extrusion Additive Manufacturing
FSW	Friction Stir Welding
FSP	Friction Stir Processing
FSC	Friction Stir Cladding
FSE	Friction Stir Extrusion
FSAM	Friction Stir Additive manufacturing
FS	Friction Surfacing
AFSD	Additive Friction Stir Deposition
SEM	Scanning Electron Microscopy
EBSD	Electron Backscatter Diffraction
ECD	Equivalent Circle Diameter
SEM	Scanning Electron Microscopy
EDX	Energy Dispersive X-Ray Analysis
DSA	Dynamic Strain Aging

Chapter 1

Introduction

Friction Screw Extrusion Additive Manufacturing (FSEAM) is an additive manufacturing technique for printing aluminium alloys, currently being researched at the University of Twente. This chapter will discuss the potential value of FSEAM, and the work presented on the impact of building speed on microstructure and mechanical properties of the material. Previous work will be discussed and a research question and strategy will be formulated.

1.1 Motivation and Framework

Additive manufacturing is a production technique where 3-dimensional structures are build layer by layer. Overall, additive manufacturing is known for advantages such as reduction of waste material and parts for assembly, no need for expensive tooling, production of intricate parts, and shorter time to market [1]–[3]. Applying additive manufacturing with aluminium could be of great use in fields with a need for lightweight parts such as aerospace and automotive [1], [3]. Aluminium additive manufacturing methods can be classified into fusion and solid state-based processes. The fusion based processes bind layers by melting the material, whereas solid-state processes remain below melting temperatures. Solid state processes are divided by mechanical deformation and sinter based methods, with the binding energy being

provided through kinetic energy for the first, and thermal input for the latter [2], [4]. A structured overview of the classifications and the corresponding manufacturing methods is provided in Figure 1.1.

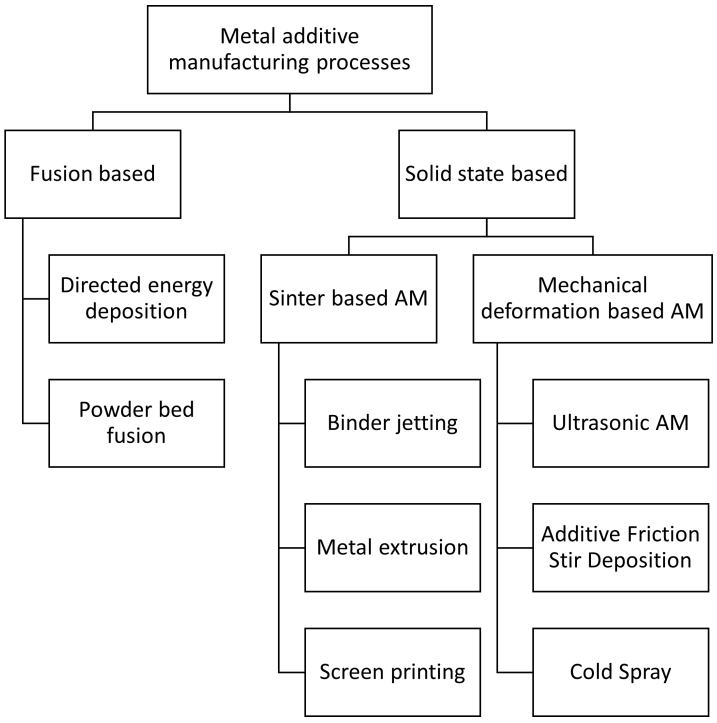

Figure 1.1: Overview of metal additive manufacturing methods [2]

The first approaches to metal printing were fusion-based processes such as directed energy deposition and powder bed fusion [5]. The feed stock material of these methods is often a powder, which is deposited and melted with a laser or electron beam to fuse with the previous layer. Challenges arise in the phase transformation from solid to liquid and back. Examples of these challenges are large columnar grains upon solidification, few available feed stock alloys, loss of elements through vaporisation, porosity and lack of fusion defects, cracking and delamination, mechanical anisotropy, and residual stresses [1]–[3], [6]–[9].

One way to solve these problems is by shifting to a solid-state approach. Previous research by the Production Technology chair of the University of Twente showed good results with friction surface cladding and extrusion [10]. This sparked interest in extending this method to additive manufacturing with a similar approach, which is called Friction Screw Extrusion Additive Manufacturing (FSEAM). Some successful experiments with AA6060 T6 have been performed [11], [12], demonstrating grain refinement and porosity-free parts. AA6060 T6 is an aluminium and magnesium silicide alloy, which is in its peak aged state, more details about this material and the state are given in Section 2.1.

In addition, the FSEAM process is performed at much lower temperatures, removing the melt-based defects and opening up more options for alloy types, resulting in promising production technology. However, the influence of different process conditions on the mechanical properties is still unknown. Therefore, more research needs to be done, to fully understand what happens during the fabrication of a structure and how the printing process can be influenced to obtain the best mechanical properties.

1.2 Background

To get a better understanding on the previous findings, the basics of the FSEAM process have to be explained first. The material is pressed onto a rotating tapered screw; due to friction, the material is heated and moved downwards by the screw where it is deposited onto a substrate. When the table on which the substrate is mounted is moved, structures can be made in an additive manufacturing fashion. A schematic overview of the system and its process parameters is given in Figure 1.2.

The process parameters that can be influenced are the rotational speed of the tool (ω_{tool}) and the feed rate (V_{feed}), which is the speed at which the material is fed into the system. Furthermore, the table speed (V_{table}), at which a new layer is deposited, and the tool gap (h_{TG}), which is the space between the extrusion chamber wall and the rotating screw. Two forces are measured during the process, the feed force (F_{feed}) and the normal

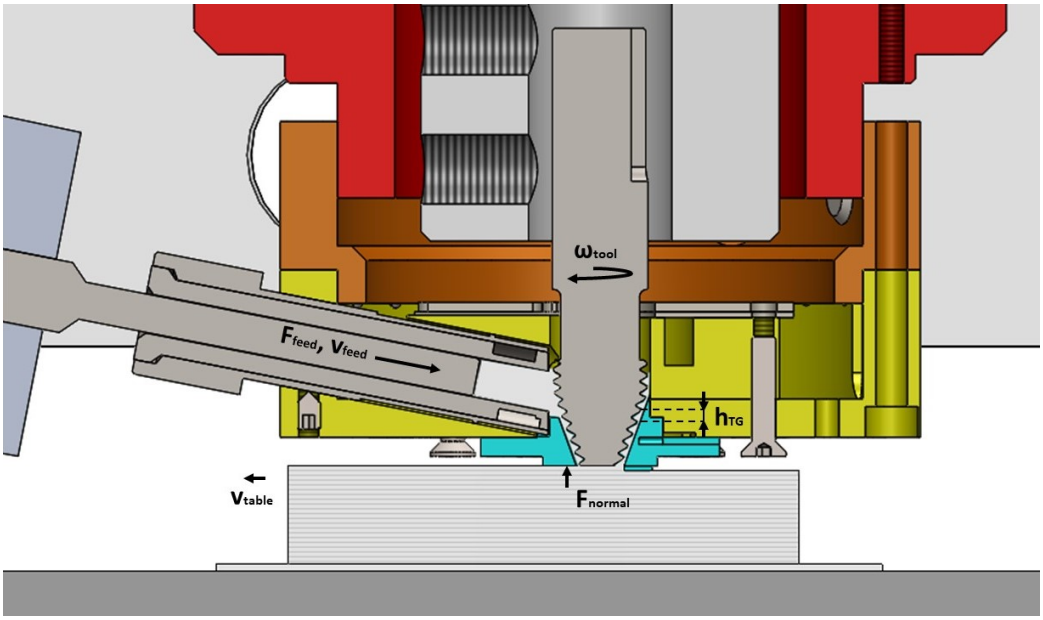

Figure 1.2: Process overview (ω_{tool} = Rotational speed, h_{TG} = tool gap, V_{feed} = Material feed rate, F_{feed} = Feed force), V_{table} = Table speed, F_{normal} = Normal force)

force (F_{normal}). They are influenced by the above mentioned process parameters and are recorded to give an in-situ indication of what happens during the manufacturing process. The feed force is related to the feed rate, while the normal force is related to a combination of the feed rate, the height of the newly printed layer, and the speed of the table. Chapter 3 will give more details about the setup.

In previous work of R. Ariës some successful builds have been made at low table speeds ranging between 50-65 mm/min. An example of these builds is given in Figure 1.3. An important result of the research is the influence of the material feed rate in porosity-free printing, which is one of the advantages of FSEAM over melt-based processes. By overfeeding the material by 25-30%, virtually no porosity is found in the part employing the current setup [12]. This means that 25-30% more material is added than is required for the desired dimensions of the print. In a later

study by V. Dolas, this has been confirmed for table speeds between 50 and $490\,\mathrm{mm/min}$ [11]. Both studies are carried out with AA6060 T6, which is used in this research as well.

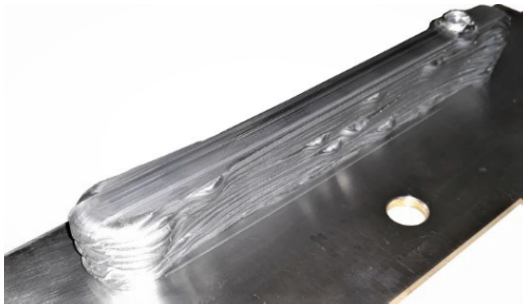

Figure 1.3: FSEAM build with a low table speed [13]

Based on previous work by N. Masselink some additional assumptions can be made. Starting with the influence of the tool gap on the tool torque and feed force. A larger tool gap gives more space for the material, and therefore a lower force is necessary to push the material in. However, the tool torque will rise since more material has to be transported at once [13].

Second, the importance of the water cooling of the material feed. This cooling keeps the temperature low enough to prevent plastic deformation in the feed tube [13]. If the temperature rises too much, the feed material deforms laterally under the influence of the feed force preventing further feed material movement in the feed tube.

Next to print experiments, extrusion experiments have been performed with roughly the same setup, as can be seen in Figure 1.4. Some useful trends can be recognised in these extrusion experiments. Starting with the material feed rate, it was observed that in extrusion the grain size increases with increasing material feed rate, independent of the rotational range of the tool used [13], [14]. Since small grains are preferred, explained in more detail in Section 2.1, it is wise to use a lower material feed rate. However, feedtube jamming may occur at very low feed rates,

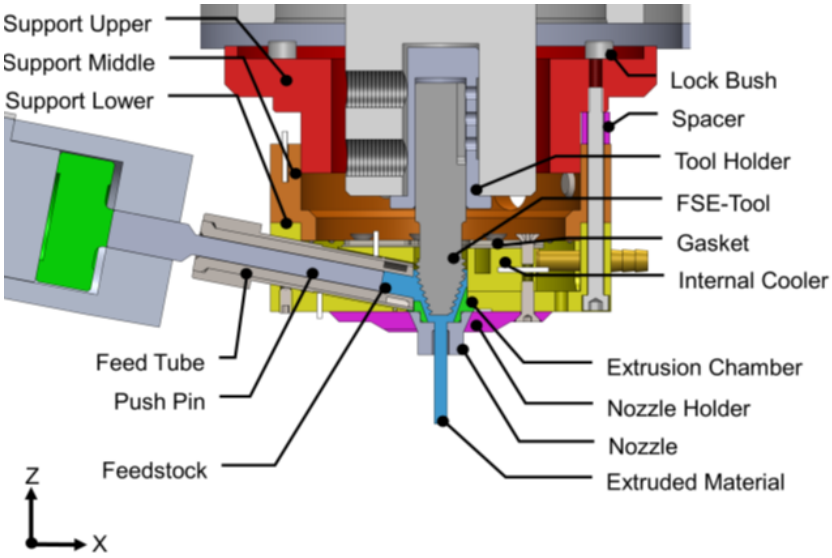

Figure 1.4: Friction screw extrusion head [13]

and low print speeds result in an unwanted long process time.

In the hardness test, the opposite seems to be true. The hardness of the material decreased less with increasing material feed rate [13], [14]. Comparing the extruded material to the feedstock the hardness decreased for all experiments. However, at a higher feed rate the extrudate is less influenced by the effects of heat. This is probably related to the heating time. For a shorter time at elevated temperatures, more precipitates remain within the material, reducing the material hardness less. More information about precipitates will be given in section 2.1.1.

1.3 Research questions

This research focuses on print velocity as the variable parameter during the manufacturing process. Therefore the research question is defined as follows: What influence does the print speed have on the microstructure and mechanical properties of FSEAM builds made from AA6060 T6?

An answer will be formulated based on the following steps:

- Perform a literature study on friction stir processes and, in particular, similar additive manufacturing approaches.
- Set up and perform an experimental approach to find a correlation between the mechanical properties, microstructure, and print velocity.
- Support the experimental outcome with a thermal model of the builds.

1.4 Report organisation

In Chapter 2, a literature research is performed to get a better understanding of the material processes which can occur during the build, to answer the research questions above. Additionally, comparable production methods are reviewed to gain some insight in the current status of similar processes. Next, an experimental plan is constructed, in Chapter 3, to print the samples and review the microstructure and mechanical properties. Then, in Chapter 4 an overview of the results combined with a discussion of the results is presented. After the experimental research, a simplified thermal model of a sample during the build is elaborated in Chapter 5. Afterwards, in Chapter 6, a conclusion will be made about the overall results.

Chapter 2

Literature overview

To gain insight into existing friction stir processes and the behavior of aluminium in general, a literature study was performed. In this chapter an overview is given of the microstructure development of aluminium and how it can be influenced. Next, solid-state processes in general are discussed and other friction stir processes are highlighted.

2.1 Microstructure development

As mentioned in the introduction, this research is focused on the additive manufacturing of aluminium. Aluminium is a crystalline material, which means its atoms are ordered in a repeating lattice pattern, called a crystal structure [15], [16]. These crystal structures are rarely perfect and contain multiple types of defects. These defects are able to move through the lattice under certain circumstances, which are discussed later in this section. The movement of these defects within the microstructure plays an important role in the microstructure development and the mechanical properties. To understand this role, different types of defects are discussed first.

The defects can be subdivided in three categories; point defects, dislocations, and grain boundaries [15]. From all categories, one example is highlighted. Starting with the category point defects, a vacancy is

discussed. In Figure 2.1a, it can be seen that one atom is missing in the crystal structure, this is called a vacancy. Due to the gap in the lattice the other atoms are pulled toward each other, creating a tensile strain field [15]. Next, an example of an edge dislocation is seen in Figure 2.1b, where an entire row of atoms is misaligned. Last, grain boundaries in Figure 2.1c. Grain boundaries are formed because the orientation of the lattice structure differs from that of the surrounding lattices [15]. A grain is never aligned with its neighbor. At the interface between these grains, a grain boundary is formed.

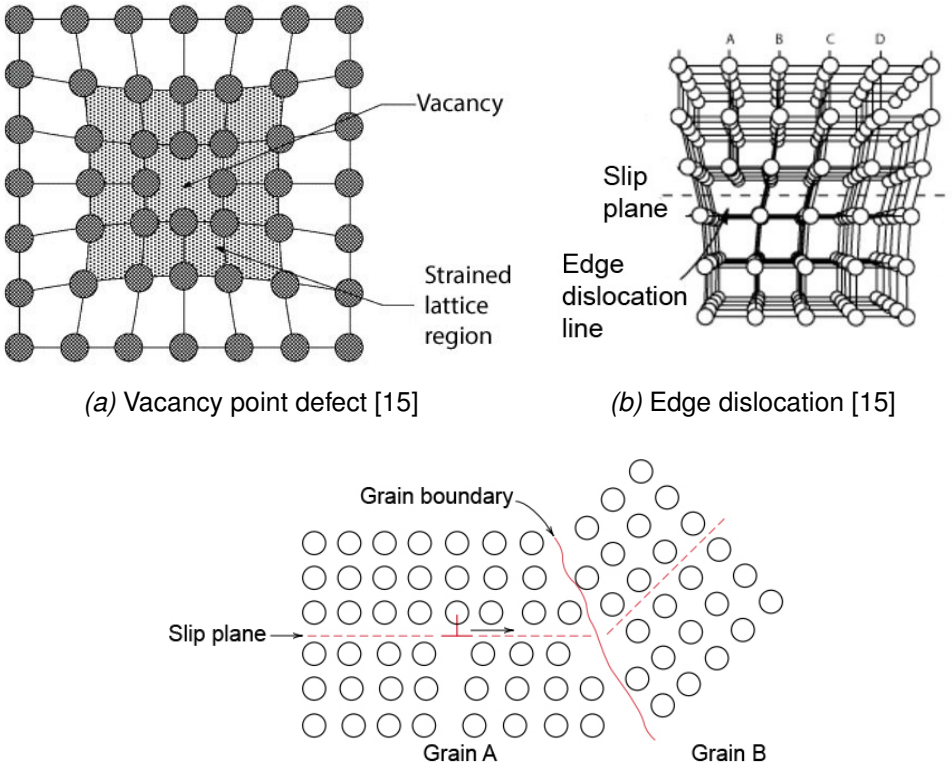

(a) Vacancy point defect [15]

(b) Edge dislocation [15]

(c) Grain boundary [17]

Figure 2.1: Examples of crystal structure defects

Movements of the defects are caused by diffusion, where single atoms move to an adjacent location, pushing the dislocation forwards. Edge dislocations for example, where a shear stress can cause a wave of

motion that transports the dislocation to the end of the lattice. In Figure 2.2 a schematic overview is provided.

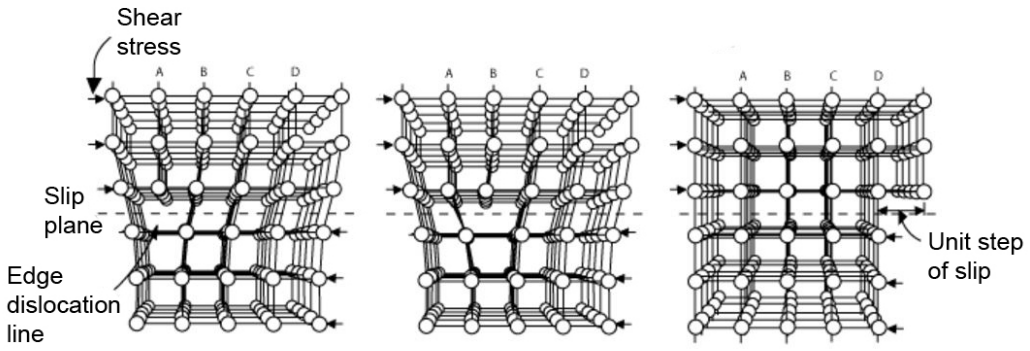

Figure 2.2: Plastic deformation based upon the movement of a dislocation line through the lattice [18]

Diffusion takes place once the following two conditions are met; a vacancy is present in an adjacent side, and the atom has enough energy to break the existing bonds with its neighbouring atoms [17]. The energy of an atom can be expressed in the amount of vibration in place. This vibration becomes larger at elevated temperatures, making it easier for an atom to diffuse.

2.1.1 Hardening

Pure aluminium is not necessarily useful for structural applications, as it is very soft and ductile [19]. The lack of strength in the material can be explained by plastic deformation due to movement of defects in the crystal structure. The more plastic deformation is possible in a crystal structure, the more elongation of the material can take place. However, the strength of the material will be reduced due to these movements [15], [16]. To improve the strength of the material, these movements should be restricted [15], [17]. This can be achieved with multiple types of hardening. Some common types of hardening are listed and discussed down below:

- Strain hardening
- Grain refinement hardening
- Precipitate hardening
- Solid solution hardening

Strain hardening

Strain hardening occurs through plastic deformation, needing a high dislocation density. Strength is gained by the interaction between the dislocations, limiting each others movement [15]. Dislocations are surrounded by a strain field that repels other dislocations. Therefore, these strain fields stop the movements of other dislocations once they are in close contact. The more dislocations are stopped in their movement, the more strength is necessary to plastically deform the material, resulting in higher strength. However, there is a limit to which this applies. A lot of dislocations pilling up in a small location make a material brittle, and can cause cracks [15].

Grain refinement hardening

Grain refinement hardening is based upon the grain boundaries, which is one of the defects mentioned in Section 2.1. These boundaries provide strength because they impede the movement of dislocations. The movement is restricted due to the different orientations of the crystals, disrupting the slip plane, as depicted in Figure 2.1c. The slip plane has to change its direction of motion to move on to the next grain, making the movement more difficult and temporarily bringing the dislocation movement to an end, strengthening the material [17].

Besides, a repulsive strain field is created by the boundary, which stops the dislocation before reaching the boundary. Once more dislocations have moved near the grain boundary, a cluster of dislocations is formed. All these dislocations create their own repulsive strain field as well, and eventually the strain field of the dislocations becomes large enough to

overcome the strain field created by the grain boundary. Moving one dislocation to an adjacent grain. The pillage of dislocations, which is necessary to overcome the strain field of the grain boundary, causes hardening [15].

Overall, grain refinement hardening benefits from small grains, because smaller grains have a higher boundary-to-volume ratio. The more grain boundaries are present in a volume, the earlier the dislocation movements are stopped resulting in a stronger material [15], [20]. A remark has to be made here. Since, in precipitation-based aluminium alloys like AA6060, the effect of precipitate hardening is usually much larger than the effect of the grain size.

Precipitate hardening

The material strength can be increased by additives as well, alloying elements can be used to increase the strength via precipitate hardening. In the AA6XXX series magnesium and silicon are added, which offer qualities such as better corrosion resistance, surface finish, formability, and increased strength. These qualities make the material a good fit for extrusion [21], and thus FSEAM.

These alloy elements can form magnesium silicide (Mg_2Si) particles in the aluminium, providing strength [21]. These particles are known as precipitates and are small particles unmixed from the overall solution of the alloyed material. They give extra strength to the material because they hinder the motion of dislocations. However, these precipitates have multiple stages. The state of the precipitate tells something about the amount of hindering that takes place, and thus the added strength.

The presence or absence of these precipitates can be explained by the phase diagram. In Figure 2.3 the phase diagram of aluminium and magnesium silicide can be found. The dotted line indicates AA6060, which is the feedstock material used for this research. The phase diagram will be explained from the top of the dotted line to the bottom.

Starting in the liquid region (L), the temperature is above the melting point ($T > T_{melt}$) and the material consists of a homogeneous liquid. If the temperature is decreased, the alloy passes through multiple region. The $\alpha + liquid$ region, the solid solution region α, and finally below the blue solvus line: the $\alpha + Mg_2Si$ region. In this last region, precipitates of Mg_2Si are formed, represented by small stripes in Figure 2.3. Precipitation occurs because the material has a decreasing mixability when the temperature is reduced [16]. In the phase diagram, this is indicated by the solvus line, which is the blue line in Figure 2.3.

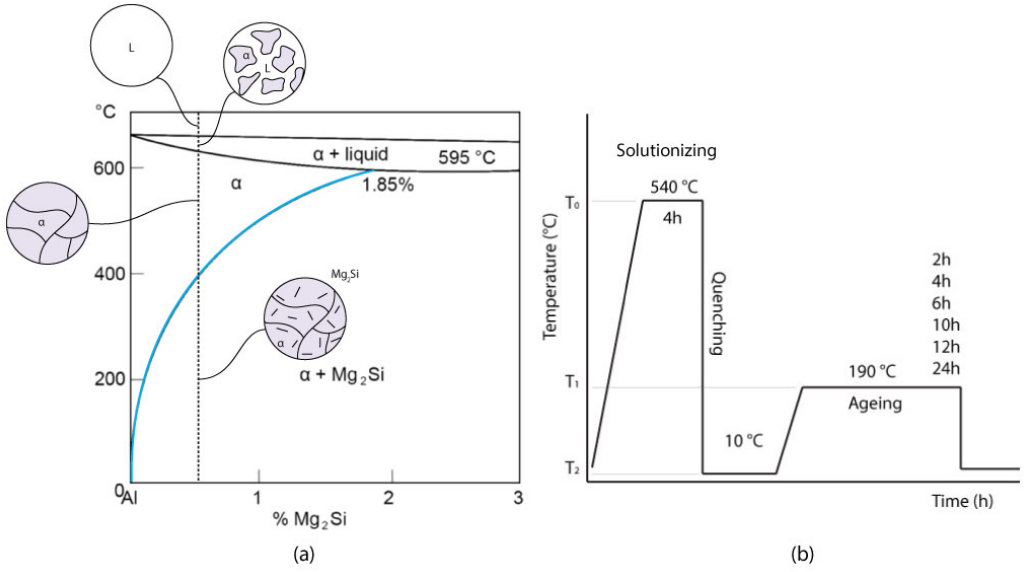

Figure 2.3: Phase diagram (left) [22] and the schematics of heat treatment stages (right) [23] of the Aluminium 6XXX series

If the material is kept in the $\alpha + Mg_2Si$ region at T_1, the diffusion rate is high and Mg_2Si particles can form precipitates. The higher the temperature, the faster this diffusion takes place. The longer the material is kept at an elevated temperature, the larger the precipitates become, and the lower the amount of precipitates in the material becomes. The size of the precipitate tells something about its state and thus its strength since precipitates can be divided into different categories; underaged,

peakaged, and overaged precipitates [24]. These categories are depicted in Figure 2.4. As can be deduced from the name, peak-aged precipitates give the highest strength and are therefore desired in a material. Large precipitates are overaged, which can only be reversed by crossing the solvus line into the solid state, where all the alloying elements are dissolved and the process starts from zero. If a material is underaged, however, it is possible to artificially age the material even further.

Artificial ageing is a heat treatment in which the material is heated to the solid solution phase (T_0) and is kept there for some time to fully solutionize. The material is then quenched to room temperature or below (T_2), resulting in a material without precipitates. This is called a supersaturated solid solution, where the magnesium and silicon atoms had no time to depart from the solid solution at elevated temperatures. By reheating the material up to T_1, precipitates start to grow and the precipitates can be aged to the desired state [25]. The process is schematically displayed in Figure 2.3 on the right. If a material is still in the underaged state, T4 for example, the ageing step without solutionizing can be used to reach the peak aged state at T6.

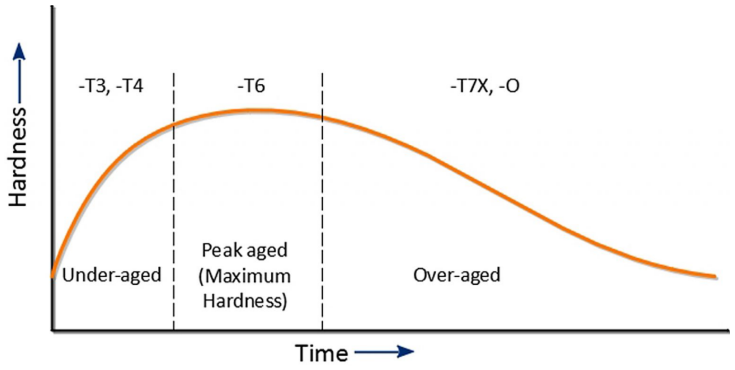

Figure 2.4: Artificial ageing curve for Aluminium [25]

Solid solution hardening

Another strengthening mechanism which makes use of alloying elements is solid solution hardening. The alloying elements add strength by

dissolving in the aluminium and taking the place of a vacancy in the crystal structure [15]. In Figure 2.5, a schematic overview is given of alloying atoms in a vacancy.

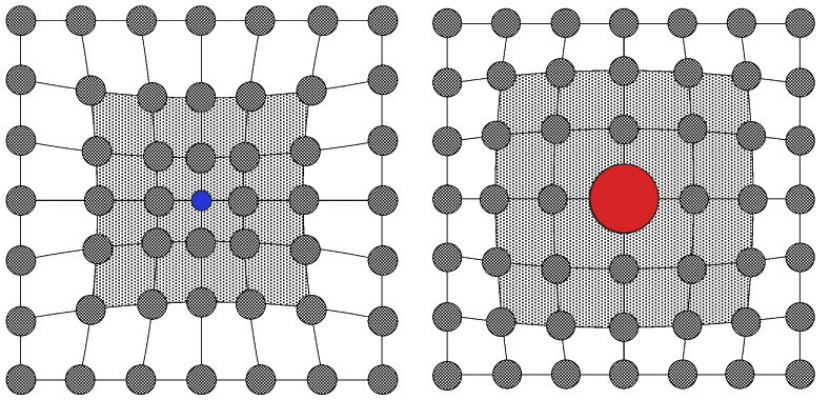

Figure 2.5: Example of alloying atoms in place of a vacancy [15]

Once these vacancies are taken by alloying elements, the localized strain changes. This is caused by the alloying atoms being either larger or smaller than the matrix atoms, which distorts the lattice [15]. A larger atom creates a compressive strain field, pushing the matrix atoms apart. While a smaller atom pulls the matrix atom towards each other, creating a tensile strain field. These strain fields are called lattice strains and both types are depicted by the grey areas in Figure 2.5. Dislocation movements are either attracted or repelled by the lattice strains, causing the strain to work as a barrier. Since the movement of the dislocations gets restricted, hardening takes place. A remark has to be made, since the alloying elements should remain within the aluminium lattice. A look at the phase diagram, in Figure 2.3, shows that the material ends up in the $\alpha + Mg_2Si$ region when cooled down to room temperature. Indicating that the atoms want to diffuse out of the lattice. In order to prevent this, the material should be cooled down fast, to a temperature in which diffusion becomes difficult.

2.1.2 Annealing

Oppose to the previous mentioned hardening methods which store internal energy, annealing is a thermal process which lowers the energy of a material. Defects raise the internal stored energy, and plastic deformation increases the dislocation density, resulting in thermodynamically unstable microstructures after processing[26]. The internal energy can be lowered by processes like recovery, recrystalisation, and grain growth [17], [26]. These processes may follow each other in the given order, as seen in Figure 2.6, but they can occur separately as well. All processes are explained in more detail down below.

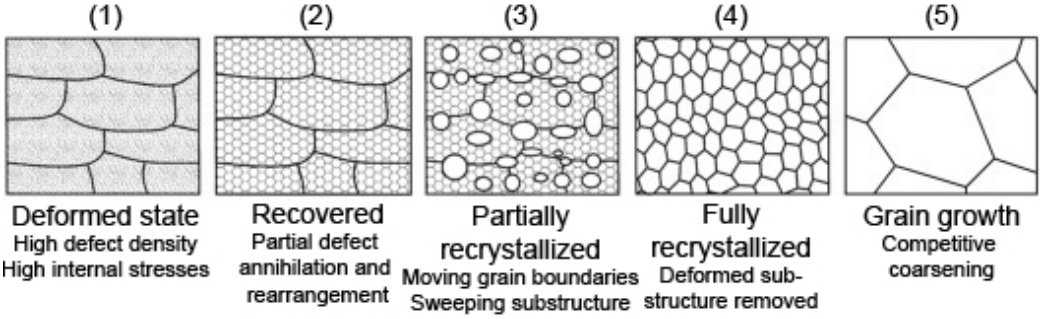

Figure 2.6: Schematic overview of the microstructure evaluation during annealing, including recovery, recrystallisation and grain growth [27]

Recovery

In recovery, dislocation movements take place in rest, to lower part of the internally stored energy [17]. That is, no external stresses are applied to the material. This occurs at elevated temperature, speeding up the diffusion process. During recovery the material seeks to release some internally stored energy. Therefore, dislocations diffuse to create the lowest possible strain field without grain boundary migration, resulting in a small reduction in the number of dislocations [17], [26].

Recrystallisation

While recovery lowers internal energy, a lot of strain is still present in the material. Therefore, another process can take place, called recrystallisation. In this process, nuclei are formed, which are the start of new grains. These nuclei are formed at defects in the crystal structure, preferable grain boundaries [17]. They grow into new grains with a low dislocation density, lowering the overall internal energy of the material. The new grains start very small and grow until the old grains have been replaced, see Figure 2.6 (3) and (4). The driving force of this process is the energy difference between the old and the new grains. The new grains store less strain, which favors the growth of new grains over the old strained grains.

The degree at which recrystalisation takes place depends on both time and temperature. For higher temperatures nuclei form faster and the diffusion rate is higher, resulting in a higher rate of recrystalisation [17]. Another factor which influence the recrystallisation rate is the dislocation density. The more dislocations are present, the higher the recrystalisation rate. Meaning the recrystalisation starts at a lower temperature. However, there is a limited temperature value, even for high dislocation densities, which lays around half of the melt temperature [17].

Grain growth

Last in line is grain growth. Grain boundaries create free energy within the material, resulting in a higher total energy. Since large grains result in fewer grain boundaries and thus less free energy, the material will strive to form larger grains [16], [17]. A single grain is able to grow by diffusing atoms from the neighboring grains. Because the atoms leave the neighbouring grains, the smaller grains will shrink until only large grains remain. Resulting in a material with less but larger grains over time [17].

The rate at which the grains grow depends on the diffusion rate. The size of the aluminium grain has been shown to grow over time at elevated temperatures, as can be seen in Figure 2.7. Once the grains grow over

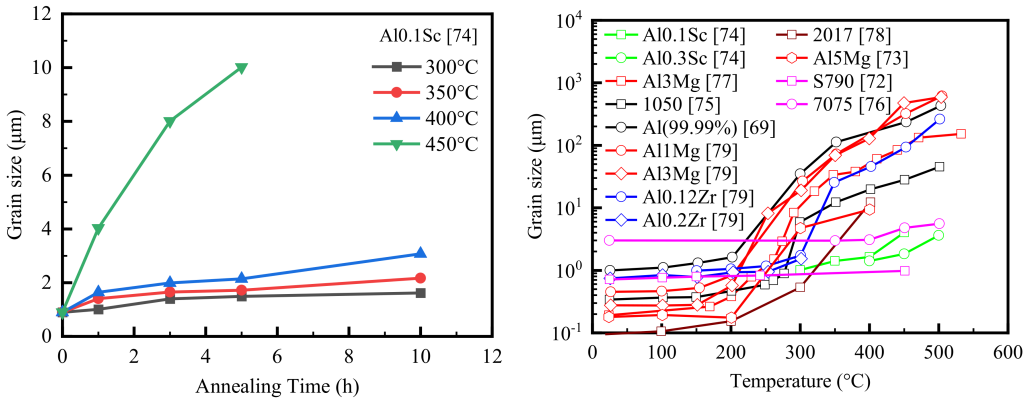

Figure 2.7: Typical grain size evolution over time at various temperatures (a), and typical grain size evolution over temperature for different Al alloys after 1h annealing (b) [28]

time, the growth rate starts to decrease, and higher temperatures result in faster grain growth as is seen in Figure 2.7a and 2.7b respectively.

Another principle that can be recognized in 2.7b is the threshold in the grain growth. The temperature should exceed a certain limit before grain growth takes place. This temperature is called the critical grain growth temperature (T_{gg}) [28]. Many factors influence T_{gg}, such as material composition, processing methods, and microstructure [28]. However, an indication can be given by the relation in Equation 2.1 [29].

$$T_{gg} = \frac{T_m}{2} \tag{2.1}$$

in which T_m is the melt point and both temperatures are expressed in [K].

Dynamic recovery & recrystallisation

Besides the previously discussed recovery and recrystalisation, both processes can occur under an external load as well, called dynamic recovery and dynamic recrystallisation. The processes occur under strain at elevated temperatures [30].

This external load causes more dislocations, to the point where new deformation leads to rearrangement and self-destruction creating cell boundaries [28], [31]. This results in a subgrain structure with low-angle grain boundaries caused by dynamic recovery, see Figure 2.8 (1) and (2).

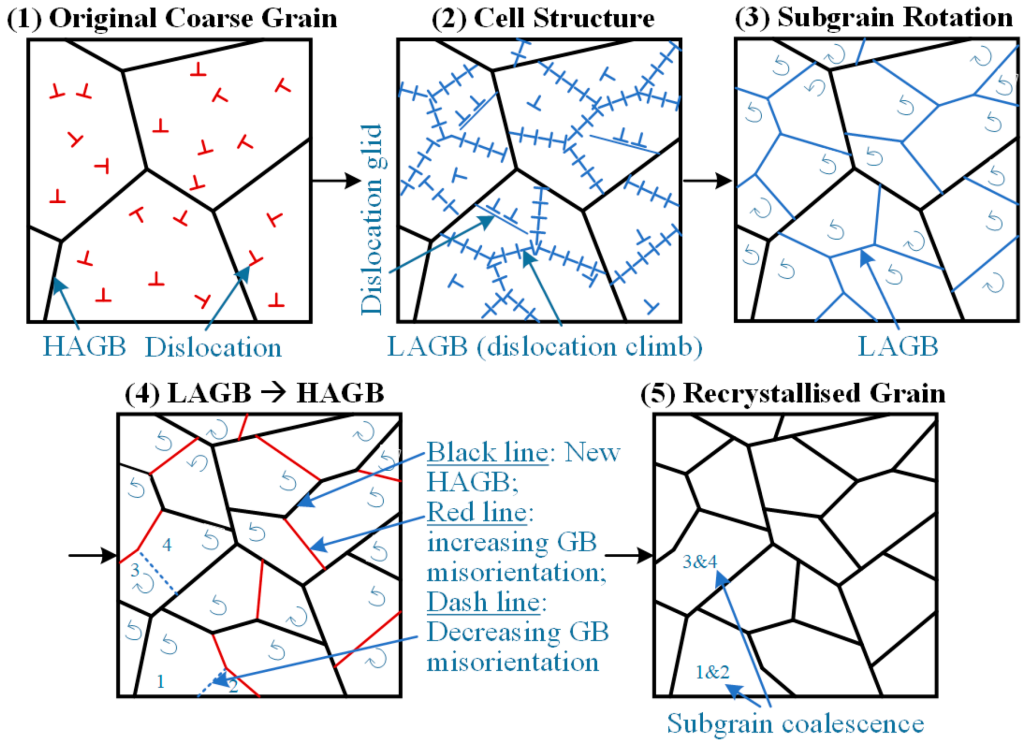

Figure 2.8: The schematic presentation of continuous dynamic recovery and recrystallisation [28]

If the strain continues the subgrains are rotated, increasing the

misorientation, seen in Figure 2.8 (3). Therefore, the low angle grain boundaries become high angle grain boundaries resulting in a grain refinement as depicted in Figure 2.8 (4) and (5) [28], [31]. However, due to the rotation of the subgrains two adjacent subgrains can end up with the same orientation, causing them to merge and become a single grain [28]. The dynamic recrystalisation process is usually started at existing grain boundaries, due to the locally increased internal energy.

2.2 Solid state processes

Additive manufacturing is categorized into fusion-based and solid-state processes. The first melts the material, the second does not. The solid state can then again be divided into sinter-based and plastic deformation-based processes. The focus will be on plastic deformation-based, which adds kinetic energy instead of thermal energy during the process [2], [4].

These mechanical deformation-based processes vary in the energy input between friction, pressure and high velocity. Up till now, some proven methods are: friction stir processing, cold spray techniques, binder jetting, metal extrusion, ultrasonic additive manufacturing, and sheet lamination [2], [4]. In general, these methods have their strengths and limitations, but some common advantages and disadvantages are listed in Table 2.1.

Table 2.1: Advantages and disadvantages of solid-state processes

Advantages	*Disadvantages*
Soft and reactive materials can be processed	High strength alloys are difficult to process
Grain refinement	May require post-processing
None to little residual stress	Small build volumes
Broad range of alloys as feedstock	Slow production rates
Blends different materials	

By switching to a solid-state approach, printing a broad range of alloys

and reactive materials becomes feasible [2], [4]. Additionally, small grains can be achieved by processing without melting while severe plastic deformation takes place [4]. Furtheremore, residual stresses are minimized by preventing the liquid to solid phase transformation [2], and it becomes possible to bond dissimilar metals without a brittle intermetallic layer. Since the bond temperature of metals is located below the meld temperature [2].

It is necessary to take some of the disadvantages of solid-state processing into account as well. First, the material is processed in solid state, so high strength alloys become difficult to process [2]. Furthermore, post processing may be required. To either reach the desired surface roughness or improve the mechanical properties of the build depending on the manufacturing type [2]. Additionally, most processes require long production rates and the build volume is limited, which is why large scale production is not feasible. However, current research in friction stir processes have shown promising results in faster production rates and large scale components [2].

2.3 Friction stir based processes

Friction stir processes are based on material mixing through plastic deformation, resulting in better microstructural properties, for example smaller grain size [32]. Since FSEAM is a friction stir process, as mentioned in Section 1.2, more information on friction stir processes is gathered to get a better insight in what is happening.

Friction stir processes can be divided into welding (FSW), material processing (FSP), cladding (FSC), extrusion (FSE), and additive manufacturing (FSAM). All processes make use of friction and stirring of the material due to a rotating tool, generating heat but staying below the meld temperature. Thus, disregarding the disadvantages of melting the material. All processes have different goals and thus results, but some similar factors can be found within all of them. Since the focus of this research is on friction screw extrusion additive manufacturing, the

extrusion and additive manufacturing processes are discussed in more detail in Section 2.3.1 and 2.3.2.

Friction stir welding, as can be seen in Figure 2.9a, bonds two parts together by creating a material flow from part A to part B and the other way around. This material flow is created by the tool, which softens the material due to frictional heat [33]. By moving the tool, a weld line is formed. FSP, seen in Figure 2.9b, is based on the same process as FSW, but focusses on modifying the microstructure of the surface layer and possibly adding reinforcement particles [34].

Cladding, seen in Figure 2.9c, is used to modify the surface layer, but now by adding additional material to the surface, which could be great for repairs. A consumable rod is pressed onto a substrate. The compression combined with the rotation of the rod generates enough friction to soften the material. The rod is moved over the substrate, where a thin layer remains on the substrate: the clad layer [10].

In general, the output material of a friction stir process is characterized by a homogeneous fine-grained structure [32], [36]–[41]. The grain refinement is up to a micrometre scale, which is not possible with conventional thermo-mechanical processes [40]. This grain refinement finds its origin in the strain field introduced by the rotating tool, causing dynamic recrystallisation and recovery [32], [38]. The important factors for the occurrence of these processes are the generated heat and the processing time [32], [42]. The heat generated is caused by friction and plactic deformation. The amount of friction that builds up comes from the tool rotational speed, the velocity in the process direction, and the downward applied force. For higher tool rotational rates and velocity in the process direction, the friction and plastic deformation is higher, causing more heat to be generated.

As mentioned in Section 2.1.1, for the strength of a material precipitates are more important than the grain size. Therefore, the evolution of these particles is of importance. It is found that precipitates age further during friction stir processes due to heat. Depending on the state of the

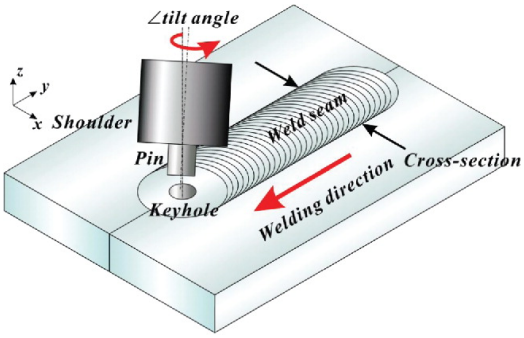

(a) Friction stir welding (FSW) [33]

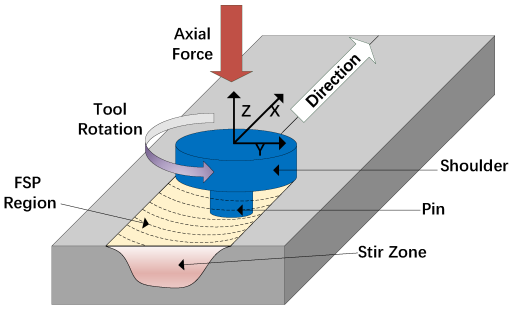

(b) Friction stir processing (FSP) [34]

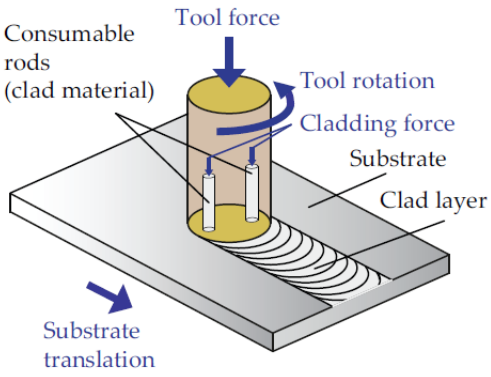

(c) Friction stir cladding (FSC) [35]

Figure 2.9: Friction stir process overview

precipitates in the feed material, they grow and coarsen, or dissolve completely, which can mean both an increase or a decrease in strength [39], [40]. When the precipitates dissolve completely, a comparison can be made with artificial ageing of a material, which is discussed in Section 2.1.1. However, the solutionization step in artificial ageing takes hours [23] while these processes take minutes [39]. In case the precipitate remains/ages to the peak age state, the hardness of the material increases by grain refinement while maintaining good ductility of the material. [38].

2.3.1 Friction stir extrusion

In friction stir extrusion, multiple process heads have been shown to produce an extrudate [36], [43]–[51]. An overview of the different principles is given in Figure 2.10. The first principle is called a friction stir extruder, seen in Figure 2.10a. It consists of a flat rotating tool, which is pressed down onto the feedstock material. In the middle of the tool, the extrusion opening is located and the extrudate comes out of the centre of the tool. The friction stir-back extruder, seen in Figure 2.10b has the same construction but produces a tube instead of a rod. The tool has a rounded top and is smaller than the extrusion chamber in which it is placed. The extruded material comes out at the outside of the tool. Lastly, a rotating screw guides the material to a tapered exit, which can be seen in Figure 2.10c. Here, continuous material feed is achieved, creating a continuous process.

All of the above methods have the same working principle carried out in a different form. Material chips or granulates are compressed and, due to the rotational tool, friction is build, resulting in a rise in temperature and strain, causing severe deformation. While the material is forced to flow to the extrusion die, the energy input causes the material to bond and recrystallise upon exit [46], [47], [52]. This results in grain refinement as mentioned in Section 2.2.

Friction stir extrusion is often described as a great method of recycling material chips [45], [49], [53]. These chips are scrap material created by subtractive methods such as milling. Once a continuous material input can be achieved, it would be possible to create a production line in which material is recycled into wire. This can then again be used as feed material for additive manufacturing or as filler material [53].

By varying the experimental parameters, the properties of the output material can be changed. For instance, the rotational speed of the tool plays an important role. If this is too slow, the heat input will be too low and no extrusion or cold tearing takes place [46]–[51]. If it is too fast, the strain rate becomes too high and swirl defects or hot cracking lower the

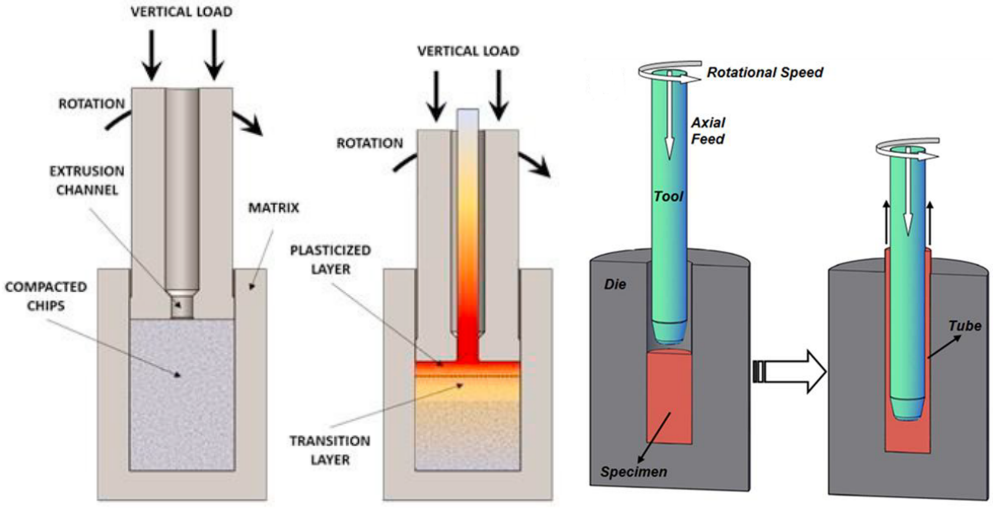

(a) Friction stir extruder [45] *(b)* Friction stir back extruder [36]

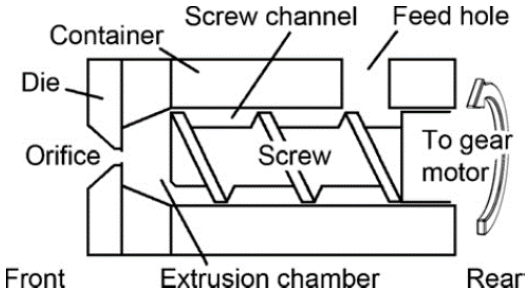

(c) Friction screw extruder [44]

Figure 2.10: Friction stir extrusion processes

mechanical properties [48]–[51]. A balance between these two extremes has to be found experimentally. Previous experiments show that increasing the rotational speed from $180 - 500$ RPM gives a rise in grain size and results in a drop in hardness and yield strength [46], [50]. A proposed explanation for this is a temperature increase causing annealing, that prevents dynamic recrystallisation and causes grain growth instead [46]. However, more important than the grain size is the state of the precipitates [47]. As explained in Section 2.1.1 the thermal cycle is of great importance in relation to the state of the precipitates. Experimental results show a grain refinement with a decreased microhardness, where an increase is expected [43]. Therefore, it is seen

that the contribution of the precipitates dominates the strength change. What can be taken from this is the importance of figuring out how much the precipitates age during the production process. With this knowledge, the desired out put material can be achieved. First, by adjusting the feedstock to achieve the peak aged state as output. Second, by optimizing the process and its parameters to end up with the desired output material. Presumably a combination of both.

Considering the torque, higher values are measured with increased vertical force and decreased rotational speed [47]. The influence of the rotational speed on the torque is explained by heat generation. A higher rotational speed generates more heat and thus softens the material resulting in lower torque. Additionally, it is found that for AA2050 the Cast and T0 conditions will result in higher peak torque and slightly lower average torque values [47]. An explanation is found in the lower hardness, causing the material to stick to the die before it softens, increasing the torque.

For the friction stir extruder and the back extruder, the influence of more parameters is known. It is found that high pressure, therefore a high vertical load, compresses the material too much, which limits the flow and therefore results in an unwanted rough surface. Experiments are carried out with a vertical force of 38.4, 48.4, and 58.4 kN, where the best result was obtained with 38.4 kN [46]. Closely related to the extrusion force is the extrusion velocity. The higher the extrusion force, the higher the velocity [54]. Of course, the extrusion velocity influences the process as well. The longer the material is inside the extrusion chamber, the more heat is generated by friction and plastic deformation within the extrusion chamber. Therefore temperature increases with a constant tool rotation and a decreasing extrusion force [54]. This time at elevated temperatures becomes beneficial once artificial ageing is necessary to meet the required mechanical properties [50]. However, it should be taken into account that there will always be a difference in the thermal cycle for the first and the last extruded material. The material extruded as last remains longer in the extrusion chamber, and thus remains at elevated temperatures for a longer period of time than the first part of the extrudate. Therefore, the properties of the extruded material are not

constant in time from the first until the last part of the extrudate. Nonetheless, a study of W. Tang showed a more or less homogeneous hardness in the extrudate [50].

2.3.2 Friction stir additive manufacturing

To better understand the current knowledge available about friction stir-based additive manufacturing, different methods are discussed that produce a porosity-free structure with a fine homogeneous microstructure [55]–[58].

A division can again be made into 3 principles; Friction surfacing (FS), Additive friction stir deposition (AFSD), and Wire-based friction stir additive manufacturing (WFSAM). In friction surfacing a rotating consumable rod is pressed onto the material by a vertical load [59], seen in Figure 2.11a. In additive friction stir deposition a consumable rod with a non-consumable rotating tool is pressed onto the material by a vertical load, see Figure 2.11b. Last, in wire-based friction stir additive manufacturing, Figure 2.11c, a screw rotates inside a stationary chamber with wire feeding [60]. The last method has the advantage of a continuous process and due to the small stir depth into the previous layer, the interfacial bonding is excellent.

The process parameters correspond with the parameters of friction stir extrusion; vertical load, rotational speed of the tool, and extrusion speed. Since a structure is build, the table speed, layer height, and normal force between the print head and the substrate are added to the list of process parameters. Logically, these additional parameters are related to the ratio between the material feed rate and the extrusion speed.

The working principle is comparable to the friction stir extrusion processes, but with a solid rod as feedstock. A distinction has to be made between the working principle of the first two processes and the screw tool. Methods with feedstock rods are characterized by pressing the feedstock onto the substrate, causing heat generation due to friction and

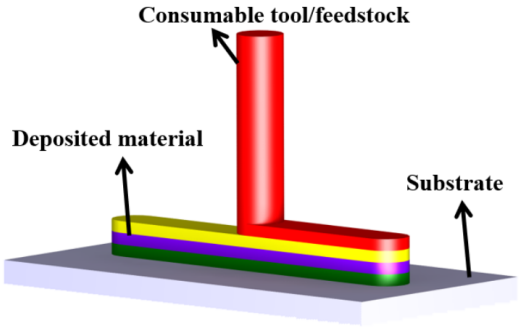

(a) Friction surfacing [59]

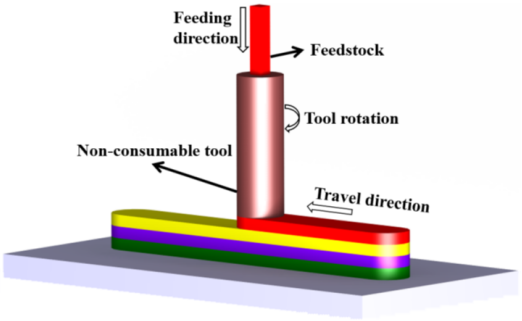

(b) Additive Friction Stir Deposition [59]

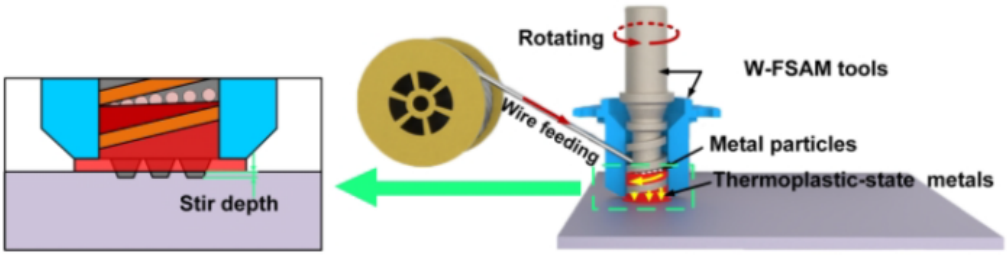

(c) Wire-based friction stir additive manufacturing [60]

Figure 2.11: Friction stir additive manufacturing processes

softening of the material. This results in a thin layer of material, just as in FSC. In rod-based processes, the tool rotation causes severe plastic deformation, and breaks up the oxide layer causing the material to adhere to the substrate while dynamic recrystallisation takes place [57], [59]. Common limitations in the rod based methods are the noncontinuous kind, decrease in mechanical properties due to microstructural evolution [55], [59]. Additionally, up to now production results in a near net shape, requiring post processing like milling to produce accurate parts.

The last process, wire-based friction stir additive manufacturing, builds friction due to the motion of the screw inside the extrusion chamber. The material is severely deformed and compressed within the extrusion chamber, causing the material to soften before extrusion onto the substrate or the previously build layer [60]. A stirring motion to the substrate/previous layer is added to this deposition by probes at the end

of the tool, which is also known from FSW as mentioned in Section 2.3.

In extrusion processes, the material cools down once it is outside the extrusion chamber, which slows down the grain growth and precipitate ageing. In additive manufacturing, this is not the case since the material is reheated by every added layer. This might cause grain growth and precipitate evolution in the bottom layers [59], but only if the temperature overshoots the critical value.

The mechanical properties of the builds are defined by the heat flow, plastic deformation, porosity, interfacial bonding, and the precipitate distribution and state [55], [59], [61]. All process parameters influence these properties in their way, but the relationship is often still unclear, especially for Wire-based friction stir additive manufacturing since this principle is still at the start of the research phase. The goal is to tailor the mechanical properties and microstructure, by gaining control over the grain size and precipitate evolution [60].

Previous research on AFSD has proven hardening [56] and a loss of hardness [62] compared to the base material, and the same holds for the tensile strength [56], [57]. An explanation can be found in the difference between the thermo-mechanical history of the material. The state of the precipitates is expected to be the determining factor for these mechanical properties. A drop in hardness and tensile strength is often accompanied by a rise in elongation at break, an explanation is proposed by solutionisation of the precipitates [57], [58].

A trend which can be recognized for AFSD is the influence of feed rate and rotational speed. With a higher feed rate and rotational speed the grain size increases and the degree of recrystallisation decreases [57]. However, no significant loss of hardness is accompanied by these larger grains. Furthermore, optical analysis by Gang Chen [57] showed a smooth and rough edge finish depending on the rotational direction. The retreating side showed a smoother finish than the advancing side.

Chapter 3

Experimental

In this chapter, the experimental setup with all its subsystems will be explained and the performed experiments will be highlighted. Furthermore, the methods used to analyse the samples is described.

3.1 Experimental setup

The experimental setup consists of a planer machine, an electric motor, a print head, and a feed system. In Figure 3.1 the entire setup is visible. Next, the different parts will be discussed in more detail.

3.1.1 Planer table & motor

The planer table can move in the x-direction. The movement is recorded by a displacement sensor. The motor has a power of $13\,\mathrm{kW}$ and is mounted above the planer table. The motor is used to rotate a tapered screw tool to plastically deform the feed material. The torque is measured and the rotational speed can be set to a specific value. The torque is recorded by a camera, and written down every $30\,\mathrm{sec}$ afterwards. In these experiments, a rotational speed of $400\,\mathrm{RPM}$ is used. At the bottom of the motor frame three load cells are placed to measure the normal force the print head experiences, the location of one of these is depicted in Figure 3.3.

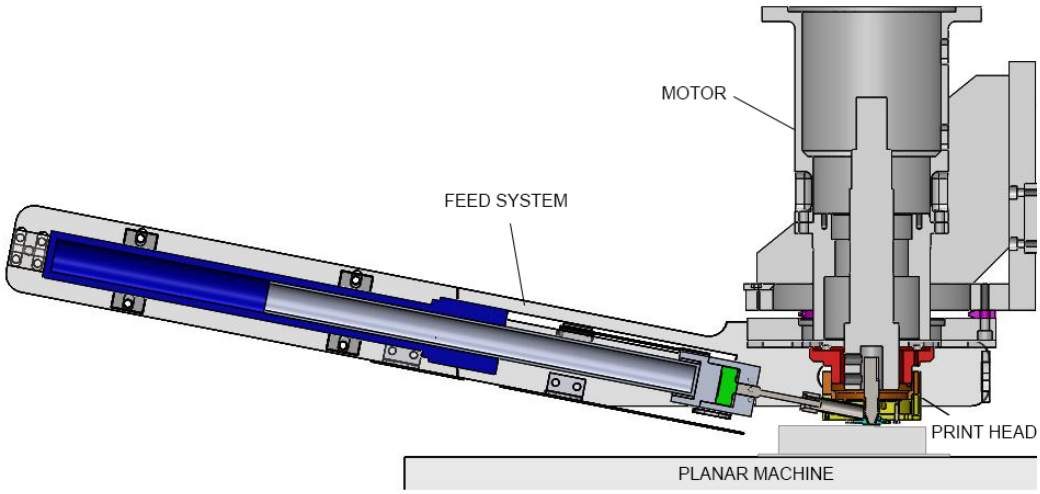

Figure 3.1: Schematic overview of the FSEAM setup

3.1.2 Feed system

The feed system consists of a hydraulic cylinder, a load cell, a pushpin, a displacement sensor, and a feedtube, all displayed in Figure 3.2.

The hydraulic cylinder ensures the force which is needed to push the material into the print head. This is limited to $25\,\mathrm{kN}$ to make sure the setup is not damaged during the experiments. Connected to the hydraulic cylinder, a load cell is present in its holder to measure the force the hydraulic cylinder exerts. In the holder of the load cell, a cavity is made to fit a pushpin. The pushpin is a steel rod, round $8\,\mathrm{mm}$ which is the same diameter as the aluminium feedstock material. The pushpin is used to push the feedstock through the feedtube. The feedtube is mounted in the print head. It is used to guide the material to the tool while being cooled with water. The cooling is needed to make sure the material does not deform plastically or only to a limited amount before it enters the extrusion chamber. Next to that, a displacement sensor is mounted on the load cell holder to record the movement of the pushpin. This movement is used to determine feed rate at which the material is pushed into the extrusion chamber, see Figure 1.2.

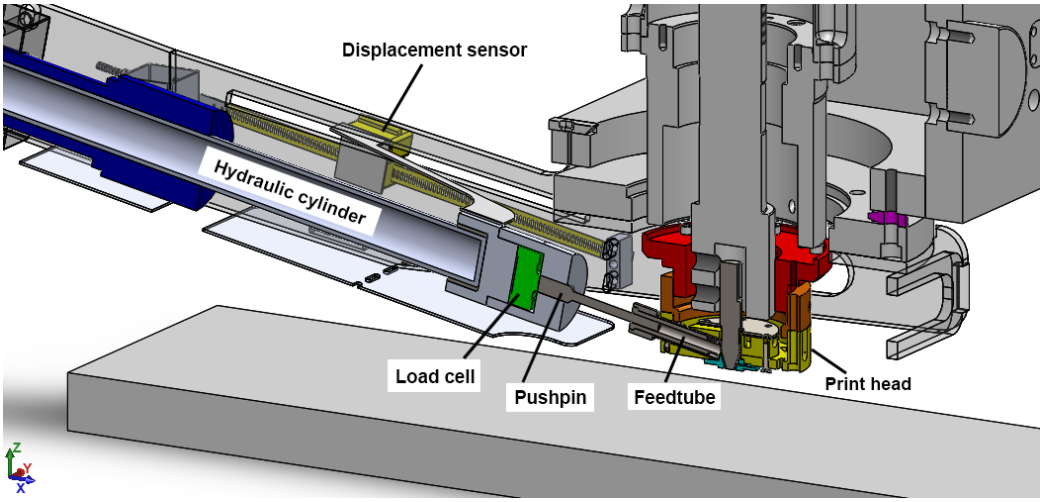

Figure 3.2: Section view of the 3D model of the feed system

3.1.3 Print head

The print head is constructed around a rotating tool, which is mounted to the motor by five bolts. The tool gap, see Figure 1.2, is kept at a constant $3.2\,\mathrm{mm}$. This is achieved with a spacer of $9.2\,\mathrm{mm}$. The print head itself consists of two outer rings where the cooling block, the feedtube, and the nozzle are mounted. An overview of the parts is given in Figure 3.3.

The cooling block is located around the cylindrical part of the tool, to control the temperature during the process, and prevent overheating of the material. Cooling water is guided through the block to control the temperature. The nozzle is shaped to the tapered part of the tool to create a constant tool gap, and small guides are constructed around the opening to make sure the printed material cannot flow to the sides directly. The 3D model of the nozzle shows the guides in Figure 3.4.

3.1.4 Thermocouple placement

The setup is equipped with thermocouples to provide insight into the temperatures during the process. Often multiple thermocouple locations

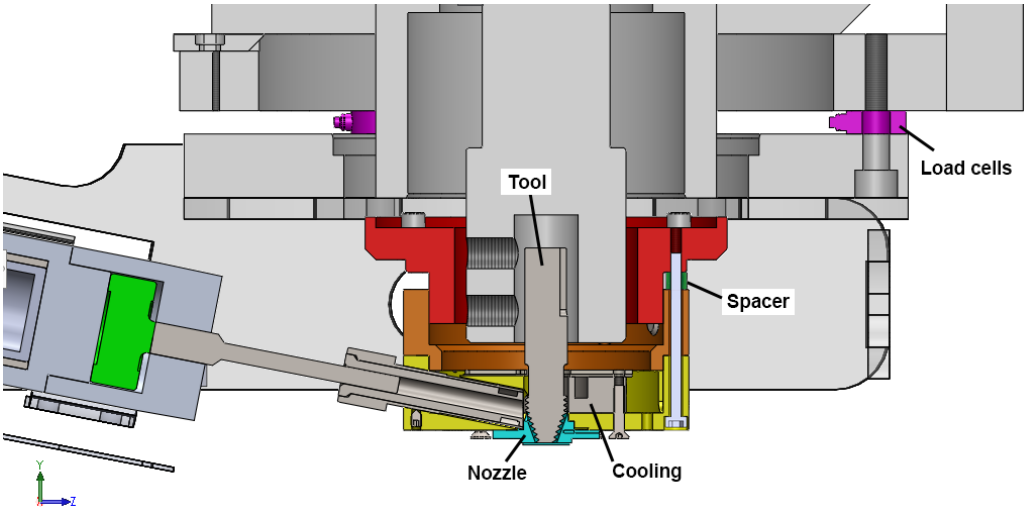

Figure 3.3: Section view of the 3D model of the print head

in the same area are chosen since the thermocouples are fragile and tend to break during the assembly or the process itself. An overview of the thermocouple placement in the print head is given in Figure 3.5. Furthermore, the substrate contains two thermocouples named TC 7 and TC 8, and the temperature of the cooling water is also recorded by TC 9 placed in the cooling water tank. All thermocouples except TC 9 are fixed in place by a thermal paste called Thermofix. The results are given in Appendix B.

3.2 Material

The material used for the experiments is Aluminium 6060 T6, which is in the peak hardened state, see Figure 2.4. The full composition can be found in Table 3.1 and the mechanical properties can be found in Table 3.2. Values are obtained from the material database in GRANTA EduPack 2020 [63]. Additional, previous research from R. Ariës investigated the hardness of the feed material, resulting in a hardness of 80 ± 9 HV.

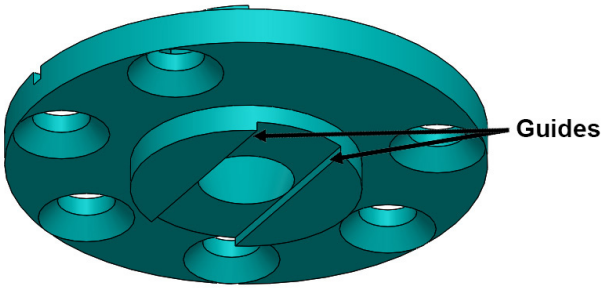

Figure 3.4: 3D model of the nozzle

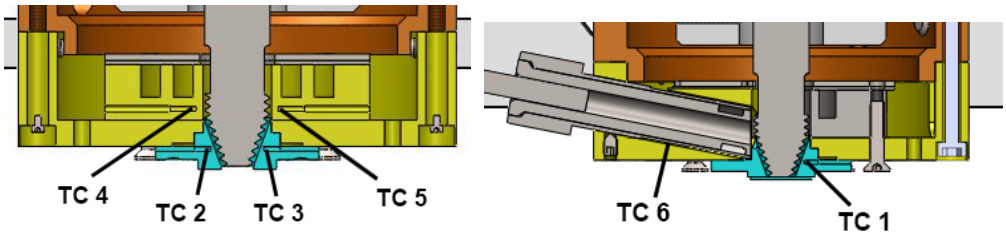

(a) Front view print head *(b)* Side view print head

Figure 3.5: Thermocouple placement

3.3 Performed experiments

Multiple experiments are performed in which the print velocity is varied per experiment. By analysing these builds, the influence of the print velocity can be analysed in the range of $100 - 250\,\mathrm{mm/min}$. Some of these experiments are performed successfully, some less successfully. An overview of all the experiments and their process parameters is given in Appendix A. The successful experiments can be found in Table 3.3.

All experiments are performed on an AA2024 substrate plate with a four-layer start-up phase. The table speed, thus the print speed, is adjusted by a rotary nob which can be varied between 0 - $500\,\mathrm{mm/min}$. The feed rate of the material is adjusted by a control valve turning a key. Therefore, feed rates are measured in keys and vary between key 2 ($0.226\,\mathrm{mm/sec}$) and key 7 ($2.218\,\mathrm{mm/sec}$). In Section 1.2 it is mentioned that overfeeding the material by approximately $30\,\%$ showed builds

Table 3.1: Composition overview AA6060 T6 [63]

Material	Percentage [%]
Aluminium (Al)	97.8 - 99.2
Chromium (Cr)	0 - 0.05
Copper (Cu)	0 - 0.1
Iron (Fe)	0.1 - 0.3
Magnesium (Mg)	0.35 - 0.6
Manganese (Mn)	0 - 0.1
Silicon (Si)	0.3 - 0.6
Titanium (Ti)	0 - 0.1
Zinc (Zn)	0 - 0.15

Table 3.2: Mechanical properties of AA6060 T6 [63]

Elongation [% strain]	8 - 11.5
Elastic modulus [GPa]	69.5 - 73
Tensile strength [MPa]	190 - 222
Yield strength [MPa]	150 - 175

Table 3.3: Print parameters of the successful experiments

Experiment	Average feed ratio [$\mathrm{mm/sec}$]	Table speed [$\mathrm{mm/min}$]	Rotational speed [RPM]
E1	0.453	100	400
E2	0.685	150	400
E3	0.950	200	400
E4	1.154	250	400

without porosity's in previous experiments. Therefore, a build-to-feed ratio of $1\,3$ is applied here as well.

The first layer would vary in table speed between $40 - 50\,\mathrm{mm/min}$ and the second, third, and fourth layers were printed with a table speed of $50\,\mathrm{mm/min}$. For the entire start-up phase, the feed rate is set to key 2.

After the start-up phase, 50 layers are printed with a constant table speed

and material feed rate. The height of the layer is kept constant at $1\,\mathrm{mm}$ for all layers, resulting in a total height of $54\,\mathrm{mm}$ excluding the substrate. The dimensions of the builds are roughly $150\,\mathrm{mm}$ in length and a little more than $10.5\,\mathrm{mm}$ in width due to the feed ratio of 1 3.

Due to the semi-continuous material feed of the process, the material is refilled after every printed layer. The procedure is as follows: At the end of a layer, the table movement is stopped and the print head is moved $1\,\mathrm{mm}$ upwards. Next, the pushpin is retrieved and enough material is inserted in the feedtube to print one full layer. The pushpin is moved back and once close to the feedstock, the feed rate is set to the desired value, pushing the material onto the screw. Pressure starts to rise again and the table movement is started in the opposite direction. The process is repeated at the end of the layer.

During the course of this research, some changes have been made in the experimental procedure. First, flow sensors were installed on the cooling system. The values of the cooling rate of both cooling systems can be found in Appendix A. Next, starting at experiment E2, the cooling water is changed during the experiment. This is done to keep the water temperature below $35\,^{\circ}\mathrm{C}$, which is the maximum temperature of the water being pumped. Last, starting at experiment E3, the material feed rate is adjusted to key 2 instead of the constant material feed rate when the print head is moved upwards.

3.4 Experimental analysis

The successfully manufactured builds from Table 3.3 are all analysed according to the following procedure. The explanation of these analysis methods is coherent with the order in which they are performed.

1. *Pictures*
   The first step is taking pictures of the samples before they are cut into pieces for the other analysis methods. These pictures will be made in front of a white background and with an added ruler for scale.

2. *3D scan*
   Next, a 3D scan of the surface is made of the intact sample. In this way, a digital file of the shape and size of the samples is constructed for reference purposes. The 3D scan is performed with the Shining 3D Einscan Pro 2x Plus.

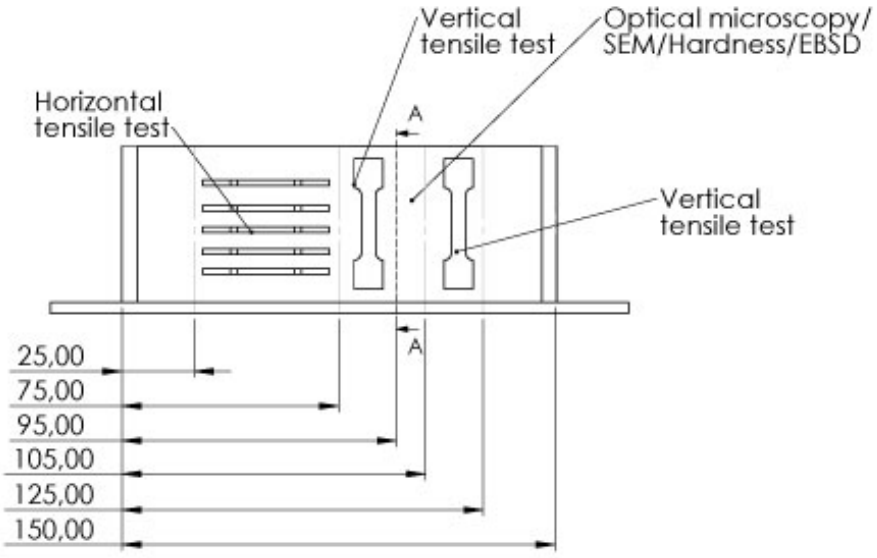

Figure 3.6: Cut plan for the samples, measurements in [mm]

3. *Cutting*
   For the following steps, the samples have to be cut into pieces. The cuts will be made with the Struers Labotom 3. During the cut, water is used as additional cooling. In Figure 3.6 the dimensions of the subdivision of the sample and for which technique it is used can be seen.

4. *Polishing*
   The piece for the microscopy and hardness testing will be hand polished starting with a Gekko plate and grit paper 500, 1000, and 2000. Next, the polishing continues with the MD DAC plate combined with DIA DUO $3\,\mu$m, MD NAP plate combined with DIA DUO $1\,\mu$m, and as the last step the MD GEM plate combined with CHEM OPS NonDry. Once the samples are scratch free, they are

cleaned and ready for further analysis.

5. *Electron microscopy*
   The polished samples were analysed with the Thermo Fisher SEM microscope. This gives the possibility to check for cracks, bond failures, and other physical defects.

6. *Etching*
   After the Thermo Fisher SEM analysis, the samples are etched with a $15\,\%$ solution of NaOH to visualise the flow lines of the material. The duration of etching varied per sample between 30 - $60\,\mathrm{sec}$.

7. *Digital light microscopy*
   To create an overall overview of the flowlines, an image is made with a digital light microscope. Because a metal is analyzed, striking light is used on the VK 9700 Keyence microscope. A scale bar is added, and the overview is made with the stitch function.

8. *Electron Backscatter Diffraction*
   Electron Backscatter Diffraction (EBSD) is performed only on the top sections of the specimens, since the entire height of the build is too big for the JEOL JSM 7200f. EBSD is used to identify the grains and their orientation. The EBSD analysis is performed on four locations throughout the top 20 layers of each sample. An indication of these locations is given in Figure 3.7.

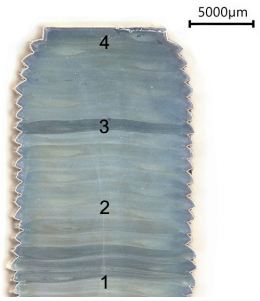

Figure 3.7: Indication of the EBSD locations

9. *Hardness test*
   The hardness of a material can be related to its tensile strength ($\sigma_{tensile}$ in [MPa]) according to Equation 3.1.

$$\sigma_{tensile} = 3 * HV \tag{3.1}$$

in which HV is the hardness in [HV]. Therefore, the hardness of the samples is tested with the Leco LM 100 AT. During this test, a diamond pyramid is pressed into the material with a force of $300\,\mathrm{gf}$ and a duration of $15\,\mathrm{sec}$. The average length of the imprint diagonals is related to the Vickers hardness of the material. This imprint will be measured afterwards. An indent is made in each layer of the center of the wall. In Figure 3.8 the grid of the performed hardness test is shown.

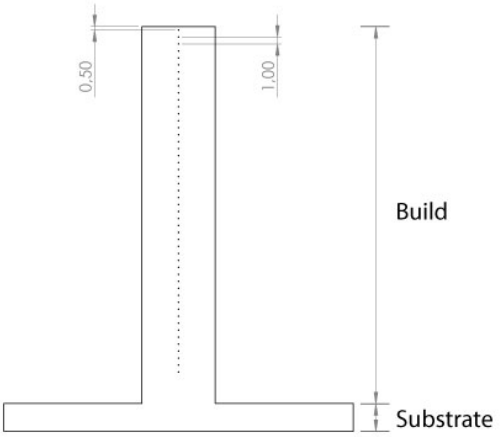

Figure 3.8: Cross section AA from Figure 3.6, Grid hardness tests, measurements in [mm]

10. *Micro CT*
    To find defects within the material without destructive methods, micro CT scans are made of the second set of tensile test specimens. The grey tone of the scans indicates the density of the sample in every location. A light spot indicates high densities, and a dark spot indicates low densities. If a spot differs from the general grey tone, an indication for a defect can be indicated. The CT scans are performed on the ZEISS Xradia Versa 620. To perform the analysis, the test specimens were bonded together in bundles of four to reduce the number of scans necessary, and a tape indicator

was placed to recognise the orientation of the samples. An overview of the prepared samples is given in Figure 3.9.

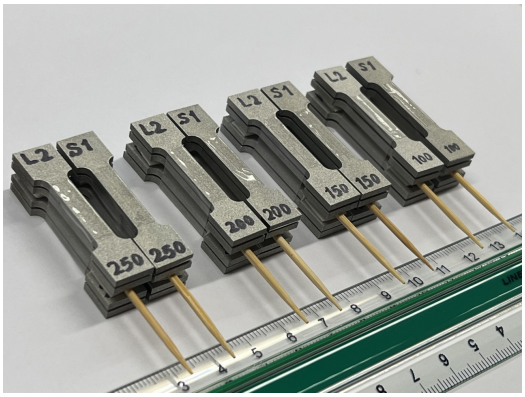

(a) Overview of the bundled samples prepared for micro CT

(b) Tape indicator to verify the orientation of the samples

Figure 3.9: Sample preparation for micro CT

11. *Tensile test*
    To perform tensile tests, an electric discharge machine is needed to extract tensile test samples from the builds. The samples are produced according to the drawing in Figure 3.10. The first set of tensile test samples are tested with the Zwick 1000 Universal Testing System, combined with an extensometer to measure the extension of a specimen, also known as displacement measurement. The second set is tested with the Zwick 1000 Universal Testing System, combined with the ARAMIS Adjustable system, which measures the displacement. Combining the data of both systems stress-strain curves are made.

    From every build, six vertical tensile test samples orthogonal to the printing directing were taken. Three samples were taken from the side of the build (Set 1), and three from the middle (Set 2). The exact location can be seen in Figure 3.6. To study the influence of the sample location and the homogeneity of the build manufactured. Exploratory experiments indicated that the temperature near the

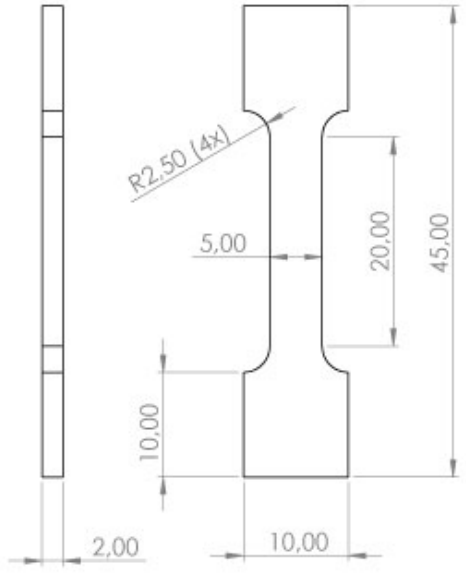

Figure 3.10: Dimensions of the tensile samples in [mm]

build ends are typically lower due to the cooling of the build during refilling of the feed system. Furthermore, five horizontal samples are extracted along the printing direction (Set 2), indicated in Figure 3.6 as well. These horizontal samples are taken to compare the mechanical properties of the print direction to the samples orthogonal to the print direction. To refer to the tensile samples in a clear matter, the samples are named in Table 3.4.

12. *Surface fracture analysis*
    After the tensile tests, the fracture surface of four tensile test samples is analysed. This is done with the SEM function of the JEOL JSM 7200f. An overview picture is made of one side of the fractures.

Table 3.4: Overview of the tensile samples names

	E1 $100\,\mathrm{mm/min}$	E2 $150\,\mathrm{mm/min}$	E3 $200\,\mathrm{mm/min}$	E4 $250\,\mathrm{mm/min}$
Set 1 Vertical samples	100 T1 100 T2 100 T3	150 T1 150 T2 150 T3	200 T1 200 T2 200 T3	250 T1 250 T2 250 T3
Set 2 Vertical samples	100 S1 100 S2 100 S3	150 S1 150 S2 150 S3	200 S1 200 S2 200 S3	250 S1 250 S2 250 S3
Set 2 Horizontal samples	100 L1 100 L2 100 L3 100 L4 100 L5	150 L1 150 L2 150 L3 150 L4 150 L5	200 L1 200 L2 200 L3 200 L4 200 L5	250 L1 250 L2 250 L3 250 L4 250 L5

Chapter 4

Results and discussion

In this chapter, an overview of the results is given. The results are analyzed in detailed and possible explanations for the results are given, based on the previously presented literature. Where necessary, some additional literature is presented.

4.1 Measurements in-situ

In this section, a more detailed description of the process parameters of Experiment E1 is given. It consists of the measurements of 2 layers in the middle section of the build and can be seen in Figure 4.1. From the displacement data of the material feed, a clear distinction can be made between the print phase and the refill phase. Red vertical dashed lines are used to indicate a switch between these phases. Once these phases are indicated in the other measurements as well, a pattern can be recognized.

During the refill phase, the measurements show a drop in value for all measured parameters except the displacement of the pushpin (x_{feed}). This is logical since the pushpin is retrieved to access the feedtube and insert feed material. Next, the pushpin is moved back in the direction of the screw. First, in a higher feed rate since no contact has been made with the material yet. Once contact has been made the feed rate is set to

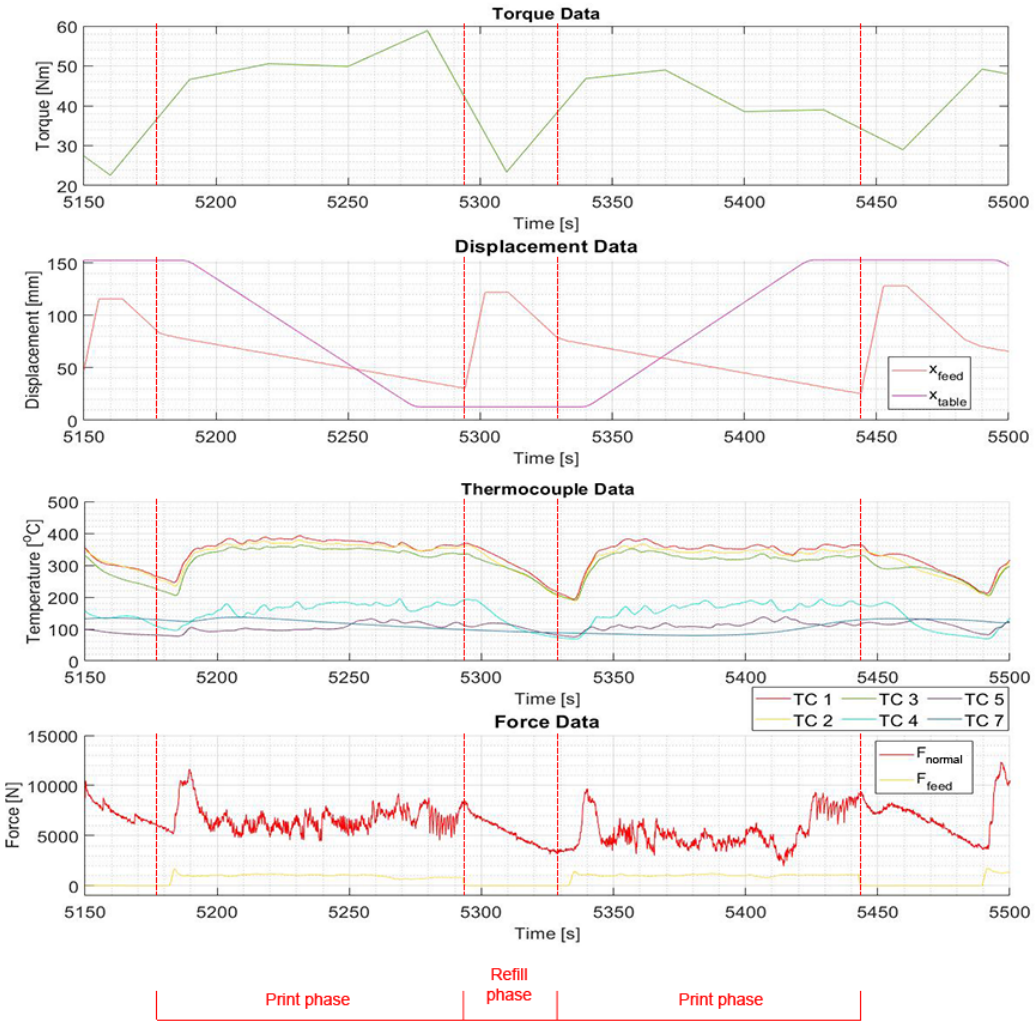

Figure 4.1: Process parameters of 2 layers of experiment E1 performed with FSEAM at a print speed of $100\,\mathrm{mm/min}$ and feedstock material AA6060 T6

the desired value for printing. During the refill phase, the remaining material is not pressed against the screw and no friction is build, lowering the torque and thus no frictional heat is generated, which is seen from the nozzle temperature (T1-T3). Once the feed material is pressed against

the tool again, more friction takes place and the cylinder force, followed by the normale force and the temperatures, starts to climb. Where the temperature climbs to a more or less stable level.

Additionally, little to no material flows out during the refill phase, lowering the normal force on the print head. An increase in normal force is seen at the beginning of the printing phase, which can be explained by the table being stationary. The table stands still during the refill phase and is moved after material deposition is started again. Pressure is build in this short moment of a stationary table during deposition, explaining the small peaks in normal force at the beginning of each print layer.

The peak in the feed force after the refill phase can be explained by the temperature of the feedstock. Once new feed material is added to the feedtube, its temperature is at room temperature. During deposition, a feedstock rod is pressed against the tool, generating the desired friction and heat. This heat is carried through the entire feed material, making it softer and easier to process. This results in a lower feed force. In contrast, after the recharge phase, the material is still cool and hard, resulting in a peak in the feed force at the initial stages of the printing process after refilling.

4.1.1 Nozzle temperature

In Figure 4.2 an overview of the mean nozzle temperature is given by deposit location. This is the mean of TC 1, TC 2, and TC 3. The ends of the build are not taken into account, as indicated in Figure 4.2a. The aim is to eventually replace the refill phase by a continuous material feed. Therefore, the stop and start after every layer are not analyzed. Additionally, only the top 50 layers are taken into account since the start phase of 4 layers were printed with a different speed.

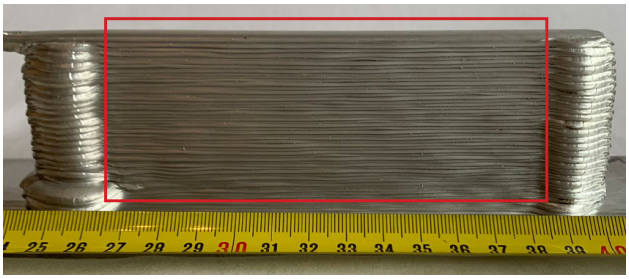

(a) Reviewed section of the print highlighted in red

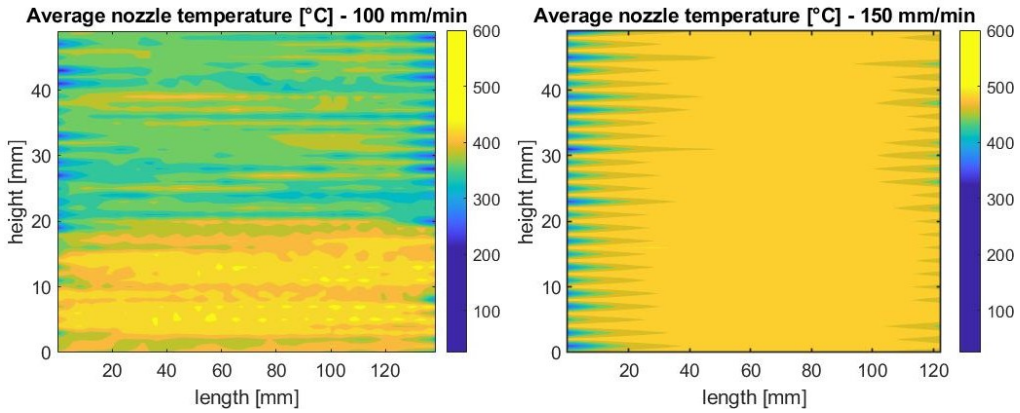

(b) E1 - print velocity 100 mm/min

(c) E2 - print velocity 150 mm/min

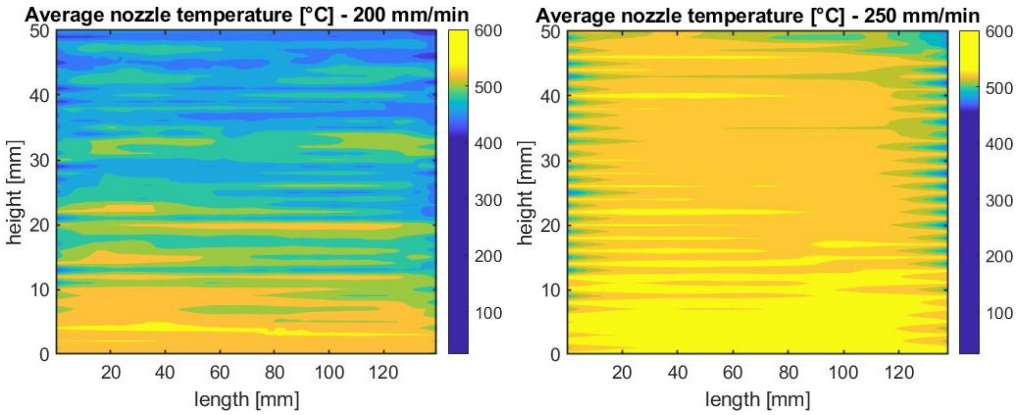

(d) E3 - print velocity 200 mm/min

(e) E4 - print velocity 250 mm/min

Figure 4.2: Average measured nozzle temperature of experiment E1-E4 with various print velocities, performed with FSEAM and feedstock material AA6060 T6

Table 4.1: Mean nozzle temperature of TC 1, TC 2, and TC 3 per experiment during the print phase, with a various print velocity, performed with FSEAM and feedstock material AA6060 T6

	E1	E2	E3	E4
v_{table} [mm/min]	100	150	200	250
T_{nozzle} [°C]	384 ± 35	485 ± 21	493 ± 28	525 ± 10

The overview shows a higher nozzle temperature in the bottom half of the builds for experiment E1, E2, and E4. Furthermore, a clear distinction is made between the temperature within the nozzle of experiment E1 and other experiments. In Table 4.1 the mean nozzle temperatures of the indicated area in Figure 4.2a are given.

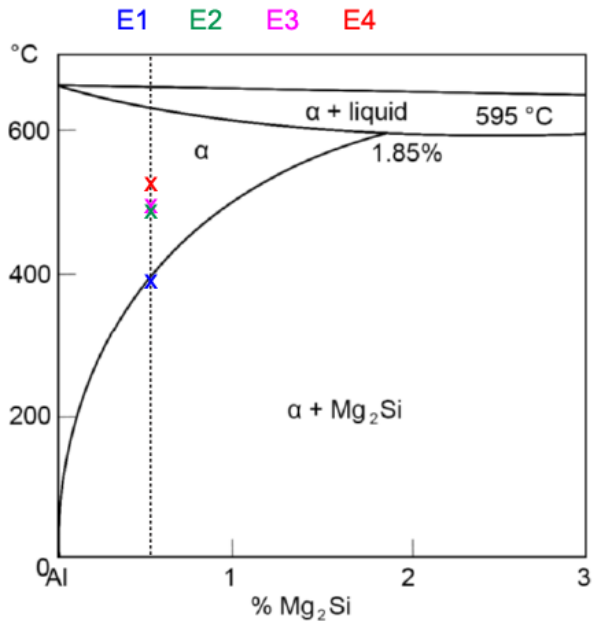

Figure 4.3: Phase diagram indicating AA6060 and the mean nozzle temperatures of experiments E1-E4 [22]

The mean nozzle temperatures indicate an increase in nozzle temperature with increased print velocity. In Figure 4.3, the temperatures

as given in Table 4.1 are depicted in the phase diagram. It is seen that the nozzle temperatures of experiments E2, E3 and E4 are located in the solid solution region. This gives the opportunity for the precipitates to solutionize and start the precipitate ageing from zero after the deposition of the layer. Furthermore, the nozzle temperature of experiment E1 is very close to the solidus line. Probably, some precipitates will solutionize since the material temperature is expected to be higher than the measured nozzle temperature.

4.1.2 Normal force

In the normal force measurements, a noticeable difference is observed between experiment E1 and the other experiments as well. Besides, an increase in normal force is observed with increasing print speed. In Table 4.1 the mean normal forces are given, and in Figure 4.4 the normal force is depicted per deposit location. Both only include the area depicted in Figure 4.2a, for which the reasoning is given in Section 4.1.1.

Figure 4.4 shows a clear gradient throughout the width of the sample for experiment E2, E3 and E4, while experiment E1 shows a blotchy gradient. In all samples, it is seen that the lower half of the layers were exposed to a higher normal force, just as is seen with the nozzle temperature.

Table 4.2: Mean normal force per experiment during the print phase, with a various print velocity, performed with FSEAM and feedstock material AA6060 T6

	E1	E2	E3	E4
v_{table} [mm/min]	100	150	200	250
F_{normal} [kN]	5.35 ± 1.40	8.85 ± 1.55	7.34 ± 0.99	9.32 ± 1.62

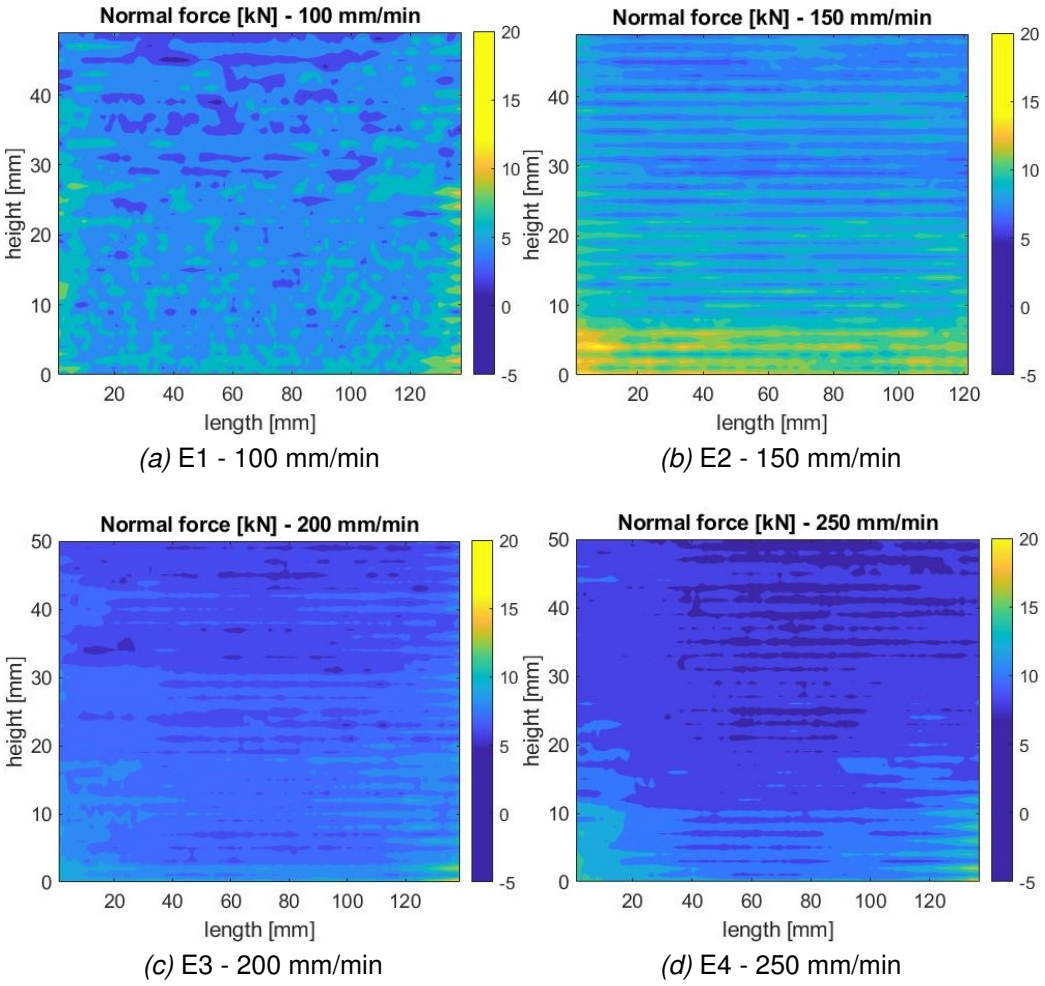

(a) E1 - 100 mm/min

(b) E2 - 150 mm/min

(c) E3 - 200 mm/min

(d) E4 - 250 mm/min

Figure 4.4: Normal force over the deposition location of experiment E1-E4 with various print velocities, performed with FSEAM and feedstock material AA6060 T6

4.1.3 Feed force

The same figures as for the nozzle temperature and the normal force were made for the feed force. However, the load cell of the feed force failed during experiment E2. Therefore, only the data from experiment E1 is reliable and presented in Figure 4.5. Again a decrease is seen after approximately 15 layers, just as in the nozzle temperature. Indicating

more force is necessary to push the feed material onto the screw for these first layers.

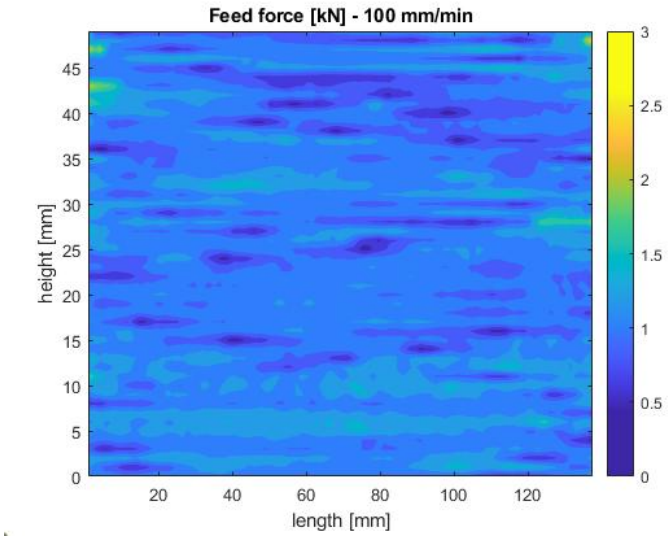

Figure 4.5: Feed force over the deposition location of experiment E1 - $100\,\mathrm{mm/min}$, performed with FSEAM and feedstock material AA6060 T6

4.1.4 Torque

The torque measured during the experiments is given in Figure 4.6 and all experiments are plotted separated in Appendix B. An overview of the mean torque during the print phase is given in Table 4.3. It is suggested that the torque increases with a higher print velocity because the tool rotation is kept constant. So, the tool has to transport more material at the same rotational speed. However, the highest torque is measured in experiment E2 and the lowest in experiment E1.

According to the assumption from Section 2.3.1, a higher peak torque is a sign of a softer feedstock and the mean torque is lower for soft materials. Since one type of feed material is used here, no statements can be made on the peak torque. However, a lower mean torque for a softer material would explain why experiment E2 shows the highest torque values. In

Table 4.3: Mean Torque of experiment E1-E4 during the print phase, with a various print velocity, performed with FSEAM and feedstock material AA6060 T6

	E1	E2	E3	E4
v_{table} [mm/min]	100	150	200	250
ω_{tool} [N m]	39 ± 11	55 ± 18	44 ± 15	41 ± 18

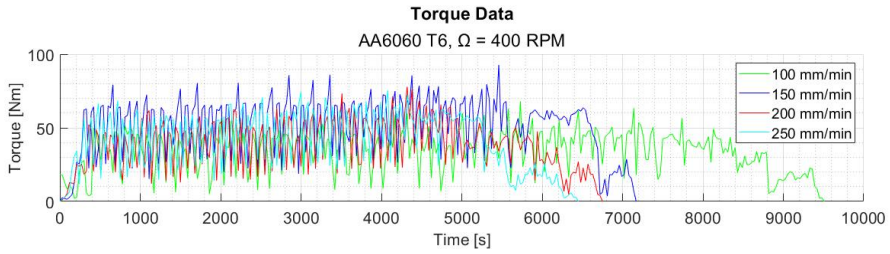

Figure 4.6: Torque data of experiments E1-E4 with various print velocities, performed with FSEAM and feedstock material AA6060 T6

Table 4.1, it can be seen that the nozzle temperature increases with an increasing print speed. Since material becomes softer at high temperatures, it becomes easier to process. This would explain why E3 and E4 have a lower measured torque.

A closer look at the torque data, see Figure 4.6, shows a drop in torque at the end of every experiment, while other in-situ measured parameters remained the same. No clear explanation is found, since the other parameters remain the same, and suddenly less torque is necessary to transport the same amount of material.

4.2 Optical inspection

Optical inspection showed a near-net shape that is expected with respect to the overfeeding. In Figure 4.7, front views of the builds of experiments E1, E2, E3, and E4 are seen. Experiment E2, E3, and E4 all show an

acceptable surface roughness. However, a noticeable difference in surface roughness is observed in experiment E1 were waviness can be identified. A possible explanation can be the lower temperature during the process (see Figure 4.2b), the blotchy normal force (see Figure 4.4a), or a combination of both. At lower deposition temperatures, the material is prone to flow less fluently as it is more solid. The surface roughness could become higher. For the normal force, a higher force would be expected to push more material aside. Therefore, the blotchy development of the normal force could also explain the difference in surface roughness.

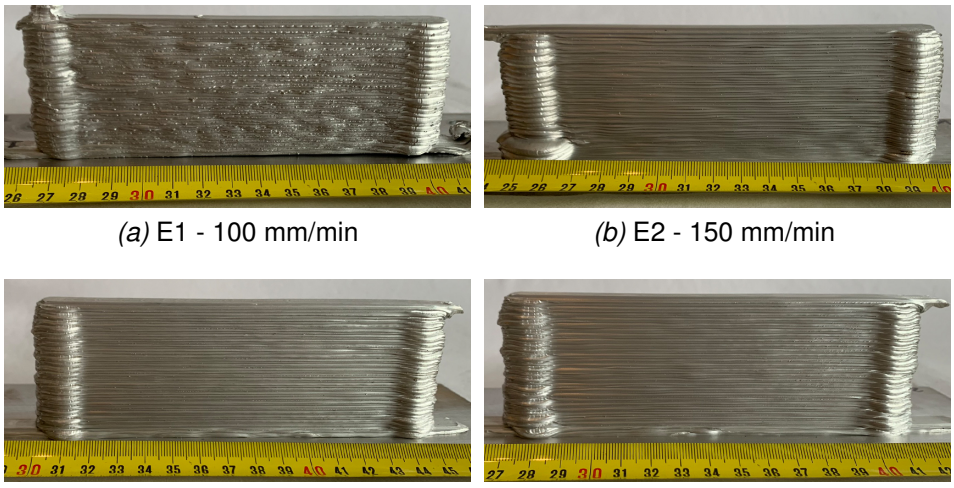

(a) E1 - 100 mm/min *(b)* E2 - 150 mm/min

(c) E3 - 200 mm/min *(d)* E4 - 250 mm/min

Figure 4.7: Visual appearance of experiment E1-E4 with various print velocities, performed with FSEAM and feedstock material AA6060 T6

Preliminary research of R. Ariës and V. Dolas has shown waviness at low print speeds as well. That is, the velocity of the material leaving the nozzle is not constant at low print speeds, even though the feed rate as determined from the position of the hydraulic cylinder is constant. Waviness is observed at print speeds below $150\,\mathrm{mm/min}$. No clear explanation is found for the occurance of the waviness, requiring additional research into the material flow at lower print speeds.

Furthermore, in Section 2.3.2 the difference in surface roughness between the advancing and retreating sides of the build is mentioned. However, in the FSEAM builds both sides have a comparable surface roughness.

4.3 Digital light microscopy

Next, a cut-out of the build was taken to analyze the cross section. After polishing and etching, no defects or porosities were visible in the cross-section with the naked eye. An overview of the cross sections is given in Figure 4.8. Unlike the observations at the in-situ measurements in Section 4.1, no variation is seen between the top and bottom sections.

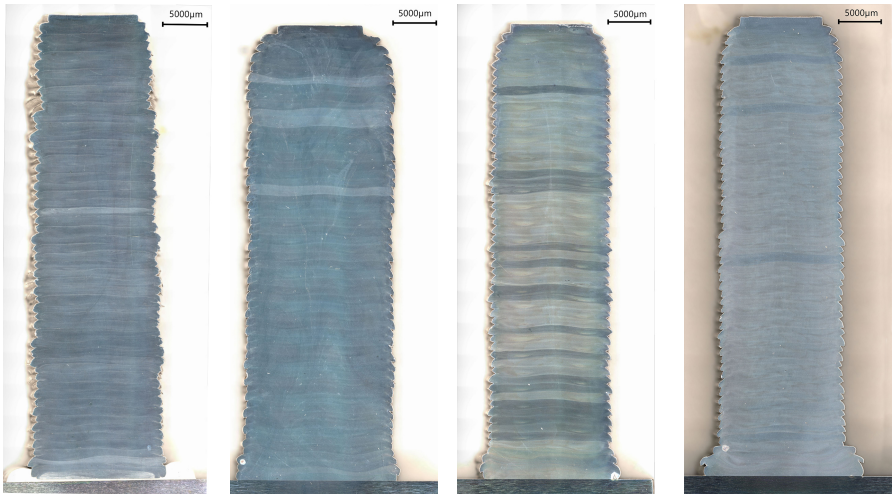

(a) $100\,\mathrm{mm/min}$ *(b)* $150\,\mathrm{mm/min}$ *(c)* $200\,\mathrm{mm/min}$ *(d)* $250\,\mathrm{mm/min}$

Figure 4.8: Light microscopy images of the cross section of experiment E1-E4 (left to right) with a various print velocity, performed with FSEAM and feedstock material AA6060 T6

What can be identified are the different layers. Additionally, all cross sections show different grey tones throughout the height. These different grey tones do not show a clear pattern and can not be related to the

measurements in-situ. A possible explanation can be sought in oxidation after etching [64].

In Figure 4.9, a closer look shows the start of some surface cracks, originating from the edges. Combined with the visible flow lines on the surface a hypothesis can be made. A pattern is seen near the edges, where every layer overflows in the protrusions of the layer below. An explanation can be found in the guiding walls next to the nozzle opening, see Figure 3.4. The newly deposited material is enclosed by these guides, building pressure until the entire cavity is filled. Due to this rise in pressure and temperature, a good bond between the layers is ensured. However, since the material is overfed, it tries to find a way out, which is downwards. A pressure drop occurs at the side, since the material is no longer restricted, resulting in bad interlayer bonding and the formation of surface cracks. A simplified overview of these steps is given in Figure 4.10.

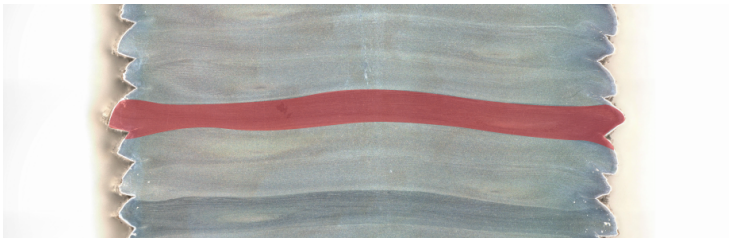

Figure 4.9: Flow line of a layer within the cross section of experiment E3, performed with FSEAM and feedstock material AA6060 T6

For future applications, the surface cracks are a concern because these small cracks can grow inward and cause weak spots between the layers. An easy workaround is to mill the surface layer to a point where the surface cracks are not present. However, more desired is optimizing the production process to deposit the exact amount of material that is needed, so the protrusions are prevented instead of overcome.

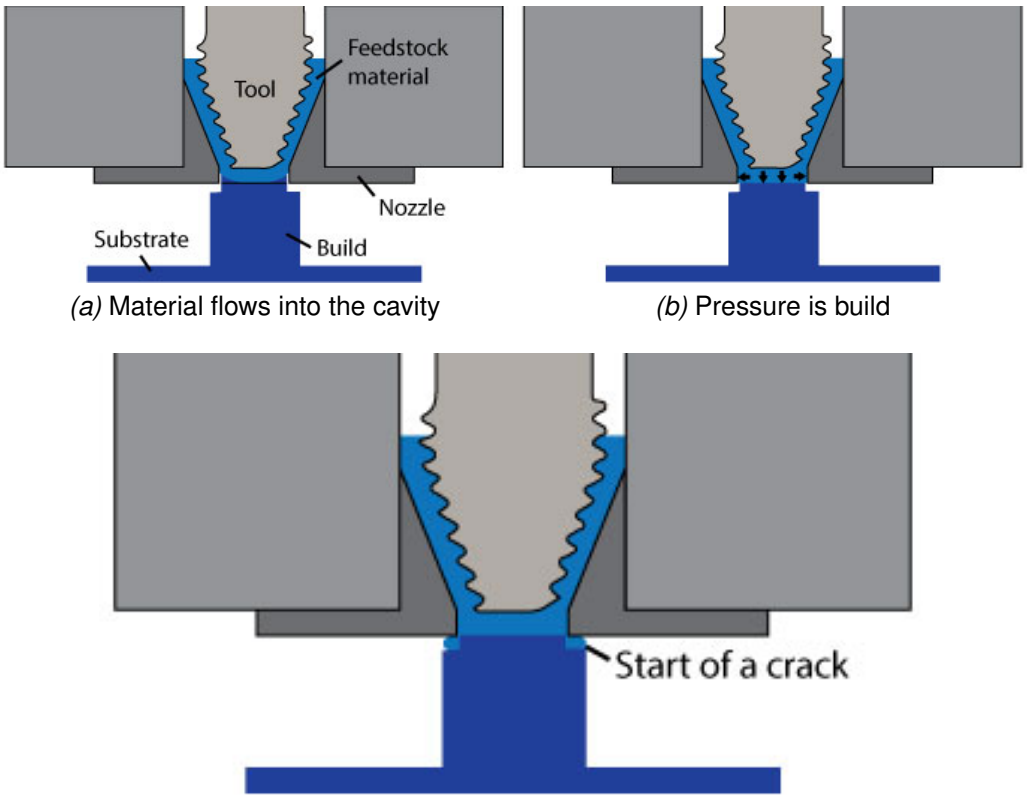

(a) Material flows into the cavity

(b) Pressure is build

(c) Material overflows

Figure 4.10: Simplified schematic overview of surface crack formation from the edges of a FSEAM build

4.4 Scanning Electron Microscopy

The electron microscopy, or SEM, showed good overall results. At macro scale there are no defects found, but using a higher magnification some microscale defects can be found. These defects can be divided in roughly three categories. First, porosity spots between 10 - $50\,\mu$m, as can be seen in Figure 4.11a. Second, there are sparse defects such as Figure 4.11b with a diameter of $\pm$ $50\,\mu$m. Finally, horizontally aligned micro-cracks, such as in Figure 4.11c that are only seen in Experiment E1.

The porosity's are mainly seen in experiment E1 and E4. Which might be

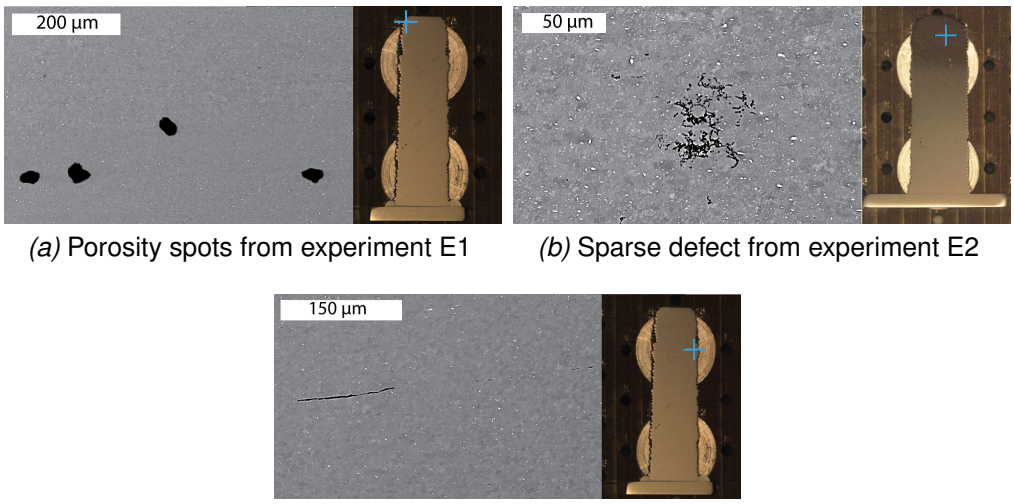

(a) Porosity spots from experiment E1 *(b)* Sparse defect from experiment E2

(c) Crack from experiment E1

Figure 4.11: Microstructural defects in FSEAM experiments E1 and E2, where the location in the build is indicated on the right

due to too the print speed and the heat input. In friction stir welding porosity's like these are observed as well. They are caused by either insufficient heat input, or abnormal stirring causing an abundance of heat [65]. Since the porosity's in experiment E1 are mainly seen in the top section and for experiment E4 in the bottom half, this would be in line with the measured nozzle temperatures. In Figure 4.2, it is seen that the bottom half of experiment E4 measured the highest nozzle temperatures, and the top section of experiment E1 measured the lowest nozzle temperatures.

The sparse defects seem to appear at grain boundaries, revealing a local globular microstructure. Globular microstructures are known from trixoforming, an additive manufacturing process where the feedstock has to be semi-solid. A possible explanation for the occurrence of this microstructure can be found in the combination of high temperatures and the applied normal force during deposition. This combination can result in recrystalisation, but also in partial melting of the material [66]. In case the material partially melts and cooling is sufficiently quick, the liquid gets

trapped, resulting in structures like Figure 4.11b. However, this is often seen in the entire micro structure instead of the local defects observed in the FSEAM builds. Additional research into these sparse defects should reveal if enclosed liquid is present in these defects.

The micro-cracks from experiment E1, seen in Figure 4.11c, indicate bad interlayer bonding. This might be caused by a lack of pressure and/or too low temperatures, since experiment E1 shows a slightly lower normal force and a lower nozzle temperature compared to the other experiments as seen in Table 4.1 and 4.2.

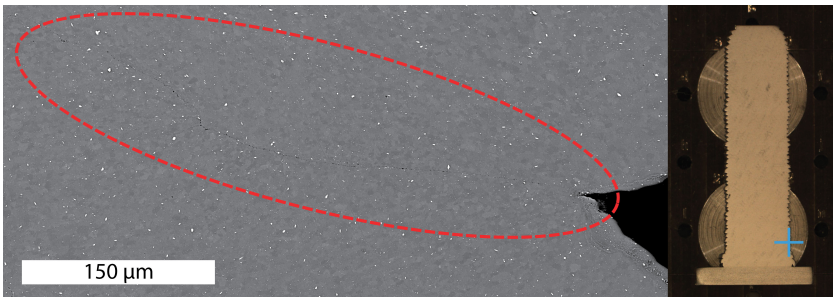

Figure 4.12: Surface crack originating from the edge of experiment E3, where the location in the build is indicated on the right

Last, surface cracks, as described in Section 4.3, are seen in all experiments. With the SEM pictures, see Figure 4.12, it is verified that these surface cracks are found between every layer.

4.5 Electron Backscatter Diffraction

The electron backscatter diffraction revealed a grain refinement after processing, just as in previous FSEAM experiment AM-3 of R. Ariës [12]. The feedstock has a significant bigger grain size than the experiments as can be seen in Figure 4.13. Additionally, a difference in grain size is observed in experiment E1 and the others. The mean, minimum, and maximum values of the equivalent circle diameter (ECD) of the grains are

given in Table 4.4, the full grain size distribution can be found in Appendix C. Locations of the measurements link to the numbers in Figure 4.14.

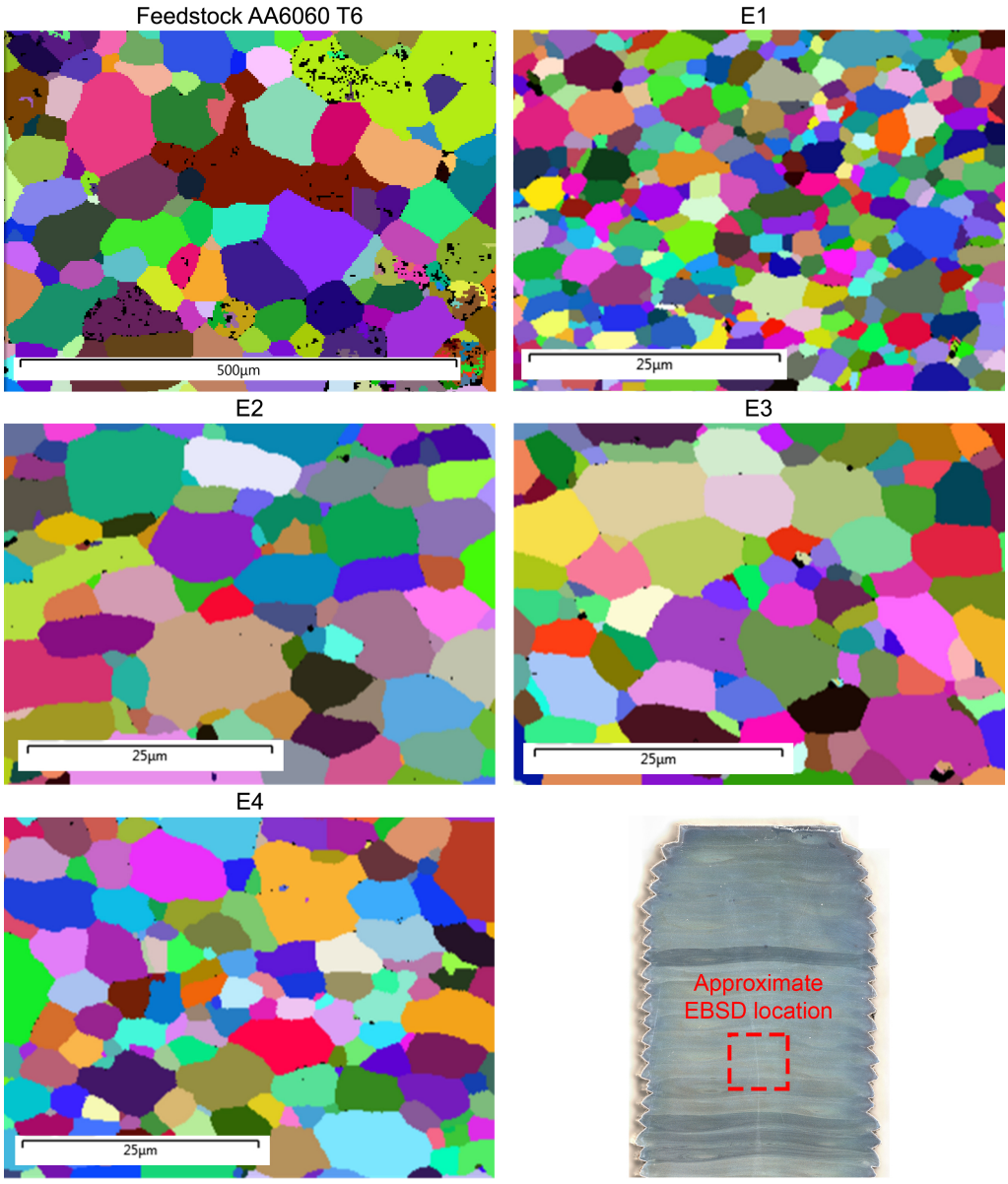

Figure 4.13: Grain size comparison of the feedstock material AA6060 T6 and experiments E1-E4 with various print velocities, produced by FSEAM

Table 4.4: ECD measurements of experiment E1-E4 in [µm]

	E1 - 100 mm/min				E2 - 150 mm/min			
Location	1	2	3	4	1	2	3	4
Mean	2,1	1,98	2	1,77	3,79	4,24	4,09	4,14
Minimum	0,42	0,42	0,42	0,42	0,56	0,4	0,4	0,4
Maximum	7,33	5,87	5,87	5,52	12,73	15,89	13,22	15,02
	E3 - 200 mm/min				E4 - 250 mm/min			
Location	1	2	3	4	1	2	3	4
Mean	3,43	3,72	3,37	3,08	3,67	3,45	3,88	3,4
Minimum	0,4	0,4	0,4	0,4	0,44	0,44	0,44	0,41
Maximum	10,91	11,61	11,82	9,21	13,17	17,15	15,02	11,63

The small grains of experiment E1 can be explained by the lower process temperatures. The mean nozzle temperature of experiment E1 is $384\,°C$, while the other mean temperatures of the experiments are at least $100\,°C$ higher, see Table 4.1. An explanation might be that the grains grow more right after deposition. Because the deposition temperature is higher, it takes more time for the material to cool down below the critic grain growth temperature as mentioned in Section 2.1. Therefore, the grains have more time to grow right after deposition.

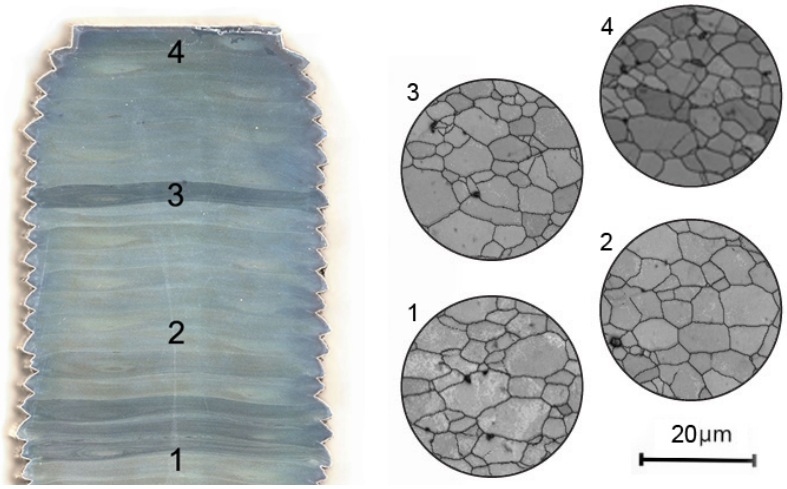

Figure 4.14: Experiment E3 - Grains from the 4 locations

In section 2.3.2 it is mentioned that Additive Friction Stir Deposition showed a larger grain size with increasing feed rate and rotational speed, due to a lower degree of recrystalisation. Comparing the results of FSEAM this is not the case, since all samples show a refinement of the grains. Additionally, no trend can be recognized in the grain size with an increasing print velocity.

In previous research by R. Ariës, it was seen that the grain size did not vary with the height of the build [12]. An explanation was found in a process temperature close to the critical grain growth temperature, as mentioned in 2.1. With a melt temperature estimated at $625\,^{\circ}\mathrm{C}$ [63] this results in a critical grain growth temperature of $176\,^{\circ}\mathrm{C}$. During the process, the temperature of the build remained mostly below this limit. In Figure 4.15, an overview is given of the substrate temperatures (TC 7 or TC 8) of the analyzed experiments. For each experiment the thermocouple closest to the build is selected. The black line in Figure 4.15 indicates T_{gg}. Local maximum temperatures overshoot the critical grain growth temperature, but drop below the T_{gg} relatively quick (50 - $150\,\mathrm{sec}$), making the time available for grain growth small.

A difference in the peak temperature of experiment E1 and the others is also observed. The substrate temperature of experiment E1 stays below T_{gg} after the first 13 layers, where the peak temperatures of the other experiments remain around the critical grain growth value for the entire build.

Since only the top section of the build was examined, no statements can be made over the entire height of the build. However, in the upper part of all experiments, it is seen that the grain size remains roughly the same, so no significant grain growth is assumed during the build. The microstructures at the four different locations are depicted in Figure 4.14 for experiment E3.

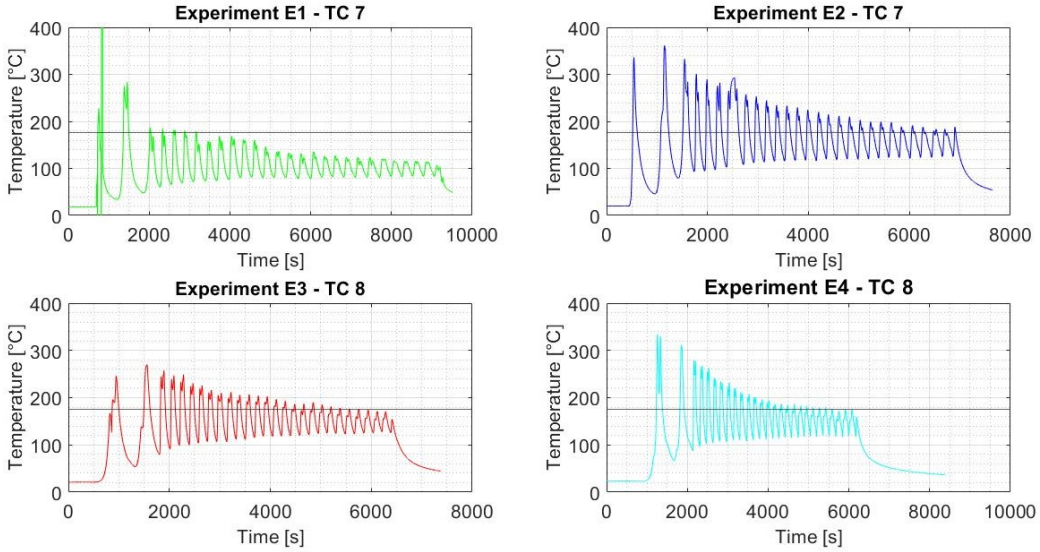

Figure 4.15: Substrate temperatures of experiment E1-E4

4.6 Hardness

Hardness tests of the builds show a relatively uniform hardness throughout the height of the builds. However, an increased hardness is seen in the top layers of experiment E2, E3, and E4. An overview of the results is given in Figure 4.16. This increase might be caused by the shorter time at elevated temperatures of the top layer. Since no additional layers are added, the top layer is not reheated, decreasing the time at elevated temperatures compared to the lower layers of the build.

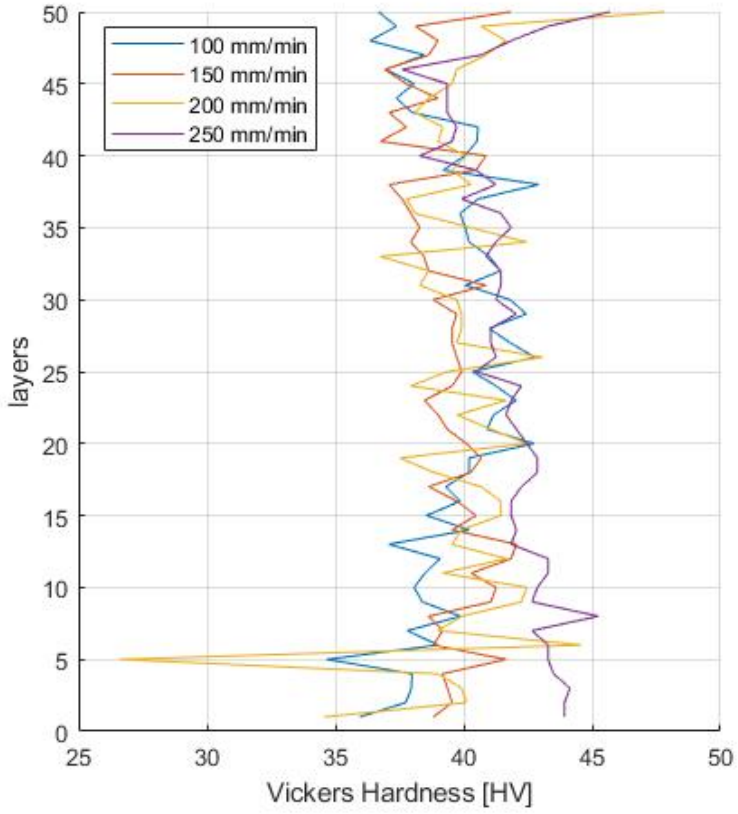

Figure 4.16: Hardness measurements in [HV] over the length of the cross section of experiments E1-E4 with various print velocities, performed with FSEAM and feedstock material AA6060 T6

Furthermore, one outlier in layer 5 is seen in experiment E3, which might be caused by a defect. Figure 4.17 shows an example of some defects observed in the SEM analysis near the location of the hardness measurement.

Besides, the hardness of the walls is roughly the same for all the printing speeds. This would mean that the tensile strength should be roughly the same as well, according to the relation in equation 3.1. Since the hardness has an average of $40\,\mathrm{HV}$, an estimation for the tensile strength

can be made of 120 MPa.

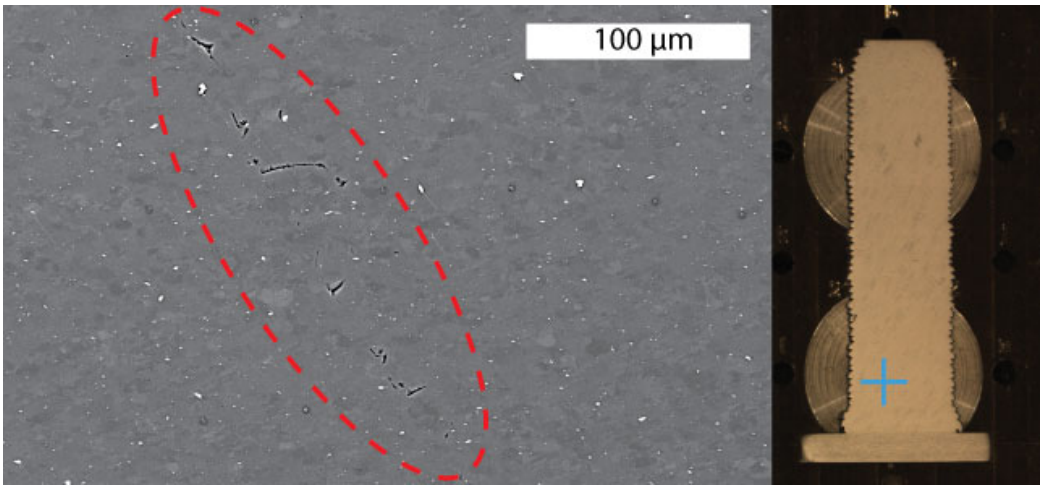

Figure 4.17: Defects found in the SEM analysis of experiment E3 near the outlier of the harness analysis

Overall, a decrease in hardness compared to the feedstock occurred. The feedstock material had a Vickers hardness of approximately 80 HV [12], while the samples showed a hardness of approximately 40 HV.

4.7 Tensile tests part 1

In Figure 4.18, the tensile-strain curves of the tensile test results of Set 1 are shown per experiment. The $0.2\,\%$ yield strength is indicated by the 'x' symbol, the 'o' symbol indicates the tensile strength. The samples deform elastic between 0 to 'x', and plastic deformation occurs between 'x' and 'o'. Furthermore, a sudden decrease after 'o' is an indication for premature fracture of the sample. Sample names are indicated in Table 3.4.

All samples from experiment E1 failed relatively fast after plastic deformation, resulting in a small elongation at fracture. This is seen in

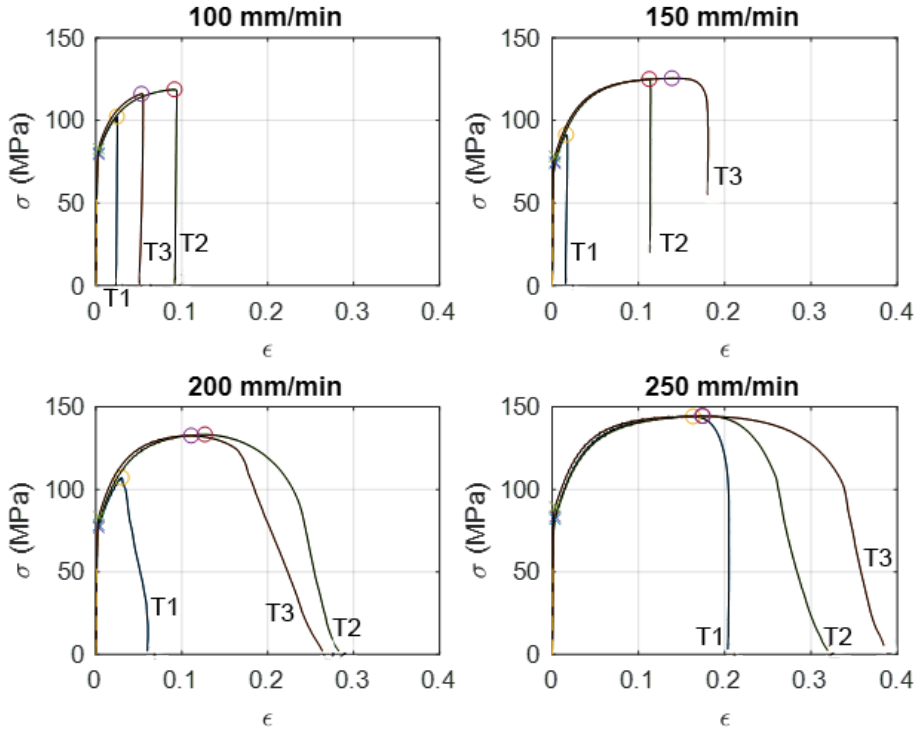

Figure 4.18: Stress-strain curves of tensile tests - Set 1, produced from a FSEAM build with feedstock material AA6060 T6. Tensile samples are located and orientated as depicted in Figure 3.6

sample 150 T1 and 150 T2 from experiment E2 as well. Additionally, multiple samples broke in the fillet region of the tensile samples, which is outside the measurement region of the extensometer. Therefore, the measured elongation at fracture is not correct.

A possible explanation for the premature fracture is that the samples are taken from the side of the build, see Set 1 in Figure 3.6. Where it is expected that the normal force and the temperature of the nozzle have not yet stabilized after the filling tube has been refilled. In Figure 4.1 this can be seen by the data of the F_{normal}, TC 1, TC 2, and TC 3 at the start of the print phase. This might result in bad interlayer bonding and thus

premature fracture. To check whether tensile samples from the center of the build give better results an additional set of tensile test samples is taken and tested in Section 4.9. The location of the vertical samples of Set 2 are indicated in Figure 3.6.

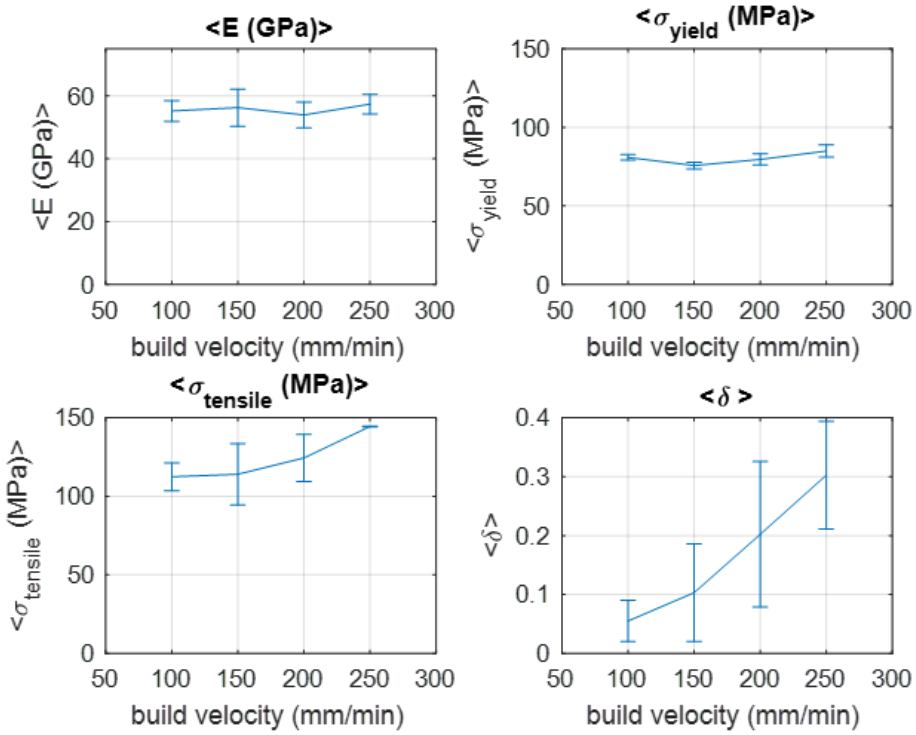

Figure 4.19: Mechanical properties of tensile tests - Set 1, produced from a FSEAM build with feedstock material AA6060 T6, with (E) the elasticity modulus, (σ_{yield}) the yield strength, ($\sigma_{tensile}$) the tensile strength, and (δ) the elongation at fracture. Tensile samples are located and orientated as depicted in Figure 3.6

The mechanical properties per experiment are given in Figure 4.19. Where E is the elasticity modulus, σ_{yield} the yield strength, $\sigma_{tensile}$ the tensile strength, and δ the elongation at fracture. As can be seen the elasticity modulus (approximately $55\,\mathrm{GPa}$), and yield strength

(approximately $80\,\mathrm{MPa}$) remain roughly the same for all experiments. However, an increase in tensile strength is observed between experiments E1 and E4, starting at approximately $110\,\mathrm{MPa}$ and increasing up to approximately $145\,\mathrm{MPa}$. Since most samples of experiment E1 and E2 broke early in the plastic deformed region, the second set of tensile samples is discussed before a comparison is made with the literature.

4.7.1 Serrated flow

A closer look at the stress-strain curves revealed a sawtooth pattern for experiment E2, E3, and E4 as seen in Figure 4.20. This phenomenon, known as serrated flow, shows an initial straight deformation curve followed by sudden stress drops in a short time [67], [68]. Two explanations for these load-serrations in aluminium are found in the literature; Dynamic Strain Aging (DSA), and precipitate shearing [69], [70].

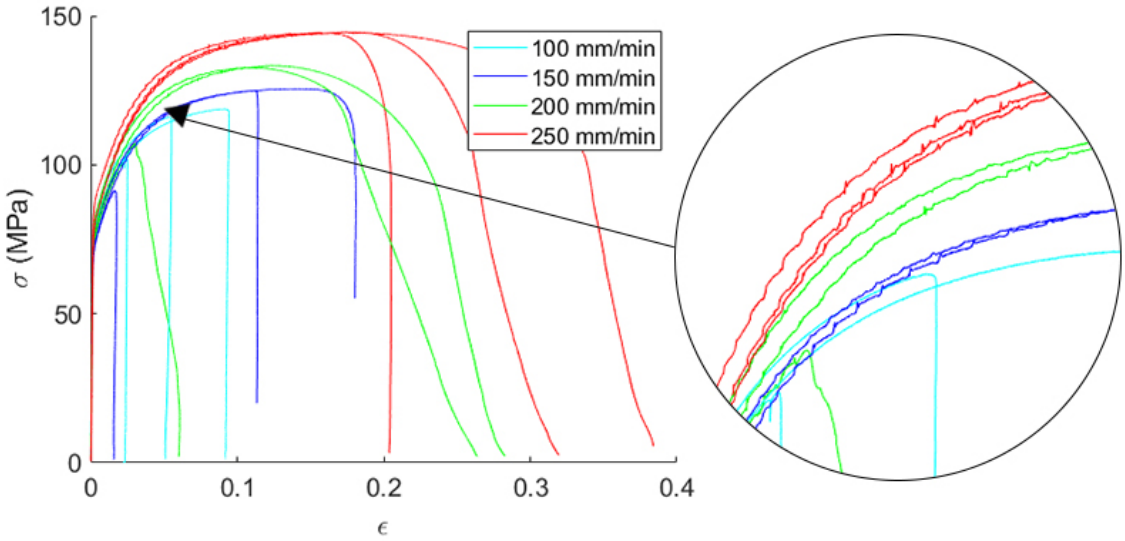

Figure 4.20: Serration in the tensile test results

The first explanation is Dynamic Strain Aging, where locking of mobile

dislocations by solute elements takes place. Solute atoms diffuse and stick to dislocations, locking the displacement and making them temporarily immobile, until they are overcome with the aid of thermal fluctuations [68], [70]–[72].

Second, precipitate shearing makes use of small coherent precipitates to stop the movement of dislocations, as is explained in Section 2.1. This forced stop causes a local stress concentration and eventually, the dislocations shear the precipitates, resulting in a sudden drop in the stress. This process repeats itself for the next blockade, creating the sawtooth-like pattern [68], [70].

Depending on the type of serration, an assumption can be made on the state of the precipitates. It is seen that the sawtooth pattern becomes larger for the higher print velocities. Combining this with the knowledge of the higher mean nozzle temperatures, it is expected that the precipitates solutionized.

4.8 Micro CT

The second set of tensile test samples is scanned with the micro CT to search for defects in a non-destructible manner. The scans showed mainly contaminations of some sort instead of porosity's with enclosed air. Both the horizontal and vertical samples showed defects, and no trend is seen in the amount or size of defects found in the horizontal versus the vertical samples.

Examples of the contamination and porosity are given in Figure 4.21. Both defects are from the samples of experiment E1, which showed the largest defects of all experiments. Most defects, which are smaller in size, are found in the samples of experiment E3.

These contaminations are evaluated through an energy-dispersive X-ray (EDX) analysis. Because this analysis can only be performed on the

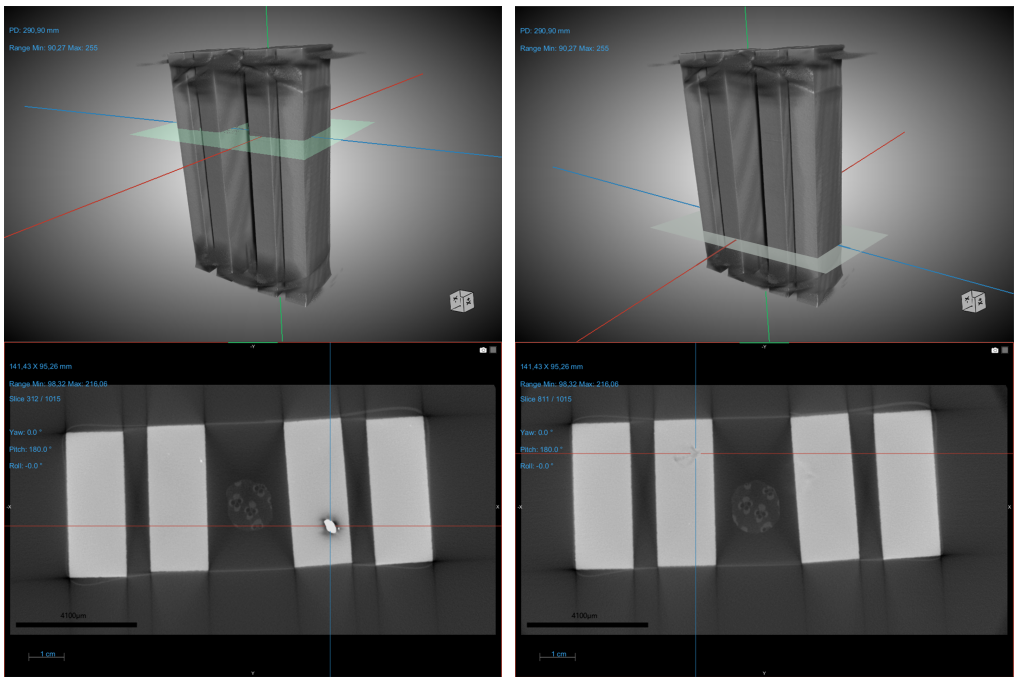

(a) Contamination *(b)* Enclosed air

Figure 4.21: Defects found in tensile test samples of experiment E1. Images at the top display the location of the cross sections analyzed. The bottom figures indicate the density distribution in the cross sections.

surface layer, samples were chosen with some defects on the surface layer. However, during the analysis, these defects could not be seen. This could be an indication that the matrix material covers the defects. So, the contaminations are covered in aluminium. The composition of these contaminations remains unknown.

Additionally, in Section 4.10, the location of the defects seen through micro CT will be compared to the fracture location of the tensile samples.

4.9 Tensile tests part 2

The stress-strain curves from the second set of the tensile tests are subdivided in horizontal and vertical samples. The vertical samples are shown in Figure 4.22 and the horizontal samples in Figure 4.23. Just as in Section 4.7, the $0.2\,\%$ yield strength is indicated by the 'x' symbol, and the 'o' symbol indicates the tensile strength.

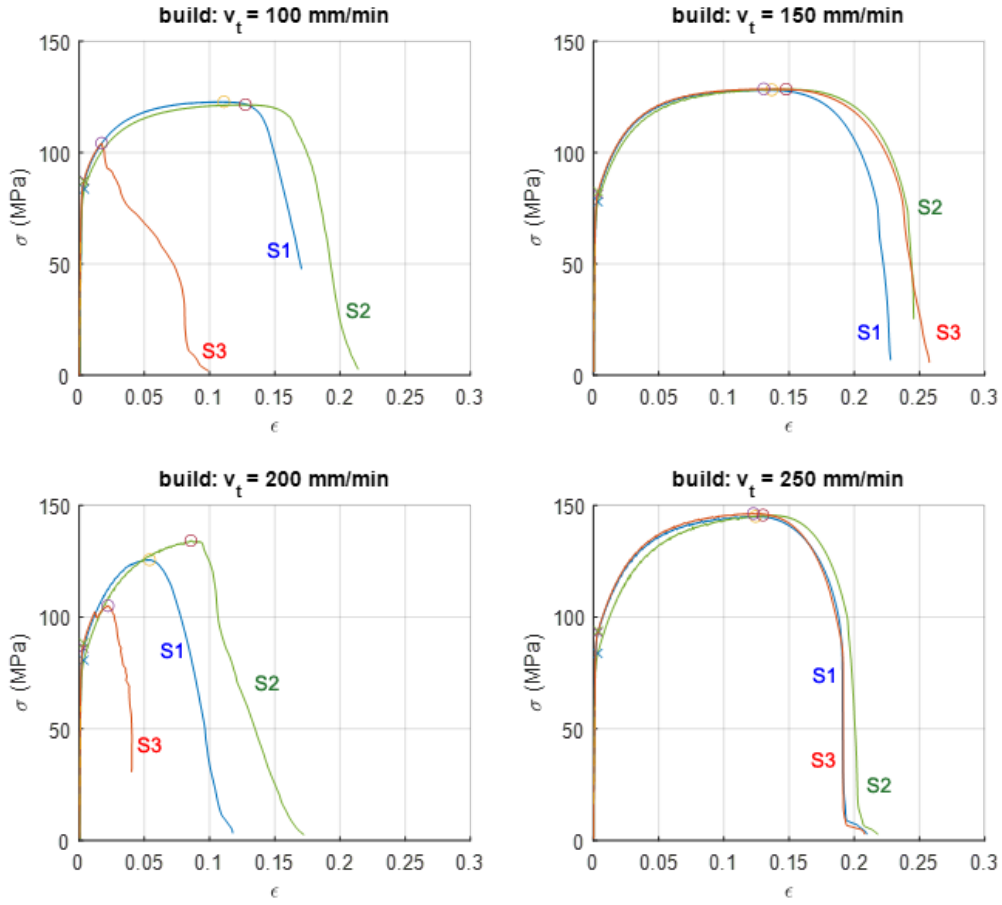

Figure 4.22: Stress-strain curves of vertical tensile tests - Set 2, produced from a FSEAM build with feedstock material AA6060 T6. Tensile samples are located and orientated as depicted in Figure 3.6

The entire second set of tensile tests showed plastic deformation, just as the first set in Section 4.7. Still, some of the vertical samples of experiment E1 and all vertical samples of experiment E3 failed prematurely. The samples from experiment E3 failed relatively fast after plastic deformation, resulting in a small elongation at fracture. This is seen in one sample of experiment E1 as well. Since the samples of Set 2 are taken from the middle part of the build, this premature fracture can not be explained by the warm up phase after the refill phase. In Section 4.10 some fracture surfaces of prematurely fractured samples will be analysed, to see if an indication for this premature break is discovered. Thus, the theory of poor adhesion between layers due to process start-up on the side of the build cannot be confirmed yet denied.

The set of horizontal samples did not show any premature break and the results per print speed show little deviation, indicating consistency throughout the height of the sample. In Figure 4.24, the mechanical properties of the entire second set of tensile samples are given. The blue lines and markings indicate the horizontal samples, red indicates the vertical samples of Set 2.

Comparing the horizontal and vertical samples, it becomes clear that the elongation at fracture is larger for the horizontal samples. The set of horizontal samples are expected to show better results than the vertical samples, since the defects are mainly expected at the interlayer surface. These interface defects are less significant when loaded in the vertical direction. Thus, loaded in-line instead of orthogonal to the defects. This is in agreement with the results of the tensile tests as well, considering that both orientations showed defects in the micro-CT analysis as mentioned in Section 4.8. The horizontal samples showing better results than the vertical samples is an indication that the interlayer bonding is not perfect yet.

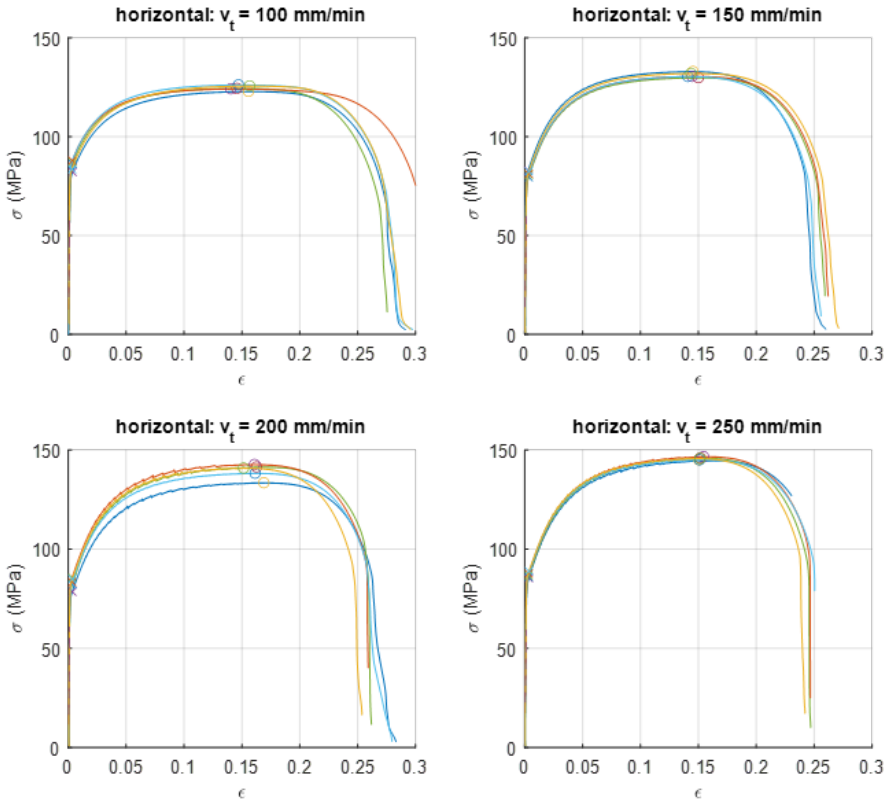

Figure 4.23: Stress-strain curves of horizontal tensile tests - Set 2, produced from a FSEAM build with feedstock material AA6060 T6. Tensile samples are located and orientated as depicted in Figure 3.6

Furthermore, the elasticity modulus and yield strength remain roughly at the same level for all experiments, which is in accordance with the first set of samples as well. The increase in tensile strength as a function of the print speed of the first set of samples is also observed. However, a drop for the vertical samples of experiment E3 is noted, which is logical due to the premature fracture of the samples.

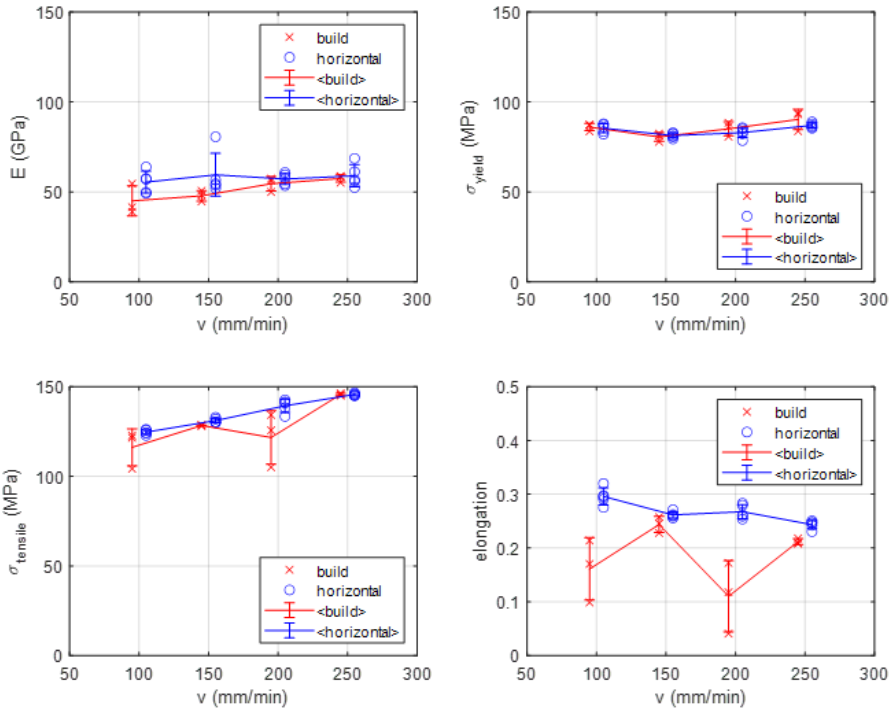

Figure 4.24: Mechanical properties of tensile tests - Set 2, produced from a FSEAM build with feedstock material AA6060 T6, with (E) the elasticity modulus, (σ_{yield}) the yield strength, ($\sigma_{tensile}$) the tensile strength, and (δ) the elongation at fracture. Tensile samples are located and orientated as depicted in Figure 3.6

Comparing the results to the feedstock material, of which the mechanical properties are mentioned in Table 3.2, the following can be noted:

- A decrease in yield strength of ± 40 MPa
- A slight drop in elastic modulus of ± 10 GPa
- Overall, a drop in tensile strength
- An increase in elongation with roughly 17 % strain

In Section 2.3.2 it was mentioned that an increase in elongation at fracture is often related to a drop in tensile strength. If the horizontal samples are compared this is true. However, for the vertical samples there are not enough results without premature fracture to verify this statement.

Last, a prediction for the tensile strength is done according to the hardness-tensile strength relation in Equation 3.1. An estimation of $120\,\mathrm{MPa}$ based on the Vickers hardness combined with the expectation that the tensile strength would be constant for all print velocities was done. However, tensile tests showed an increase in tensile strength with increasing print velocity. The estimated strength is more or less correct for experiment E1.

4.10 Fracture surface

The fracture surfaces of four tensile tests have been reviewed. These samples are selected as followed:

- A sample in the horizontal direction with good tensile test results (Sample 100 L3)
- A sample in the vertical direction with good tensile test results (Sample 150 S1)
- A sample with moderate tensile test results (Sample 100 S2)
- A sample with bad tensile test results (Sample 200 S2)

The reviewed fracture surfaces are depicted in Figure 4.25 and 4.27. Additionally the CT data of the defects in the fracture region is depicted in Figure 4.26 and 4.28. The CT results show the cross sections in front view (FV), side view (SV) and top view (TV).

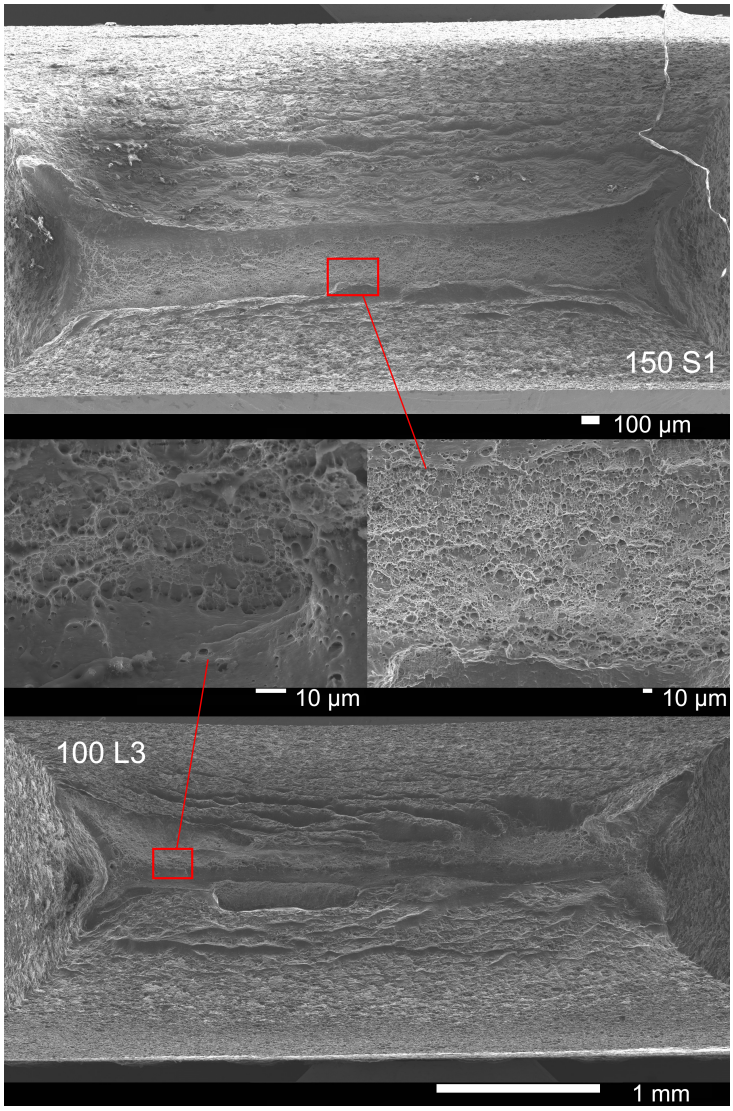

Figure 4.25: Fracture surface of sample 150 S1 and 100 L3 after tensile test. Magnified details of the fracture surfaces are indicated with the red squares

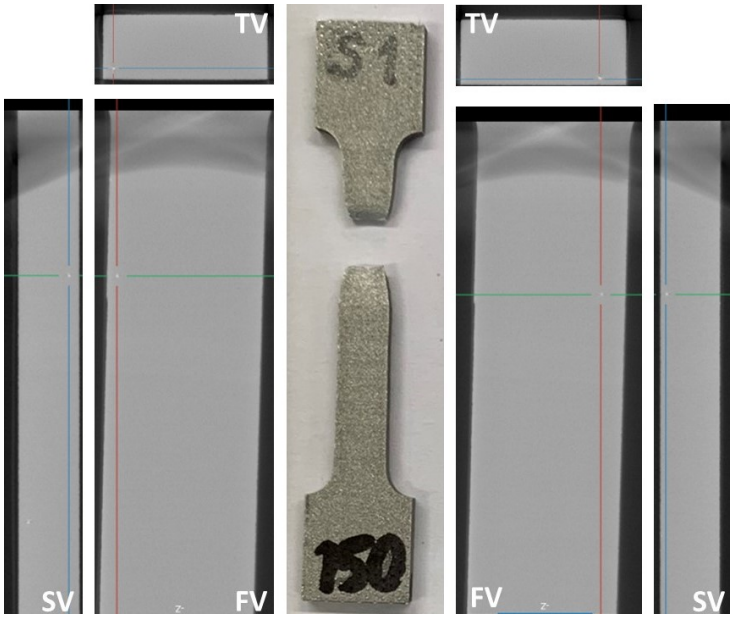

(a) Tensile sample 150 S1

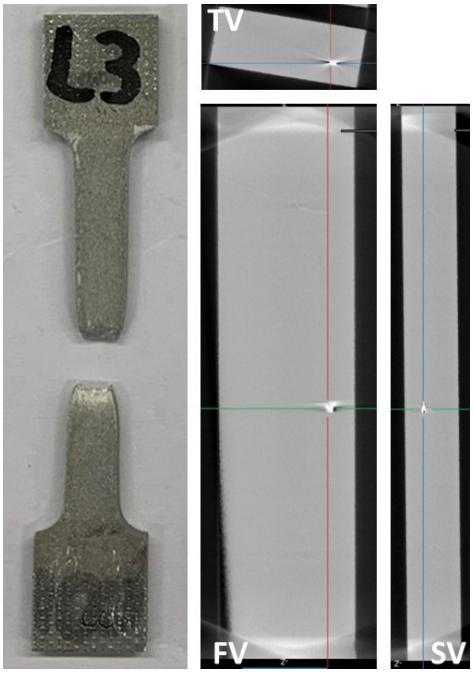

(b) Tensile sample 100 L3

Figure 4.26: Fractured tensile tests and defects observed in micro-CT analysis around the fracture region of sample 150 S1 and 100 L3. CT results show the cross sections in front view (FV), side view (SV) and top view (TV).

In Figure 4.25, it can be seen that the fractures with good tensile test results show a significant reduction in cross section, also known as necking. A closer look reveals a structure of small dents, called dimples. Dimples are an indication of ductile breaks, which means that the material can withstand some plastic deformation before fracturing.

When comparing the horizontal sample (100 L3) to the vertical sample (150 S1), it can be seen that the fracture surface of the horizontal sample is the smallest. Indicating that more plastic deformation and thus elongation at fracture took place in the horizontal sample, which is in line with the tensile test results from Section 4.9.

The micro-CT results of the fracture region of sample 100 L3 and 150 S1 both indicate the presence of contamination; see Figure 4.26. For sample 150 S1 two possible defects are seen near the fracture. However, both are located near the outer surface of the tensile sample, indicating that the fracture is not caused by these defects since necking occurred in this region.

In sample 150 S1 a large defect is seen in the fracture surface region, see Figure 4.26. However, the fracture surface does not indicate a different structure at this location in Figure 4.25. Therefore, the assumption is made that this defect did not cause the fracture.

The reviewed tensile samples that fractured prematurely show a variety in cross-sectional width, see Figure 4.27. However, some necking still occurred. In sample 100 S2 a wider left side of the fracture is seen, indicating less plastic deformation before fracturing than the right side. This could be an indication that the fracture started on the left side. In Figure 4.28, the CT data from the fractured region indicates the presence of a defect on the left side of the fracture as well.

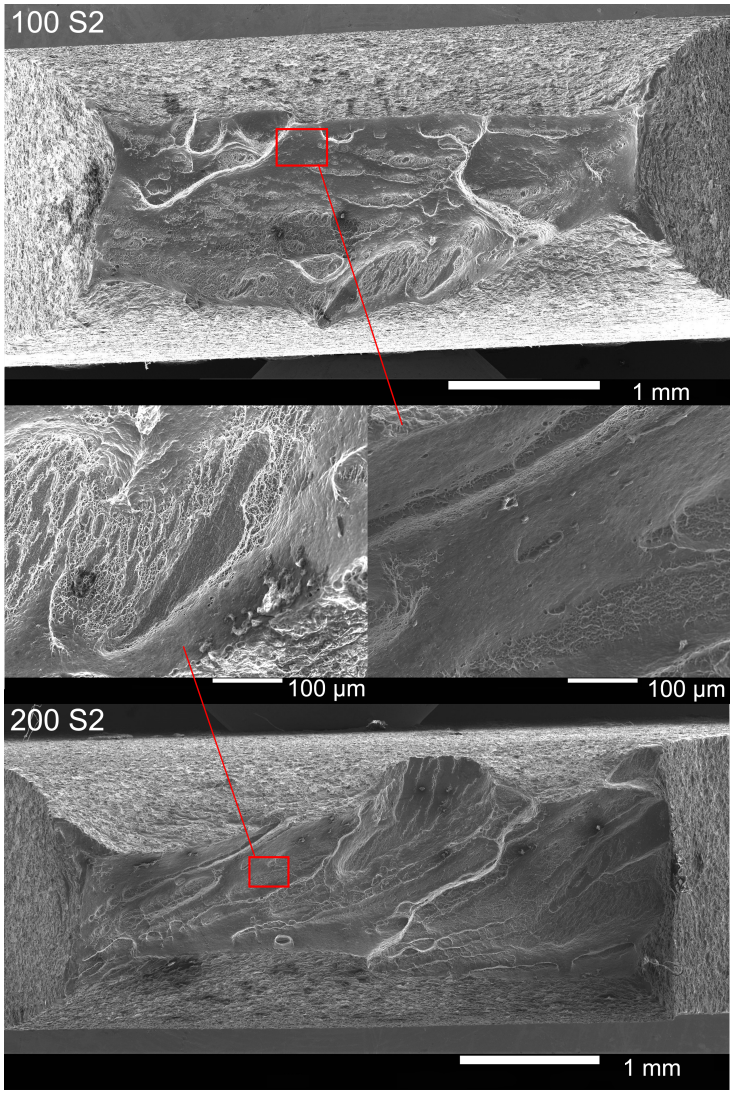

Figure 4.27: Fracture surface of sample 100 S2 and 200 S2 after tensile tests were premature fracture is identified. Magnified details of the fracture surfaces are indicated with the red squares

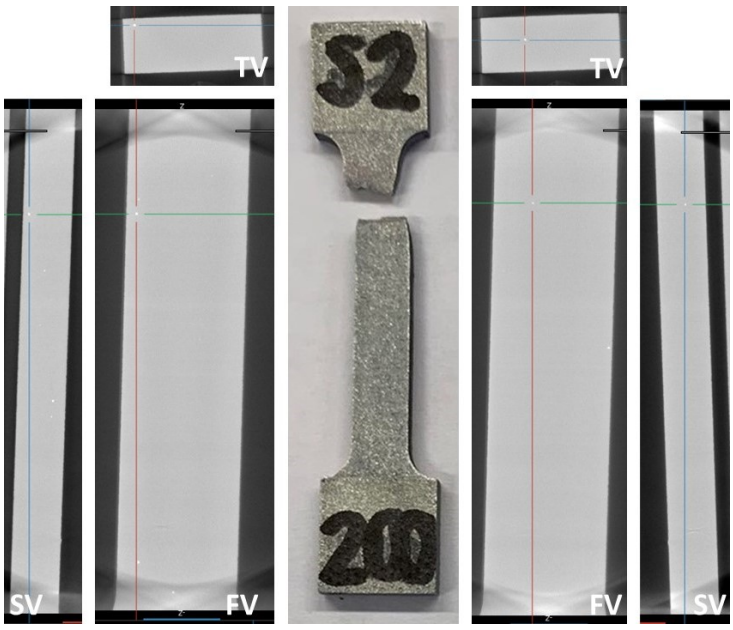

(a) Tensile sample 200 S2

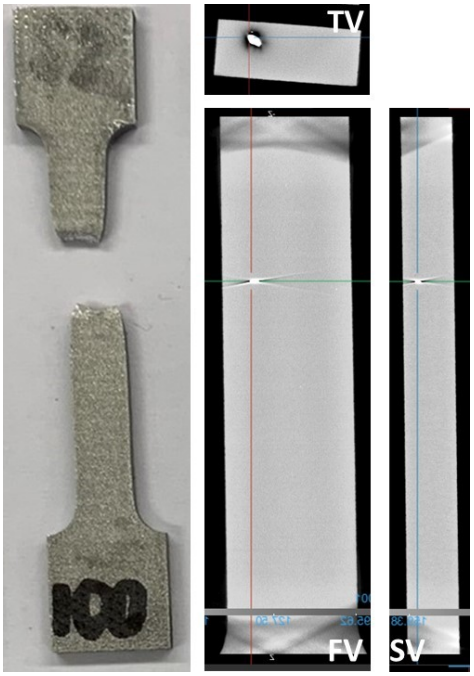

(b) Tensile sample 100 S2

Figure 4.28: Fractured tensile tests and defects observed in micro-CT analysis around the fracture region of sample 200 S2 and 100 S2. CT results show the cross sections in front view (FV), side view (SV) and top view (TV).

The same is seen in sample 200 S2, but here the fracture appears to start from the right side. Again, the CT data of the fracture region is compared to the fracture surface. However, the defects found in the fracture region are small and on the opposite side of the sample. Therefore, these defects are not expected to cause the premature fracture and no clear indication is found.

Next, the structure of the fracture surfaces experiencing premature fracture is discussed. Mixed regions of both flat and dimple rich regions are seen in Figure 4.27. Flat surfaces indicate little plastic deformation of the fracture surface and are seen in brittle fractures where there is little necking. The mix of dimples and flat surfaces indicates both good bonding and sheared surfaces. This may be caused by a defect rather than poor interlayer adhesion in general, as ductile areas are observed as well.

4.11 Precipitates after processing

Combining the results of EBSD analysis, hardness and tensile tests a hypothesis about the precipitate state can be made. After processing, the EBSD results show a grain refinement, while the hardness and tensile strength both decreased. Grain refinement should increase the strength of a material, see Section 2.1.1. So, since the measured mean grain size order is E2-E4-E3-E1 from large to small, a material strength increase in the same order is expected. Reviewing the tensile strength this is not the case. Therefore, it can be concluded that the strength is defined by the precipitates and that these are not in the peak aged state anymore. Additionally, the tensile strength results suggest that the precipitates of higher print speeds are closer to the peak aged state.

This suggestion is supported by the serrations seen in the stress strain curves of experiments E2, E3, and E4. These serrations are caused by either dissolving of the precipitates or by small coherent precipitates in the underaged state. Both scenarios indicate dissolving of the precipitates during the process, which is in agreement with the measured

nozzle temperatures from Table 4.1. However, to conclude if the precipitates are dissolved or underaged additional research is necessary.

4.12 Changes in practice

The big difference in results of the in-situ measurements of experiment E1 compared to the other experiments is remarkable. No clear explanation is found for this difference, but the number of parts in the setup that have been replaced after completion of this experiment is noteworthy. An overview of the work done on the setup is given in Appendix A.

After conducting experiment E1, many problems arose of which the cause was often unclear. Some parts needed replacement and were reproduced. One of these parts was the nozzle, and after replacement it was seen that the available drawing was incorrect. Since the dimensions of the nozzle are closely related to the size of the tool gap, see Figure 1.2, this became smaller. The nozzle and its drawing are adjusted before continuing, but a remark has to be made. The exact dimensions of the previous nozzle were unknown, and since it was destroyed, there is no 100 % certainty that the replacement has the same dimensions.

As mentioned in Section 1.2, a small change in the toolgap could result in noticeably different values for the torque and the feed force. Since no reliable feed force data is available after the changed nozzle, only the torque can be compared. In Table 4.3 it can be seen that the mean torque of experiment E1 is lower than the other experiments. However, it is not that far off experiment E3 and E4. A slightly larger tool gap for experiment E1 might be possible, however it is not likely regarding the similar torque values.

Chapter 5

Thermal model

Additional to the experimental work, a 2D temperature model of the temperature development during the manufacturing of the build has been created. The model is supported with the experimental data collected with the thermocouples in the nozzle (TC 1, TC 2, and TC 3) and the substrate (TC 7 and TC 8). The locations of which can be found in Figure 3.5. With the help of a validated thermal model the relation between the temperature development in the substrate and the print speed can be investigated.

5.1 Modeled process

The modeled process is a simplified 2-dimensional version of the experimental build of a structure as described in Section 3.3. Including a substrate, the start phase, and the refill phase after every layer, but excluding the print head. The deposition of material is simplified to an area at deposition temperature. The size of the area is in accordance with the nozzle diameter.

5.2 Dimensions of the model

The model consists of a 2-dimensional uniform grid of N by M points. Here N indicates the y-direction and M the x-direction. Starting with the substrate only, the four lower rows are nonzero, while all other points are equal to zero. Figure 5.1 shows a scaled-down example; real values can be found in Table 5.1. Layers are printed by adding non-zero points between column S and E, depicted by the light grey blocks. The calculated points of the matrix are located in the middle of the blocks.

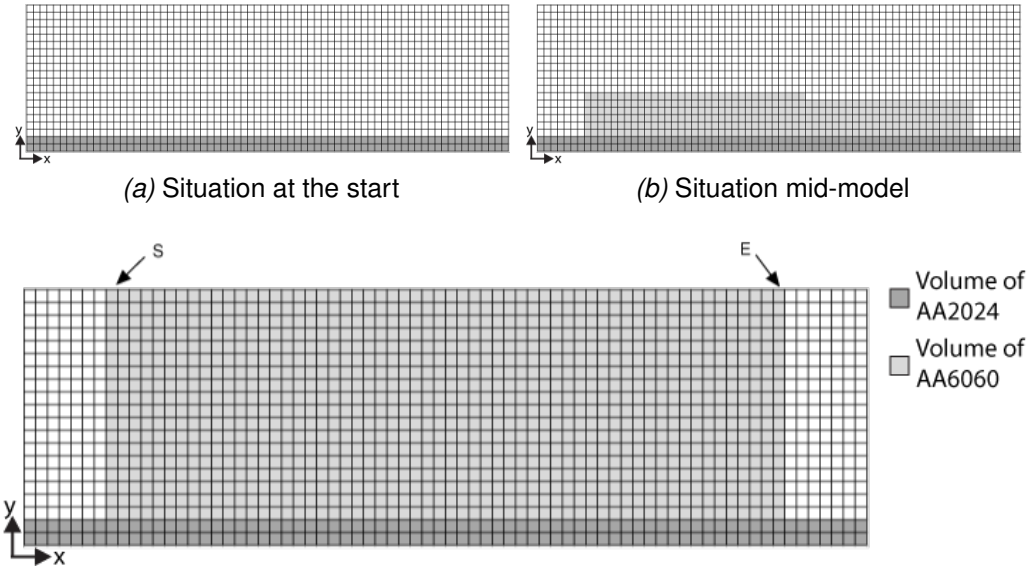

(a) Situation at the start

(b) Situation mid-model

(c) Situation at the end

Figure 5.1: 2-dimensional grid of the model in multiple phases of the build. The squares indicate the volume assigned to one single point in the matrix. Dark grey volume indicates the substrate, light grey the build.

5.3 Modeling approach

The time and place dependent heat transfer equation is employed to simulate the temperature distribution during the deposition of the aluminium in a layer-wise fashion while fabricating a rectangular build.

Table 5.1: Properties used in the model

N	58
M	300
S	61
E	240
Δx	$8.3333 \times 10^{-4}\,\mathrm{m}$
Δy	$0.001\,\mathrm{m}$
Δt	$0.0020\,\mathrm{sec}$
T_∞	$18\,^\circ\mathrm{C}$
h_{air}	$10\,\mathrm{W/m^2K}$
h_{table}	$375\,\mathrm{W/m^2K}$
λ_{AA6060}	$210\,\mathrm{W/mK}$
λ_{AA2024}	$120\,\mathrm{W/mK}$
ρ_{AA6060}	$2700\,\mathrm{kg/m^3}$
ρ_{AA2024}	$3000\,\mathrm{kg/m^3}$
$c_{pAA6060}$	$900\,\mathrm{J/kgK}$
$c_{pAA2024}$	$880\,\mathrm{J/kgK}$

$$\frac{\partial T}{\partial t} = \frac{\lambda}{\rho c_p}\left(\frac{\partial^2 T}{\partial x^2} + \frac{\partial^2 T}{\partial y^2}\right) \tag{5.1}$$

in which T is the temperature in [$^\circ$C], t the time in [sec], λ the thermal conductivity in [$\mathrm{W/m} * \mathrm{K}$], ρ the density in [$\mathrm{kg/m^3}$], c_p the specific heat capacity in [$\mathrm{J/kg} * \mathrm{K}$], and x and y are locations in [m]. The method used in this model is a combination of the finite difference method (Equation 5.2), based on the difference between neighboring points, and the explicit Euler method for time discretization (Equation 5.3).

$$\begin{aligned}
\frac{\partial^2 T}{\partial x^2} + \frac{\partial^2 T}{\partial y^2} &= \frac{\partial}{\partial x}\left(\frac{\partial T}{\partial x}\right) + \frac{\partial}{\partial y}\left(\frac{\partial T}{\partial y}\right) \\
&= \frac{1}{\Delta x}\left(\frac{T_{i,j+1} - T_{i,j}}{\Delta x} - \frac{T_{i,j} - T_{i,j-1}}{\Delta x}\right) + \frac{1}{\Delta y}\left(\frac{T_{i+1,j} - T_{i,j}}{\Delta y} - \frac{T_{i,j} - T_{i-1,j}}{\Delta y}\right) \\
&= \frac{T_{i,j+1} - 2T_{i,j} + T_{i,j-1}}{\Delta x^2} + \frac{T_{i+1,j} - 2T_{i,j} + T_{i-1,j}}{\Delta y^2}
\end{aligned} \tag{5.2}$$

in which j denotes the point in the x-direction, and i the points in y-direction. The model has been verified by comparing it to the exact solution of the thermal penetration depth theory, more information can be found in Appendix D.

$$\int_{t_n}^{t_{n+1}} f(T)\, dt \approx \Delta t f(T(t_n)) \qquad T^{n+1} = T^n + \Delta t f(T^n) \tag{5.3}$$

Furthermore, the boundary conditions described to the system are based on convection with a varying enthalpy value for air and the table. A schematic overview of the applied boundary conditions is shown in Figure 5.2. Where λ is the heat transfer coefficient of AA2024 and AA6060 respectively, and h the enthalpy of the air and the table. Where h_air is based on a previous models from the Production Technology chair [42], h_table has been determined by matching the experimental data from TC 1, TC 2, and TC 3. Values can be found in Table 5.1. Furthermore, the convection boundary condition is verified by comparing it with the stable convection equation; more information is provided in Appendix D.

Additional boundary conditions are coupled to the material deposition. The print head is simplified to a deposition length of $10.5\,\mathrm{mm}$, which equals 12 points, and is moved to the side according to the print speed. The deposition height is $1\,\mathrm{mm}$, which equals 1 point. Furthermore, the deposition temperature is kept constant during print phase, and a linear decrease of $200\,^{\circ}\mathrm{C}$ is assigned to a stationary deposition location at the end of every layer. This is done to mimic the refill phase where little to no material is extruded. Since contact with the material inside the printhead is maintained the heat input is lowered but not equal to zero because the screw is still rotating.

Figure 5.2: Convection boundary conditions assigned to the finite difference model

5.4 Experimental data

To make a good comparison between the experimental data and the model, more insight in the substrate temperature of the experiments is necessary. In Figure 5.3 the experimental data of experiment E2 - TC 7 is depicted. Where the difference between the start phase and the main build is indicated, and 2 printed layers in the main build are highlighted.

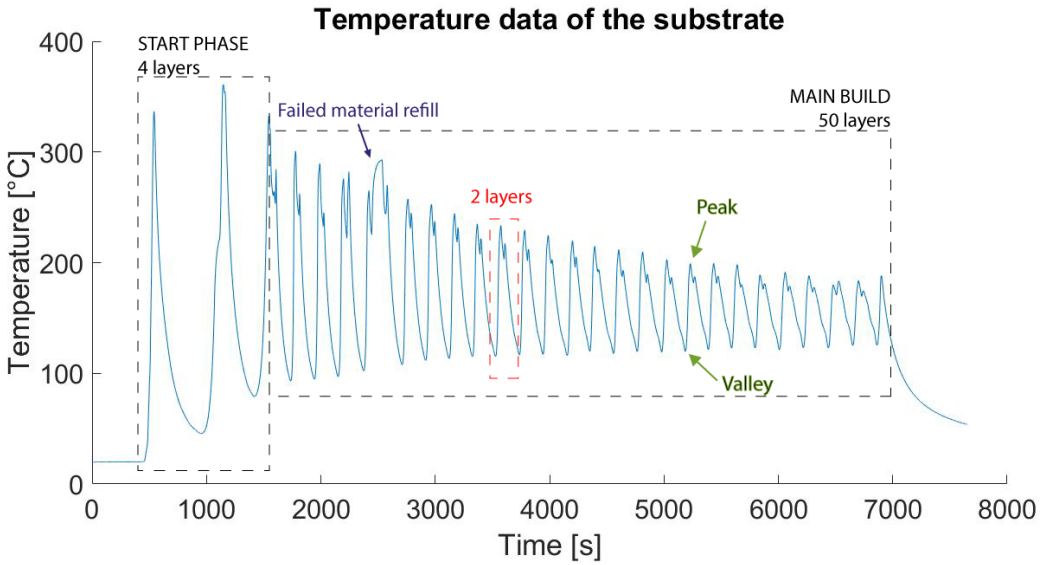

(a) Substrate temperature over time

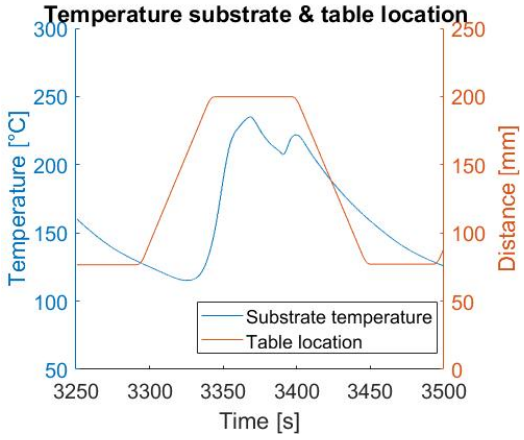

(b) Two layers of substrate temperature and table movement over time

Figure 5.3: Experimental data of E2

In the start phase in Figure 5.3a, higher peak temperatures are seen, which can be explained by longer layers, adding more energy to the build before the next material refill. Furthermore, two events are indicated during the build; peaks get lower while valleys become higher. Both events can be explained. During the build, the newly deposited material is

placed further and further away from the thermocouple. Since the distance becomes larger, the temperature becomes lower. Next, the higher valley temperatures. Every layer more energy is added to the build. This energy is indicated by the increasing temperature. During the material refill moments some of this energy leaves the build by convection and conduction into the table. In the end it is a story of energy balance: the temperature is determined by the amount of heat put in by the building process and lost by convection and conduction. Since more energy is put in than can be lost via convection and conduction, the internal energy increases and results in higher valleys.

In Figure 5.3b, the table location is plotted within the indicated 2 layers as well. The horizontal lines indicate material refill, while the slopes indicate the print phases. The first temperature peaks lags behind the stop of the table movement. This can be explained by the thermocouple which is located opposite from the build edge. It takes time for the heat wave to arrive at the thermocouple. The second layer ends on the side of the thermocouple. Since the distance to the thermocouple is close, this peak is nearly located at the start of the table movement. The second peak is regularly smaller, which can be explained by the energy already in the build. After material refill, it takes some time before the temperature is back at the original values during continuation of the manufacturing process.

Additionally, a failed material refill is indicated in Figure 5.3a, and it can be seen by the excess material at the lower left of the build in Figure 4.7b as well. This is a clear example of manual errors which occur during the process. Most of the steps during printing are manually timed, while the timing in the model is kept constant. Therefore, the timing of the model is not entirely the same as the experimental data. Moreover, the long layers in the starting phase are not included in the model. However, the lower print speed of these layers is included.

5.5 Comparison to experimental data

A comparison is made between the simulated temperature distribution and the measured one to verify the model. The compared model makes use of the time and temperature measurements. The high end of the mean nozzle temperatures in Table 4.1 are used as deposition temperatures of the material, and the wait time is based on the experimental time data. Both input arguments vary per experiment and are given in Table 5.2. After the model is complete, the experimental data from TC 7 or TC 8 is plotted against the substrate temperature in the model. It is concluded that the locations of the thermocouples are not directly under the build, and that the distance to the build varies. Figure 5.4 gives a schematic overview of the indicated distance, and the values per experiment can be found in Table 5.2. A remark has to be given that the exact distance is unknown. An estimation is made based on the pictures taken from the builds, because the builds have been cut into smaller pieces for analysis.

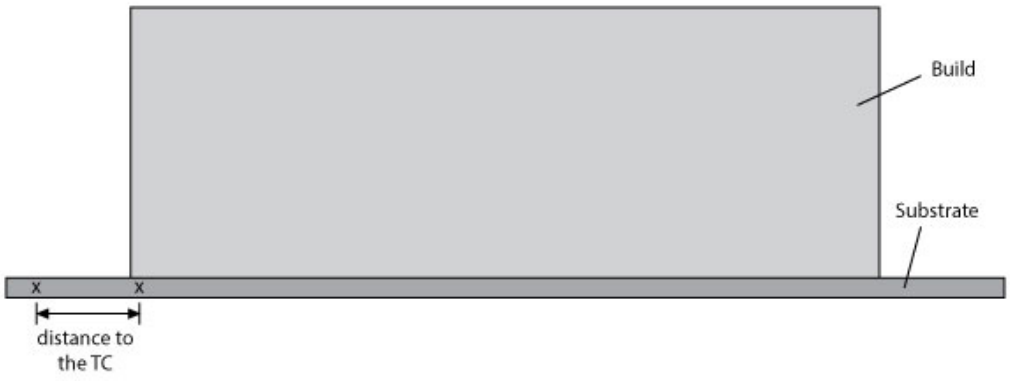

Figure 5.4: Schematic overview of the thermocouple location used in the model

Once the local maximum and minima of the 2 dimensional model are plotted against the experimental data it can be seen that the model fits

Table 5.2: Values used in the model, taken from the experimental data

	$100\,\mathrm{mm/min}$	$150\,\mathrm{mm/min}$	$200\,\mathrm{mm/min}$	$250\,\mathrm{mm/min}$
Deposition temperature [°C]	420	506	521	535
Wait time [sec]	57.8	45.3	47.2	46
Distance TC [$\#ofpoints$]	30	16	24	18

the experimental data relatively good, as seen in Figure 5.5 and 5.6. Some differences between the model and reality were already mentioned in Section 5.4. An additional explanation is sought in the assumption of a 2D model, which assumes an infinitely thick body instead of a wall of approximately $15\,\mathrm{mm}$. Thus, convection out of the x-y plane is not taken into account, which becomes larger with a growing build. This might explain the higher mean of the model at the end of the build. Additionally, the experimental results of experiment E4 deviate more than the others. The build cooled down much quicker in between layers than the model. A possible explanation would be the shorter duration of the experiment. Since the table slowly heats up during the experiment it acts as an energy storage. The hotter the table becomes, the less heat from the build can be stored in the table. Since no temperature data of the table is available, this can not be to verified.

5.6 Print velocity-build temperature relation

The thermal model is used to simulate the influence of the print velocity on the substrate temperature. The lower layers of the build are expected to decrease in temperature with increasing print speed. The hypothesis is based on the amount of heat that is added to the build. If the deposition temperature and the refill time are kept constant, this means that the rate of heat added to the build is constant over the different print speeds. Since a higher print speed results in a shorter build time, less heat is added to the build overall. This should results in lower substrate temperatures for higher print velocities.

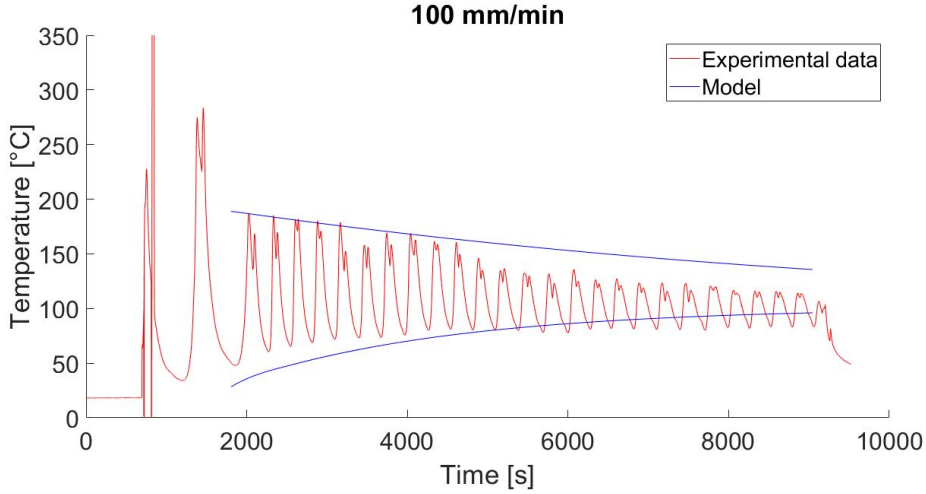

(a) $100\,\mathrm{mm/min}$

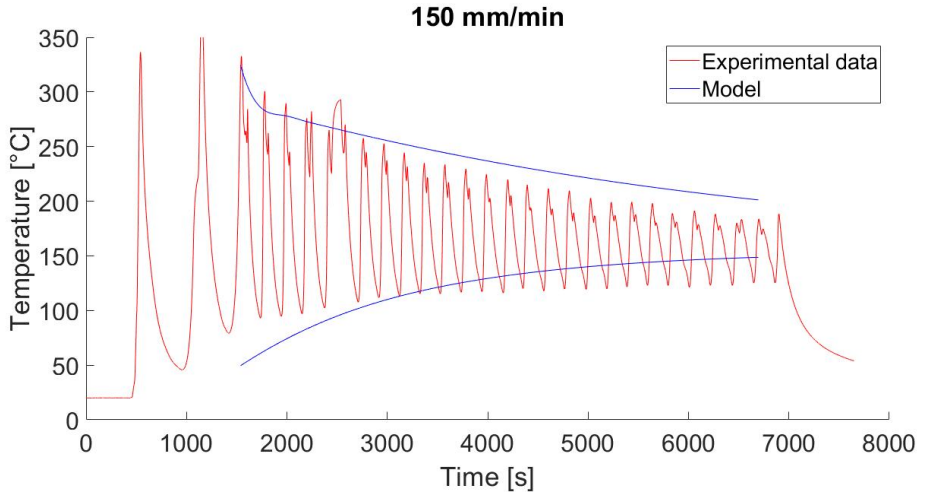

(b) $150\,\mathrm{mm/min}$

Figure 5.5: Part 1: Experimental data of the substrate temperature, compared to the maxima and minima values of the substrate temperature of the model

The maxima en minima of the substrate temperature of four different print speeds are plotted in Figure 5.7. A constant deposition temperature of $500\,^{\circ}\mathrm{C}$ and a wait time of $45\,\mathrm{sec}$ is chosen. The thermocouple location is assigned to column S, directly under the build.

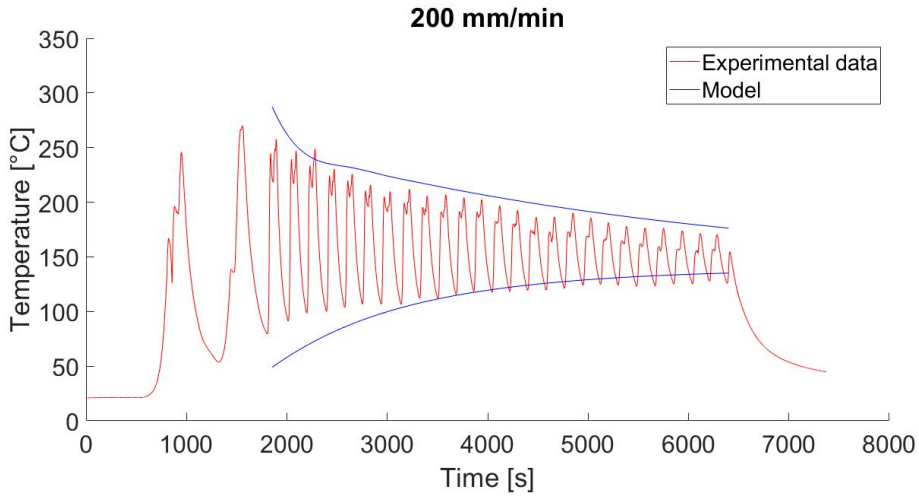

(a) $200\,\mathrm{mm/min}$

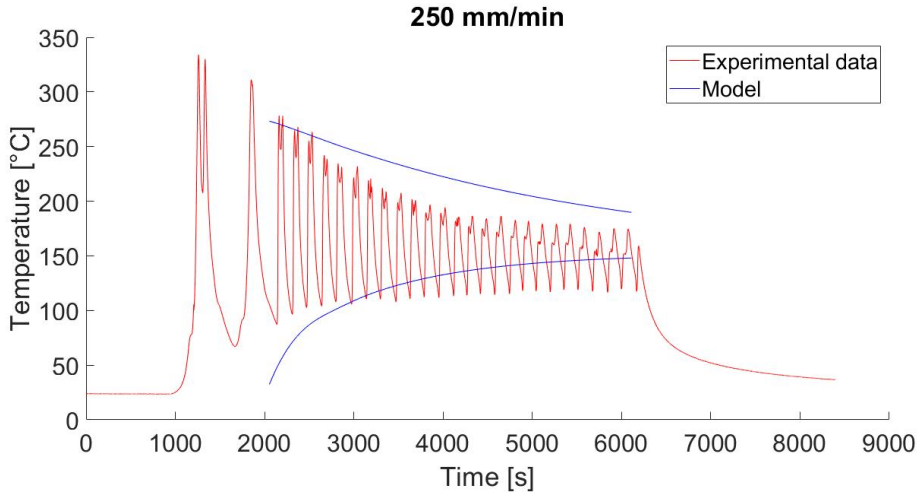

(b) $250\,\mathrm{mm/min}$

Figure 5.6: Part 2: Experimental data of the substrate temperature, compared to the maxima and minima values of the substrate temperature of the model

The maxima en minima plots indicate a larger bandwidth for lower print speeds. The lower maximum with increasing print speed can be explained according to the hypothesis. Due to the constant heat rate, a faster processes results in a lower maximum temperature.

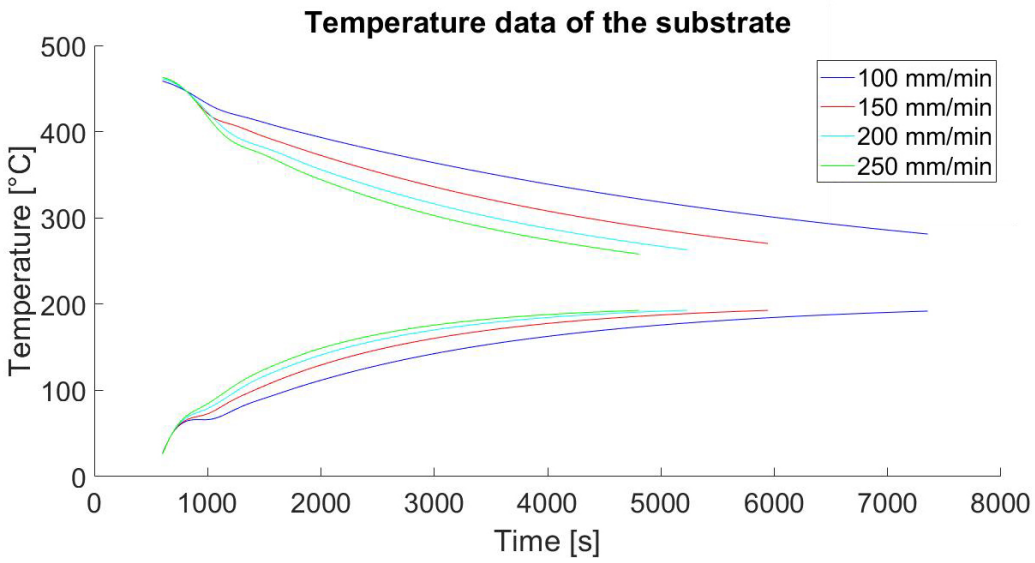

Figure 5.7: Print velocity-substrate temperature relation

The expectation does not explain the higher minima. A possible explanation is the amount of convection and conduction which takes place. The temperature is measured at the thermocouple location. As the nozzle deposits a layer of material, it passes by the thermocouple location. When the nozzle reaches the end of the first layer, the next layer is deposit on top, and the nozzle will return towards the thermocouple location. The time interval between the instances where the nozzle passes the thermocouple is dependent on the printing speed, so a higher print speed results in a shorter time interval. Since the time interval is shorter, the build can lose less energy to its surroundings, resulting in a higher lower limit.

Chapter 6

Conclusions and recommendations

6.1 Conclusions

The answer to the research question is formulated using the previously described literature, findings from the experimental work, and the thermal model.

The research question:
"What influence does the print speed have on the microstructure and mechanical properties of FSEAM builds made from AA6060 T6?"

Four successful builds were produced and reviewed, with printing speeds of 100, 150, 200, and 250 mm/min. The following conclusions were drawn from the analysis of the build and the thermal model.

- The in-situ measurement showed an increasing trend in the nozzle temperature with increasing print speed. Furthermore, the nozzle temperatures of experiments E2, E3, and E4 are located in the solid solution phase of the phase diagram, which might cause solutionizing of the precipitates during the process.
- Analysis of the builds showed no macro-scale defects. Microscopy

showed microscale defects of approximately $50\,\mu\mathrm{m}$ for the builds produced at 150, 200, and $250\,\mathrm{mm/min}$ builds. The build produced at $100\,\mathrm{mm/min}$ showed larger micro-cracks as well.

- The electron backscatter diffraction revealed a grain refinement for all builds, indicating recrystallisation. However, no trend in grain size regarding the print speed is noticed. An explanation can be found in the temperature of the build in process, which remains close to the critical grain growth temperature.
- Regarding mechanical tests, the hardness of all experiments decreased by approximately 50 %, and the tensile tests showed a decrease in the yield strength and the tensile strength, combined with an increase in elongation at fracture compared to the feedstock material. Since this is in contrast with the grain refinement, it can be concluded that the precipitates are not in their peak aged state after processing.
- After mutual comparison of the experiments, the tensile test results show an increase in tensile strength with increasing printing speed. However, no influence of the print speed is seen on the elastic modulus as this remain roughly at the same level for all builds.
- A difference in tensile test results is observed between samples extracted in the build direction and along the deposition direction. From every build both horizontal and vertical tensile samples were extracted and compared. All samples showed plastic deformation. However, many vertical samples broke prematurely, while no premature fracture is seen in the horizontal samples. Since micro-CT analysis revealed defects in both orientations of the the tensile samples, it can be concluded that the influence of these defects is negligible in the horizontally orientated samples. This can be explained by interlayer areas being loaded in length. Additionally, the elongation at fracture is greater for horizontal samples. These are indications that the interlayer bonding is not perfect and the process is in need for further improvements.
- Furthermore, a closer look at the stress-strain curves revealed a sawtooth pattern, known as serrated flow. The sawtooth pattern is seen for higher print speeds (150, 200, and $250\,\mathrm{mm/min}$). Combining

this with the nozzle temperatures located in the solid-solution phase, a hypothesis is made that the precipitates solutionize in the print head. This would occur when the material is transported by the rotational tool, resulting in precipitates that have not formed yet or are in the underaged state after deposition. However, more research is necessary to prove this statement.

- Last, the 2D thermal model concluded a decrease in the maximum substrate temperature and an increase in the minimum substrate temperature, with an increasing print speed when all other parameters remain constant.

In summary, the nozzle temperature and the tensile strength show increasing trends with an increased print speed in experimental work. Other results have not shown clear trends regarding the print speed. However, since only one build per print speed is produced, more experiments have to be performed to identify small trends and/or verify these results.

6.2 Recommendations

Based on the work presented, some recommendations are made for future work. These recommendations can be divided into the following categories: Experimental work, additional analysis of the builds, and the thermal model.

Experimental work

- Experiments should be performed with the same setup, without intermediate cleaning. This assures the same thermocouple location and tool gap for all experiments. Small changes in thermocouple location or the size of the tool gap may cause unanticipated changes in the temperature and/or heat generation.
- Additionally, it is wise to check the existing technical drawings of crucial elements in the setup to make sure these are up to date. In case of failure, such as in experiment F4 (see Appendix A), the parts can be replaced with ease.

- Cleaning the feed material. Up until now, the feed material had to be cut into small pallets. In the workshop, the pallets are sawn on a general saw that is used for other materials as well. Contaminations can stick to the pallets and are inserted with the pallet as feedstock material. However, ideally the need to cut the feedstock into small pallets is removed completely by changing to a continuous feed system.
- Finally, there is the desire to move to a more automated system. The movement of the table and the print head is now done by manually pressing and turning buttons, which does not offer precision. The same holds for the feed rate at which the material is fed to the screw. All are crucial for material flow and thus the pressure necessary to create a good bond between layers. By moving to an automated system a more constant deposition volume and feed rate can be achieved.

Additional research

- Further investigation of the contaminations seen in the micro CT results. A quick EDX analysis is performed without success. These contaminations might cause defects, and therefore it is necessary to identify their composition as a first step in figuring out where these contaminations come from and how to prevent them. Two theories are formed; these contaminations are inserted with the feedstock, or the contaminations are assigned to the wear of the tool.
- Most importantly, more research is necessary to form a well-substained theory about the precipitate state. Two methods can be considered; transmission electron microscopy (TEM), or artificial ageing combined with tensile tests. The first being a microscopy method which can identify precipitates. From the size and the distribution of the precipiates it can be estimated in which state they are. The second method is by artificially ageing the material, as explained in Section 2.1.1. Tensile samples can be aged, for multiple time durations, and tested to find the highest tensile strength. Relating this to the existing literature and a known composition will indicate the state of the precipitates at the start.

Thermal model

- Measure the exact distance to the thermocouple. The distance between the deposition area of the build and the location of the thermocouple in the substrate is now unknown. In the comparison of the model with the experimental data an estimation of this distance is made. By knowing the exact distance of the thermocouple to the build, the model can be verified accurately. This can be achieved by milling the substrate plates until the thermocouple becomes visible. Additionally, the amount of thermal fixing paste between the aluminium and the thermocouple should be reviewed as well. Indicating how well the heat conduction could take place.
- Switch to a 3 dimensional model which includes the in plane heat conduction. A 3-dimensional model is expected to result in a better approximation, and thus giving a better indication of the thermal history.

Bibliography

[1] T. DebRoy, H. Wei, J. Zuback, *et al.*, "Additive manufacturing of metallic components – process, structure and properties," *Progress in Materials Science*, vol. 92, pp. 112–224, 2018, ISSN: 0079-6425. DOI: https://doi.org/10.1016/j.pmatsci.2017.10.001. [Online]. Available: https://www.sciencedirect.com/science/article/pii/S0079642517301172.

[2] S. Saxena and A. Kar, "A review of solid-state additive manufacturing processes," *Transactions of the Indian National Academy of Engineering*, vol. 6, Sep. 2021. DOI: 10.1007/s41403-021-00270-7.

[3] J. Martin, B. Yahata, J. Hundley, J. Mayer, T. Schaedler, and T. Pollock, "3d printing of high-strength aluminium alloys," *Nature*, vol. 549, pp. 365–369, Sep. 2017. DOI: 10.1038/nature23894.

[4] N. Tuncer and A. Bose, "Solid-state metal additive manufacturing: A review," *JOM*, vol. 72, Jul. 2020. DOI: 10.1007/s11837-020-04260-y.

[5] S. Lathabai, "Chapter 2 - additive manufacturing of aluminium-based alloys and composites," in *Fundamentals of Aluminium Metallurgy*, ser. Woodhead Publishing Series in Metals and Surface Engineering, R. N. Lumley, Ed., Woodhead Publishing, 2018, pp. 47–92, ISBN: 978-0-08-102063-0. DOI: https://doi.org/10.1016/B978-0-08-102063-0.00002-3. [Online]. Available: https://www.sciencedirect.com/science/article/pii/B9780081020630000023.

[6] W. E. Frazier, "Metal additive manufacturing: A review," *Journal of Materials Engineering and Performance*, vol. 23, pp. 1917–1928, 2014. DOI: 10.1007/s11665-014-0958-z. [Online]. Available:

https://link.springer.com/article/10.1007/s11665-014-0958-z#citeas.

[7] W. E. King, H. D. Barth, V. M. Castillo, *et al.*, "Observation of keyhole-mode laser melting in laser powder-bed fusion additive manufacturing," *Journal of Materials Processing Technology*, vol. 214, no. 12, pp. 2915–2925, 2014, ISSN: 0924-0136. DOI: https://doi.org/10.1016/j.jmatprotec.2014.06.005. [Online]. Available: https://www.sciencedirect.com/science/article/pii/S0924013614002283.

[8] K. Darvish, Z. Chen, and T. Pasang, "Reducing lack of fusion during selective laser melting of cocrmo alloy: Effect of laser power on geometrical features of tracks," *Materials & Design*, vol. 112, pp. 357–366, 2016, ISSN: 0264-1275. DOI: https://doi.org/10.1016/j.matdes.2016.09.086. [Online]. Available: https://www.sciencedirect.com/science/article/pii/S0264127516312679.

[9] "Printability of alloys for additive manufacturing.," *Sci Rep.*, vol. 6, 2016. DOI: 10.1038/srep19717.. [Online]. Available: https://www.ncbi.nlm.nih.gov/pmc/articles/PMC4726422/.

[10] A. van der Stelt, T. Bor, B. Geijselaers, R. Akkerman, and T. van den Boogaard, "Cladding of advanced al alloys employing friction stir welding," *Key Engineering Materials*, vol. 554-557, pp. 1014–1021, 2013, ISSN: 0924-0136. DOI: https://doi.org/10.4028/www.scientific.net/KEM.554-557.1014. [Online]. Available: https://www.scientific.net/KEM.554-557.1014.

[11] V. Dolas, *Friction screw extrusion additive manufacturing: Parameter study*, Master Thesis, 2021.

[12] R. Ariës, *Exploratory research of friction stir extrusion additive manufacturing using aa6060 t6*, Master Thesis, 2021.

[13] N. Masselink, *Friction screw extrusion: An exploratory research to the relations between process parameters, microstructure and mechanical properties*, Master Thesis, 2021.

[14] P. Meyer, *Material properties of friction screw extrusion additive manufactured aa6060*, Bachelor Thesis, 2019.

[15] "4 - strengthening of metal alloys," in *Introduction to Aerospace Materials*, A. P. Mouritz, Ed., Woodhead Publishing, 2012, pp. 57–90, ISBN: 978-1-85573-946-8. DOI: https://doi.org/10.1533/9780857095152.57. [Online]. Available:

https://www.sciencedirect.com/science/article/pii/B9781855739468500042.

[16] M. K. en Marc Pallada, *Materiaalkunde voor technici*. Academic Service, 2009, ISBN: 9789039524664.

[17] J. William D. Callister, *Fundamentals of Materials Science and Engineering*. John Wiley & Sons, Inc., 2001.

[18] *How to visually understand that dislocation moves on a slip plane?* Physics Stack Exchange. eprint: https://physics.stackexchange.com/q/408234. [Online]. Available: https://physics.stackexchange.com/q/408234.

[19] *The aluminium automotive manual - materials - alloy constitution*, 2022.

[20] M. Gedeon, "Grain size and material strength," *Technical Tidbits*, no. 5, 2010. [Online]. Available: https://materion.com/-/media/files/alloy/newsletters/technical-tidbits/issue-no-15---grain-size-and-material-strength.pdf.

[21] T. Sheppard, "Extrusion of aluminium alloys," *SPRINGER-SCIENCE+BUSINESS MEDIA, B.V.*, 1999. DOI: 10.1007/978-1-4757-3001-2. [Online]. Available: https://www.daboosanat.com/wp-content/uploads/2018/02/0012-Extrusion-of-Aluminium-Alloys.pdf.

[22] B. Milkereit, L. Jonas, C. Schick, and O. Kessler, "The continuous cooling precipitation diagram of an aluminum alloy en aw-6005a," *HTM J. Heat Treatm. Mat.*, vol. 65, pp. 159–171, Mar. 2010.

[23] A. Onat, "Effects of artificial aging heat treatment on mechanical properties and corrosion behaviour of aa6xxx aluminium alloys," *Journal of Chemical Engineering*, vol. 9, pp. 17–23, 2018.

[24] M. Bobby Kannan, P. Bala Srinivasan, and V. Raja, "8 - stress corrosion cracking (scc) of aluminium alloys," in *Stress Corrosion Cracking*, ser. Woodhead Publishing Series in Metals and Surface Engineering, V. Raja and T. Shoji, Eds., Woodhead Publishing, 2011, pp. 307–340, ISBN: 978-1-84569-673-3. DOI: https://doi.org/10.1533/9780857093769.3.307. [Online]. Available: https://www.sciencedirect.com/science/article/pii/B9781845696733500080.

[25] D. S. MacKenzie, "Heat treatment of aluminum vi – artificial aging," 2021. [Online]. Available: https://thermalprocessing.com/heat-treatment-of-aluminum-vi-artificial-aging/.

[26] S. Biswas, P. Gautam, A. Shukla, and D. Chouhan, "Dynamic recrystallization and its effect on microstructure and texture evolution in magnesium alloys," *Encyclopedia of Smart Materials*, pp. 476–481, 2022. DOI: 10.1016/B978-0-12-815732-9.00016-4.

[27] D. Raabe, "23 - recovery and recrystallization: Phenomena, physics, models, simulation," in *Physical Metallurgy (Fifth Edition)*, D. E. Laughlin and K. Hono, Eds., Fifth Edition, Oxford: Elsevier, 2014, pp. 2291–2397, ISBN: 978-0-444-53770-6. DOI: https://doi.org/10.1016/B978-0-444-53770-6.00023-X. [Online]. Available: https://www.sciencedirect.com/science/article/pii/B978044453770600023X.

[28] J. Lv, J.-H. Zheng, V. A. Yardley, Z. Shi, and J. Lin, "A review of microstructural evolution and modelling of aluminium alloys under hot forming conditions," *Metals*, vol. 10, no. 11, 2020, ISSN: 2075-4701. DOI: 10.3390/met10111516. [Online]. Available: https://www.mdpi.com/2075-4701/10/11/1516.

[29] W. Smith, J. Hashemi, and F. Presuel-Moreno, *Foundations of materials science and engineering*. Mcgraw-Hill Publishing, 2006.

[30] V. G. Fernandez, *Dynamic recrystallization: Multiple peak and monotonic stress behavior*, 2004. [Online]. Available: https://www.tesisenred.net/bitstream/handle/10803/6043/09Vggf09de11.pdf?sequence=9.

[31] M. Azarbarmas, S. S. Mirjavadi, A. Ghasemi, and A. M. Hamouda, "A combined method to model dynamic recrystallization based on cellular automaton and a phenomenological (cap) approach," *Metals*, vol. 8, no. 11, 2018, ISSN: 2075-4701. DOI: 10.3390/met8110923. [Online]. Available: https://www.mdpi.com/2075-4701/8/11/923.

[32] M. Puviyarasan, L. Karthikeyan, C. Gnanavel, and K. Dhineshkumar, "A critical review on friction stir based processes," in *Proceedings of the International Conference for Phoenixes on Emerging Current Trends in Engineering and Management (PECTEAM 2018)*, Atlantis Press, 2018, ISBN: 978-94-6252-492-7. DOI: https://doi.org/10.2991/pecteam-18.2018.46. [Online]. Available: https://doi.org/10.2991/pecteam-18.2018.46.

[33] Z. Y. Ma, A. H. Feng, D. L. Chen, and J. Shen, "Recent advances in friction stir welding/processing of aluminum alloys: Microstructural evolution and mechanical properties," *Critical Reviews in Solid State*

and Materials Sciences, vol. 43, no. 4, pp. 269–333, 2018. DOI: 10.1080/10408436.2017.1358145. eprint: https://doi.org/10.1080/10408436.2017.1358145. [Online]. Available: https://doi.org/10.1080/10408436.2017.1358145.

[34] K. Li, X. Liu, and Y. Zhao, "Research status and prospect of friction stir processing technology," *Coatings*, vol. 9, no. 2, 2019, ISSN: 2079-6412. DOI: 10.3390/coatings9020129. [Online]. Available: https://www.mdpi.com/2079-6412/9/2/129.

[35] A. van der Stelt, *Friction surface cladding - development of a solid state cladding process*, PhD Thesis, 2014.

[36] M. Mahmoodi, K. Tahmasbi, and M. Zaroodi, "Microstructure and mechanical characterization of al–sic mmc tube produced via friction stir back extrusion," *Transactions of the Indian Institute of Metals*, vol. 74, pp. 2609–2620, 2021. DOI: https://doi.org/10.1007/s12666-021-02325-3. [Online]. Available: https://link.springer.com/article/10.1007/s12666-021-02325-3#citeas.

[37] A. P. Zykova, S. Y. Tarasov, A. V. Chumaevskiy, and E. A. Kolubaev, "A review of friction stir processing of structural metallic materials: Process, properties, and methods," *Metals*, vol. 10, no. 6, 2020, ISSN: 2075-4701. DOI: 10.3390/met10060772. [Online]. Available: https://www.mdpi.com/2075-4701/10/6/772.

[38] D. Yadav and R. Bauri, "Effect of friction stir processing on microstructure and mechanical properties of aluminium," *Materials Science and Engineering: A*, vol. 539, pp. 85–92, 2012, ISSN: 0921-5093. DOI: https://doi.org/10.1016/j.msea.2012.01.055. [Online]. Available: https://www.sciencedirect.com/science/article/pii/S0921509312000913.

[39] D. Jacquin and G. Guillemot, "A review of microstructural changes occurring during fsw in aluminium alloys and their modelling," *Journal of Materials Processing Technology*, vol. 288, p. 116 706, 2021, ISSN: 0924-0136. DOI: https://doi.org/10.1016/j.jmatprotec.2020.116706. [Online]. Available: https://www.sciencedirect.com/science/article/pii/S0924013620301205.

[40] Z. Y. Ma, A. H. Feng, D. L. Chen, and J. Shen, "Recent advances in friction stir welding/processing of aluminum alloys: Microstructural evolution and mechanical properties," *Critical Reviews in Solid State and Materials Sciences*, vol. 43, no. 4, pp. 269–333, 2018. DOI: 10.

1080/10408436.2017.1358145. eprint: https://doi.org/10.1080/10408436.2017.1358145. [Online]. Available: https://doi.org/10.1080/10408436.2017.1358145.

[41] H. Chen, J. Chen, S. Xu, Y. Zhao, X. Meng, and Y. Xie, "Wire-based friction stir additive manufacturing toward field repairing," *Welding Journal*, Sep. 2022. DOI: 10.29391/2022.101.019.

[42] S. Liu, T. Bor, A. Van der Stelt, *et al.*, "Friction surface cladding: An exploratory study of a new solid state cladding process," *Journal of Materials Processing Technology*, vol. 229, pp. 769–784, 2016, ISSN: 0924-0136. DOI: https://doi.org/10.1016/j.jmatprotec.2015.10.029. [Online]. Available: https://www.sciencedirect.com/science/article/pii/S0924013615301813.

[43] N. Mathew, I. Dinaharan, V. Santhiyagu, and N. Murugan, "Microstructure and mechanical characterization of aluminum seamless tubes produced by friction stir back extrusion," *Transactions of the Indian Institute of Metals*, vol. 69, Feb. 2016. DOI: 10.1007/s12666-016-0841-8.

[44] F. Widerøe and T. Welo, "Using contrast material techniques to determine metal flow in screw extrusion of aluminium," *Journal of Materials Processing Technology*, vol. 213, no. 7, pp. 1007–1018, 2013, ISSN: 0924-0136. DOI: https://doi.org/10.1016/j.jmatprotec.2012.11.013. [Online]. Available: https://www.sciencedirect.com/science/article/pii/S092401361200338X.

[45] D. Baffari, G. Buffa, D. Campanella, and L. Fratini, "Al-sic metal matrix composite production through friction stir extrusion of aluminum chips," *Procedia Engineering*, vol. 207, pp. 419–424, 2017, International Conference on the Technology of Plasticity, ICTP 2017, 17-22 September 2017, Cambridge, United Kingdom, ISSN: 1877-7058. DOI: https://doi.org/10.1016/j.proeng.2017.10.798. [Online]. Available: https://www.sciencedirect.com/science/article/pii/S1877705817355753.

[46] K. Tahmasbi and M. Mahmoodi, "Evaluation of microstructure and mechanical properties of aluminum aa7022 produced by friction stir extrusion," *Journal of Manufacturing Processes*, vol. 32, pp. 151–159, 2018, ISSN: 1526-6125. DOI: https://doi.org/10.1016/j.jmapro.2018.02.008. [Online].

Available: https://www.sciencedirect.com/science/article/pii/S1526612518300501.

[47] D. Baffari, A. P. Reynolds, X. Li, and L. Fratini, "Influence of processing parameters and initial temper on friction stir extrusion of 2050 aluminum alloy," *Journal of Manufacturing Processes*, vol. 28, pp. 319–325, 2017, ISSN: 1526-6125. DOI: https://doi.org/10.1016/j.jmapro.2017.06.013. [Online]. Available: https://www.sciencedirect.com/science/article/pii/S1526612517301603.

[48] M. A. Ansari, M. Narvan, R. Behnagh, E. Sadeqzadeh, M. K. B. Givi, and H. Ding, "Optimization of friction stir extrusion (fse) parameters through taguchi technique," *Transactions - Indian Institute of Metals*, vol. 69, Aug. 2015. DOI: 10.1007/s12666-015-0686-6.

[49] R. A. Behnagh, R. Mahdavinejad, A. Yavari, M. Abdollahi, and M. Narvan, "Production of wire from AA7277 aluminum chips via friction-stir extrusion (FSE)," *Metallurgical and Materials Transactions B*, vol. 45, no. 4, pp. 1484–1489, 2014. DOI: 10.1007/s11663-014-0067-2. [Online]. Available: https://doi.org/10.1007%5C%2Fs11663-014-0067-2.

[50] W. Tang and A. Reynolds, "Production of wire via friction extrusion of aluminum alloy machining chips," *Journal of Materials Processing Technology*, vol. 210, no. 15, pp. 2231–2237, 2010, ISSN: 0924-0136. DOI: https://doi.org/10.1016/j.jmatprotec.2010.08.010. [Online]. Available: https://www.sciencedirect.com/science/article/pii/S0924013610002463.

[51] M. Abdollahi, R. A. Behnagh, J. Ghasemi, and M. K. B. Givi, "Solid-state recycling of aluminium alloy chips through friction stir extrusion (fse)," May 2014.

[52] D. Baffari, G. Buffa, and L. Fratini, "A numerical model for wire integrity prediction in friction stir extrusion of magnesium alloys," *Journal of Materials Processing Technology*, vol. 247, pp. 1–10, 2017, ISSN: 0924-0136. DOI: https://doi.org/10.1016/j.jmatprotec.2017.04.007. [Online]. Available: https://www.sciencedirect.com/science/article/pii/S0924013617301358.

[53] D. Baffari, G. Buffa, D. Campanella, and L. Fratini, "Design of continuous friction stir extrusion machines for metal chip recycling:

Issues and difficulties," *Procedia Manufacturing*, vol. 15, pp. 280–286, 2018, Proceedings of the 17th International Conference on Metal Forming METAL FORMING 2018 September 16 – 19, 2018, Loisir Hotel Toyohashi, Toyohashi, Japan, ISSN: 2351-9789. DOI: https://doi.org/10.1016/j.promfg.2018.07.220. [Online]. Available: https://www.sciencedirect.com/science/article/pii/S2351978918309120.

[54] D. Baffari, G. Buffa, D. Campanella, L. Fratini, and A. P. Reynolds, "Process mechanics in friction stir extrusion of magnesium alloys chips through experiments and numerical simulation," *Journal of Manufacturing Processes*, vol. 29, pp. 41–49, 2017, ISSN: 1526-6125. DOI: https://doi.org/10.1016/j.jmapro.2017.07.010. [Online]. Available: https://www.sciencedirect.com/science/article/pii/S1526612517301743.

[55] R. Griffiths, M. Perry, J. Sietins, *et al.*, "A perspective on solid-state additive manufacturing of aluminum matrix composites using meld," *Journal of Materials Engineering and Performance*, vol. 28, Sep. 2018. DOI: 10.1007/s11665-018-3649-3.

[56] J. K. Yoder, G. D. Hahn, N. Zhao, R. E. Brennan, K. Cho, and H. Z. Yu, "Additive friction stir deposition-enabled upcycling of automotive cast aluminum chips," *Additive Manufacturing Letters*, vol. 4, p. 100 108, 2023, ISSN: 2772-3690. DOI: https://doi.org/10.1016/j.addlet.2022.100108. [Online]. Available: https://www.sciencedirect.com/science/article/pii/S2772369022000755.

[57] G. Chen, K. Wu, Y. Wang, Z.-X. Zhu, P. Nie, and F.-F. Hu, "Effect of rotational speed and feed rate on microstructure and mechanical properties of 6061 aluminum alloy manufactured by additive friction stir deposition," Sep. 2022. DOI: 10.21203/rs.3.rs-2107596/v1.

[58] S. Babaniaris, L. Jiang, R. K. Varma, *et al.*, "Precipitation in aa6063 produced from swarf using additive friction stir deposition," *Additive Manufacturing Letters*, vol. 3, p. 100 096, 2022, ISSN: 2772-3690. DOI: https://doi.org/10.1016/j.addlet.2022.100096. [Online]. Available: https://www.sciencedirect.com/science/article/pii/S2772369022000639.

[59] H. Dong, X. Li, K. Xu, *et al.*, "A review on solid-state-based additive friction stir deposition," *Aerospace*, vol. 9, no. 10, 2022, ISSN: 2226-4310. DOI: 10.3390/aerospace9100565. [Online]. Available: https://www.mdpi.com/2226-4310/9/10/565.

[60] H. Chena, X. Menga, J. Chena, *et al.*, "Wire-based friction stir additive manufacturing," *Mechanical Engineering eJournal*, DOI: http://dx.doi.org/10.2139/ssrn.4296882. [Online]. Available: https://ssrn.com/abstract=4296882.

[61] H. Z. Yu and R. S. Mishra, "Additive friction stir deposition: A deformation processing route to metal additive manufacturing," *Materials Research Letters*, vol. 9, no. 2, pp. 71–83, 2021. DOI: 10.1080/21663831.2020.1847211. eprint: https://doi.org/10.1080/21663831.2020.1847211. [Online]. Available: https://doi.org/10.1080/21663831.2020.1847211.

[62] R. J. Griffiths, D. T. Petersen, D. Garcia, and H. Z. Yu, "Additive friction stir-enabled solid-state additive manufacturing for the repair of 7075 aluminum alloy," *Applied Sciences*, vol. 9, no. 17, 2019, ISSN: 2076-3417. DOI: 10.3390/app9173486. [Online]. Available: https://www.mdpi.com/2076-3417/9/17/3486.

[63] *Aluminium, 6060, t6*, Database.

[64] F. Servigna, *Understanding aluminum corrosion*, 2019. [Online]. Available: https://www.corrosionpedia.com/understanding-aluminum-corrosion/2/6954.

[65] Y. Kim, H. Fujii, T. Tsumura, T. Komazaki, and K. Nakata, "Three defect types in friction stir welding of aluminum die casting alloy," *Materials Science and Engineering: A*, vol. 415, no. 1, pp. 250–254, 2006, ISSN: 0921-5093. DOI: https://doi.org/10.1016/j.msea.2005.09.072. [Online]. Available: https://www.sciencedirect.com/science/article/pii/S0921509305011652.

[66] D. Liu, H. Atkinson, P. Kapranos, W. Jirattiticharoean, and H. Jones, "Microstructural evolution and tensile mechanical properties of thixoformed high performance aluminium alloys," *Materials Science and Engineering: A*, vol. 361, no. 1, pp. 213–224, 2003, ISSN: 0921-5093. DOI: https://doi.org/10.1016/S0921-5093(03)00528-8. [Online]. Available: https://www.sciencedirect.com/science/article/pii/S0921509303005288.

[67] E. Pink, S. Kumar, and B. Tian, "Serrated flow of aluminium alloys influenced by precipitates," *Materials Science and Engineering: A*, vol. 280, no. 1, pp. 17–24, 2000, ISSN: 0921-5093. DOI: https://doi.org/10.1016/S0921-5093(99)00650-4. [Online]. Available: https://www.sciencedirect.com/science/article/pii/S0921509399006504.

[68] J. Brechtl, S. Chen, X. Xie, *et al.*, "Towards a greater understanding of serrated flows in an al-containing high-entropy-based alloy," *International Journal of Plasticity*, vol. 115, pp. 71–92, 2019, ISSN: 0749-6419. DOI: https://doi.org/10.1016/j.ijplas.2018.11.011. [Online]. Available: https://www.sciencedirect.com/science/article/pii/S0749641918303140.

[69] R. Islam, A. Hadadzadeh, M. Wells, and M. Haghshenas, "Characterization and analysis of hot compression behaviors of an ultralight mg-li-al alloy," *International Journal of Lightweight Materials and Manufacture*, vol. 2, Apr. 2019. DOI: 10.1016/j.ijlmm.2019.04.004.

[70] F. Chmelıék, E. Pink, J. Krol, J. Balıék, J. Pesicka, and P. Lukac, "Mechanisms of serrated flow in aluminium alloys with precipitates investigated by acoustic emission," *Acta Materialia*, vol. 46, no. 12, pp. 4435–4442, 1998. DOI: https://doi.org/10.1016/S1359-6454(98)00070-6.

[71] B. Tian, "Ageing effect on serrated flow in al–mg alloys," *Materials Science and Engineering: A*, vol. 349, no. 1, pp. 272–278, 2003, ISSN: 0921-5093. DOI: https://doi.org/10.1016/S0921-5093(02)00769-4. [Online]. Available: https://www.sciencedirect.com/science/article/pii/S0921509302007694.

[72] K. Prasad, R. Sarkar, D. P. Ghosal, and V. Kumar, "Effects of strain waveform on low cycle fatigue behaviour of near α timetal 834 titanium alloy," *Materials & Design - MATER DESIGN*, vol. 32, pp. 1710–1715, Mar. 2011. DOI: 10.1016/j.matdes.2010.08.044.

Appendix A

Experimental overview

Multiple experiments were performed without success, as can be seen in Table A.1. However, some important changes to the setup were performed, which is why they are documented in this appendix. An overview of the changes and what went wrong during the experiments is given as well. The S- and E-series, which are not further elaborated, did not encounter a setup change.

- **Experiment S1**
  Cooling block was not fixed in place and came loose during the process. This caused a forced stop of the experiment.
- **Experiment E1**
  In the last layer the build came loose from the substrate. Since is was the last layer the build could still be reviewed. The start-up procedure was changed to create a larger surface area in which the build can bond to the substrate. This results in the bottom 4 layers now being $\pm\ 5\,\mathrm{cm}$ longer.
- **Experiment F1**
  The experiment failed during the start up phase. The problem occurred in the feedtube due to a blockade. It is suggested that the cause of the problem was prematurely softening of the feedstock, which can be solved by using a higher cooling rate for the feedtube.

Table A.1: Overview of all performed experiments

Name	Date (y\m\d)	Table speed (mm/min)	Feed rate mm/sec	Key	Cooling rate Feedtube (L/min)	Cooling rate Nozzle (L/min)	Fail/ Success
S1	22/02/01	50-430	0.226-1.946	2-5.8	Unknown	Unknown	Fail
E1	22/03/09	100	0.453	2.8	Unknown	Unknown	Fail
F1	22/03/23	-	-	-	Unknown	Unknown	Fail
F2	22/03/30	200	0.950	4.0	Unknown	Unknown	Fail
F3	22/05/03	Extrusion	0.226	2.0	Unknown	Unknown	Fail
F4	22/05/12	Extrusion	0.226	2.0	Unknown	Unknown	Fail
F5	22/05/31	210	0.950	4.0	7.1	1.8	Fail
F6	22/06/16	200	0.950	4.0	6.8	2.2	Fail
F7	22/06/16	150	0.685	3.5	6.8	2.2	Fail
E2	22/07/20	150	0.685	3.5	3.5	2.3	Success
E3	22/07/27	200	0.950	4.0	3.5	2.5	Success
E4	22/07/27	250	1.154	4.5	3.5	2.5	Success
S2	22/08/19	300	1.354	4.9	3.6	2.5	Success
S3	22/08/19	350	1.575	5.3	3.6	2.5	Success
S4	22/08/23	400	1.810	5.6	3.5	2.5	Success
S5	22/08/23	450	2.036	5.9	3.5	2.5	Success
S6	22/08/23	500	2.218	7	3.5	2.5	Success

- **Experiment F2**
  The experiment failed during the start up phase. The suggested problem was the high extrusion force. A possible explanation could be a too high cooling rate of the nozzle. To check the cooling rate in later experiments, flow meters are added to the system afterwards.
- **Experiment F3 & F4**
  Extrusion experiments with AA7075 were performed for another research. During experiment F4 the system got blocked and the screw and nozzle got stuck in the print head. For the next experiment both a new nozzle and screw where used.
- **Experiment F5**
  The experiment failed during the start up phase. The problem occurred in the feedtube due to a blockade. It is suggested that the cause of the problem was prematurely softening of the feedstock. Since the cooling rate of the feedtube was much higher than

previous the reason for this softening has to be found somewhere else. A closer look at the new manufactured nozzle showed a different geometry, causing a smaller toolgap, and explained the rise in temperature, force, and torque. For the next experiment, the toolgap will be brought back to $3.2\,\mathrm{mm}$ by adjusting the geometry of the nozzle.

- **Experiment F6**
  The experiment failed due to too high vertical forces. The material feed was not stopped while the table did not move causing a rise in vertical force. Due to these high forces, the table could not move anymore and the experiment had to be stopped.

- **Experiment F7**
  The experiment failed due to too a power outage causing the systems to stop. Afterwards the feedtube was examined. Since it had a diameter of $8.5\,\mathrm{mm}$ instead of the original $8.1\,\mathrm{mm}$, probably due to wear over time, it was replaced.

Appendix B

Process parameters

The in-situ measurement taken during the builds are depicted in the following Figures. If one of the thermocouples mentioned in Section 3.1.4 is not assigned, it broke during assembly or in the experiment.

B.1 E1 - 100 mm/min, 400 RPM

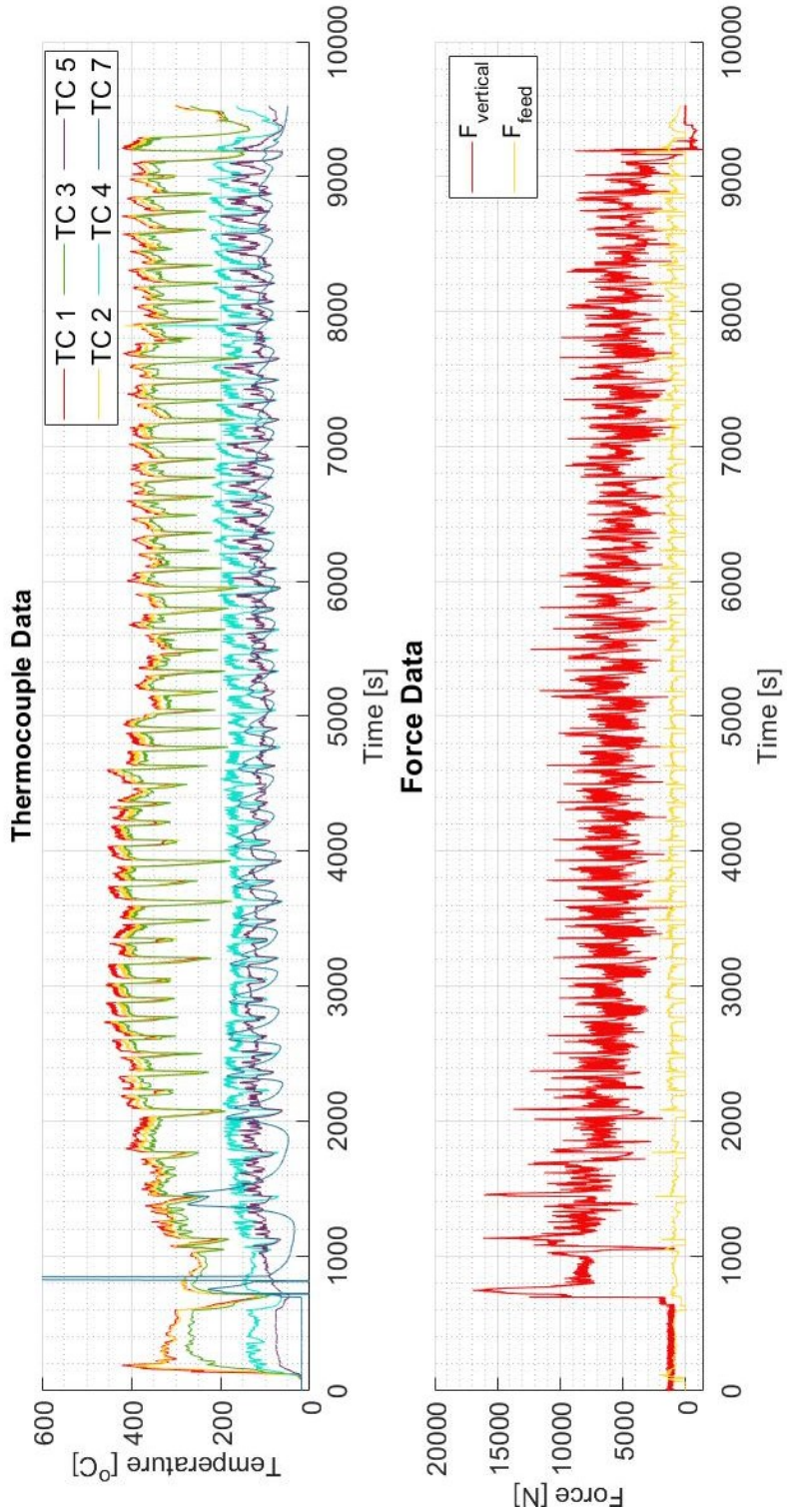

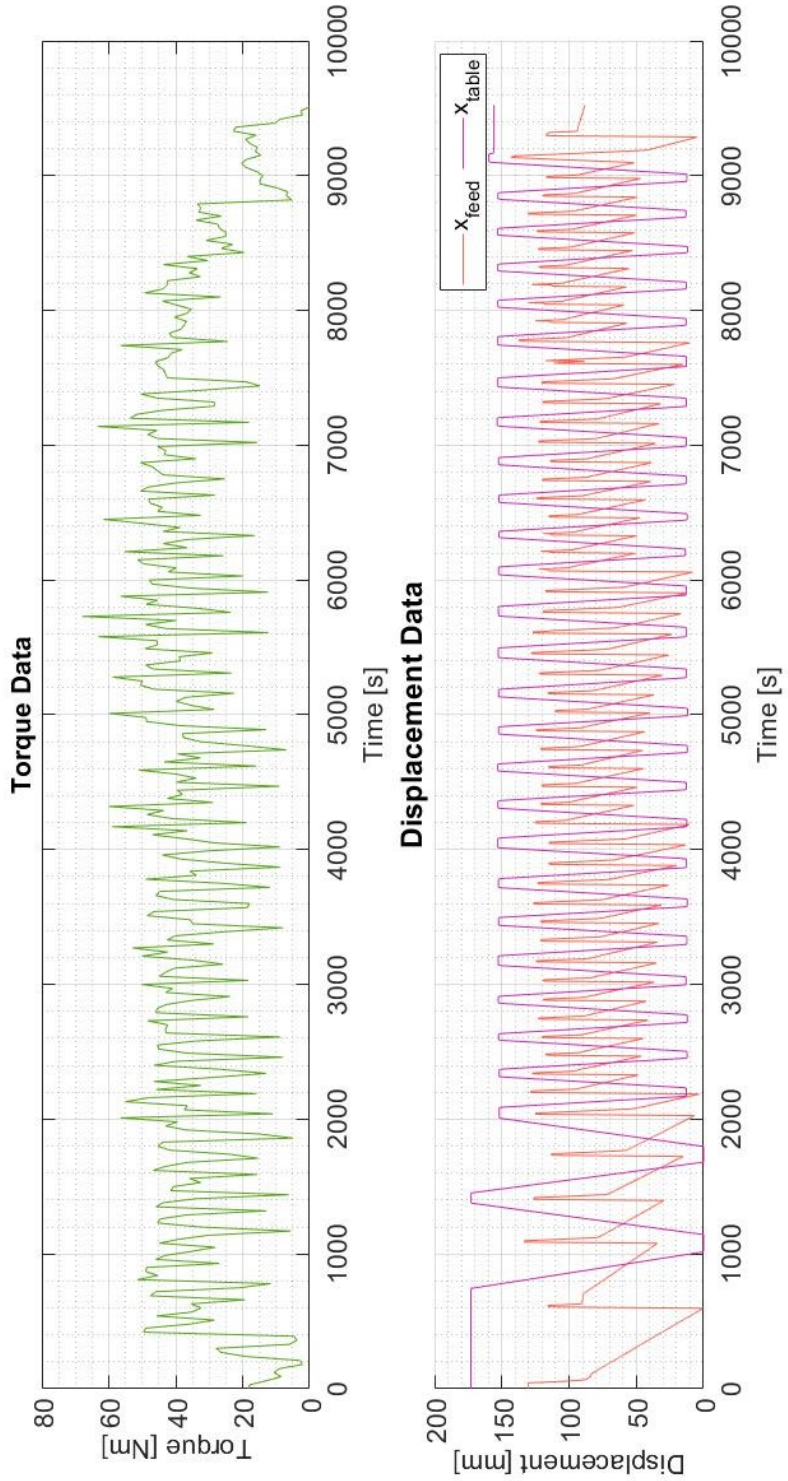
Torque Data
Torque [Nm]
0
20
40
60
80
0
1000
2000
3000
4000
5000
6000
7000
8000
9000
10000
Time [s]
Displacement Data
Displacement [mm]
0
50
100
150
200
x_{feed}
x_{table}
Time [s]

B.2 E2 - 150 mm/min, 400 RPM

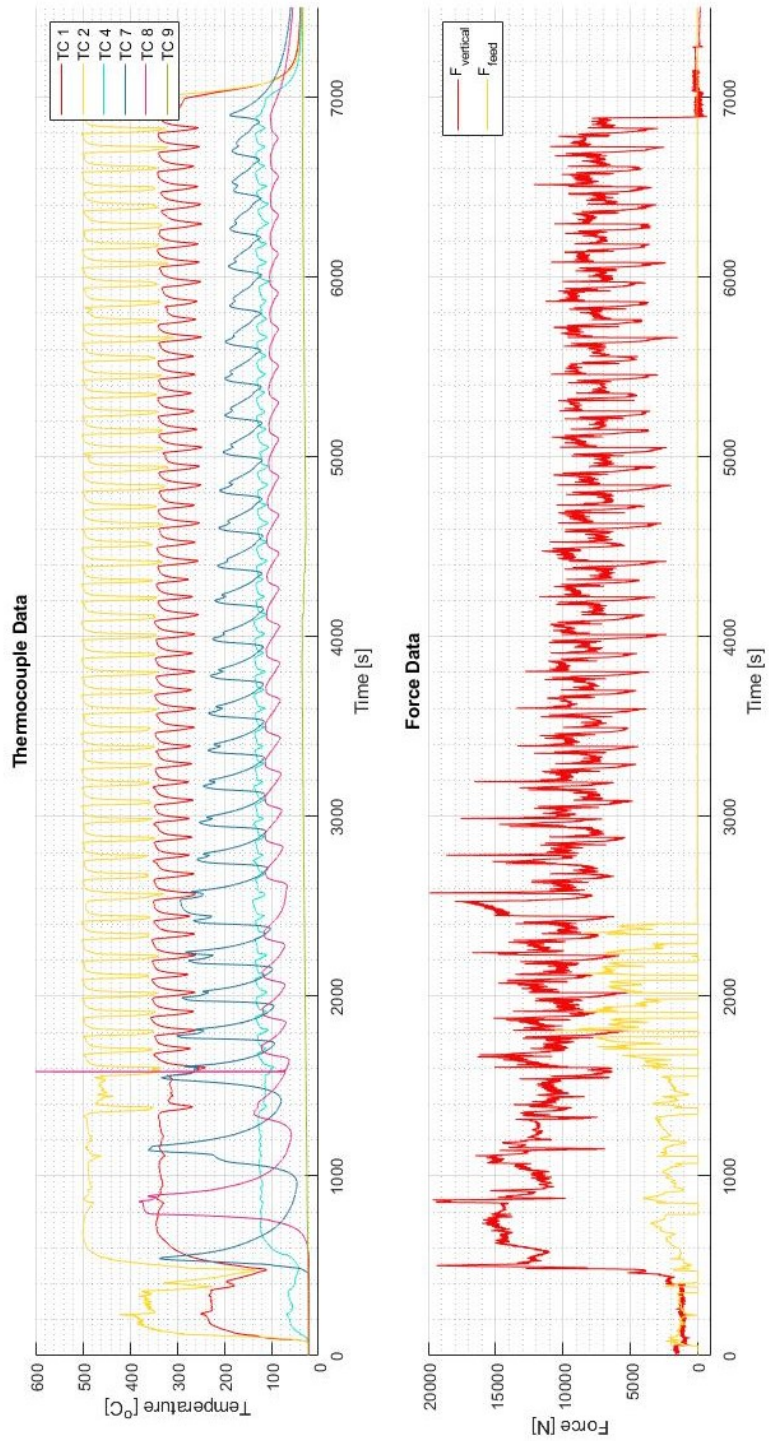

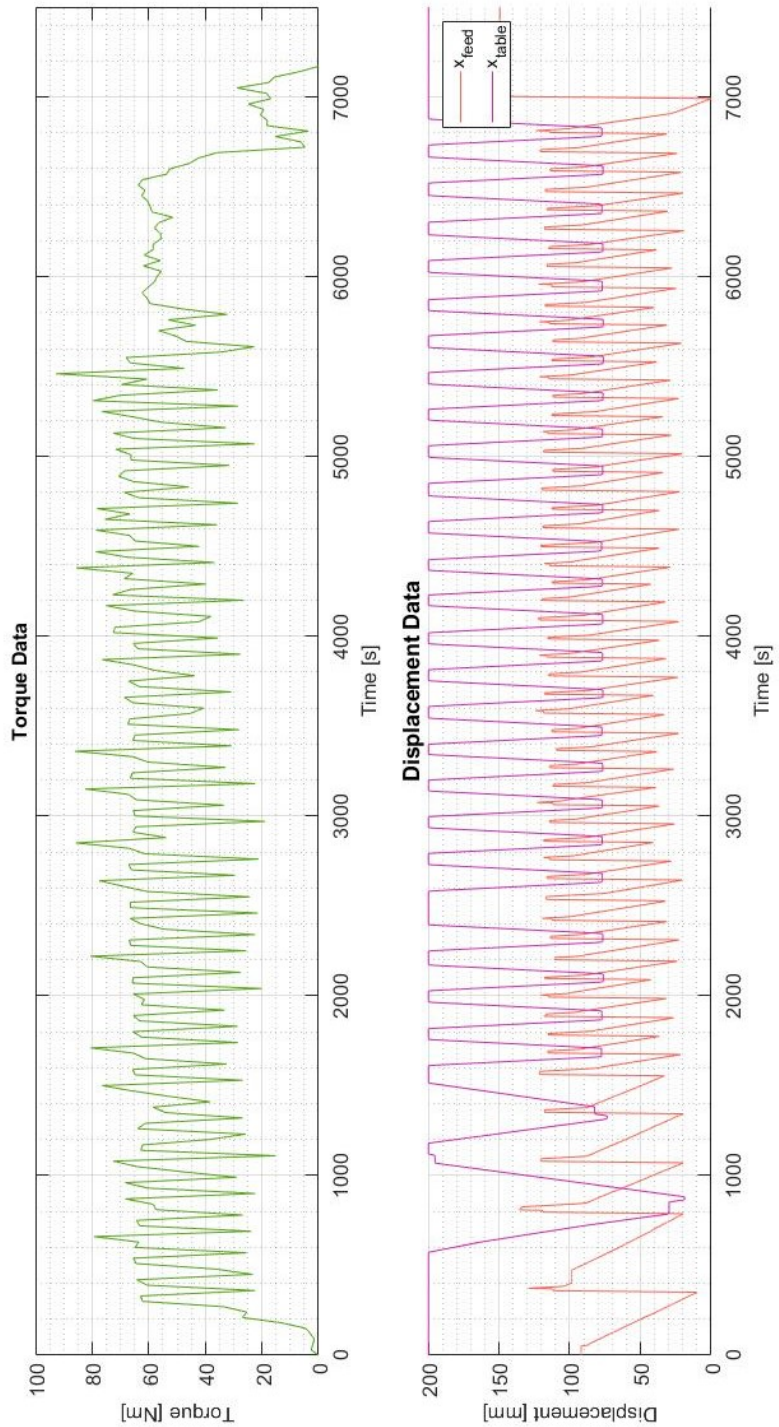
Torque Data
Torque [Nm]
Time [s]
Displacement Data
Displacement [mm]
Time [s]
x_{feed}
x_{table}

B.3 E3 - 200 mm/min, 400 RPM

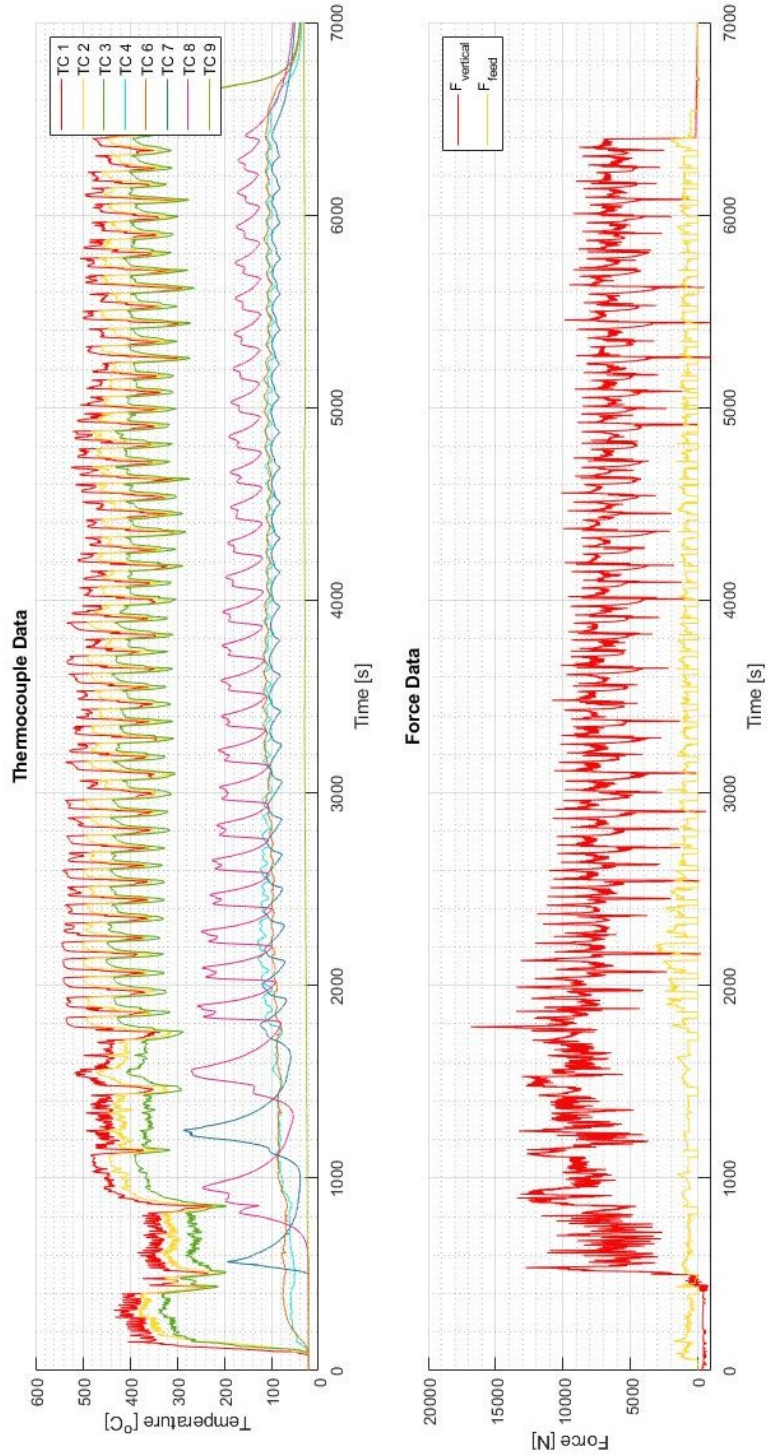

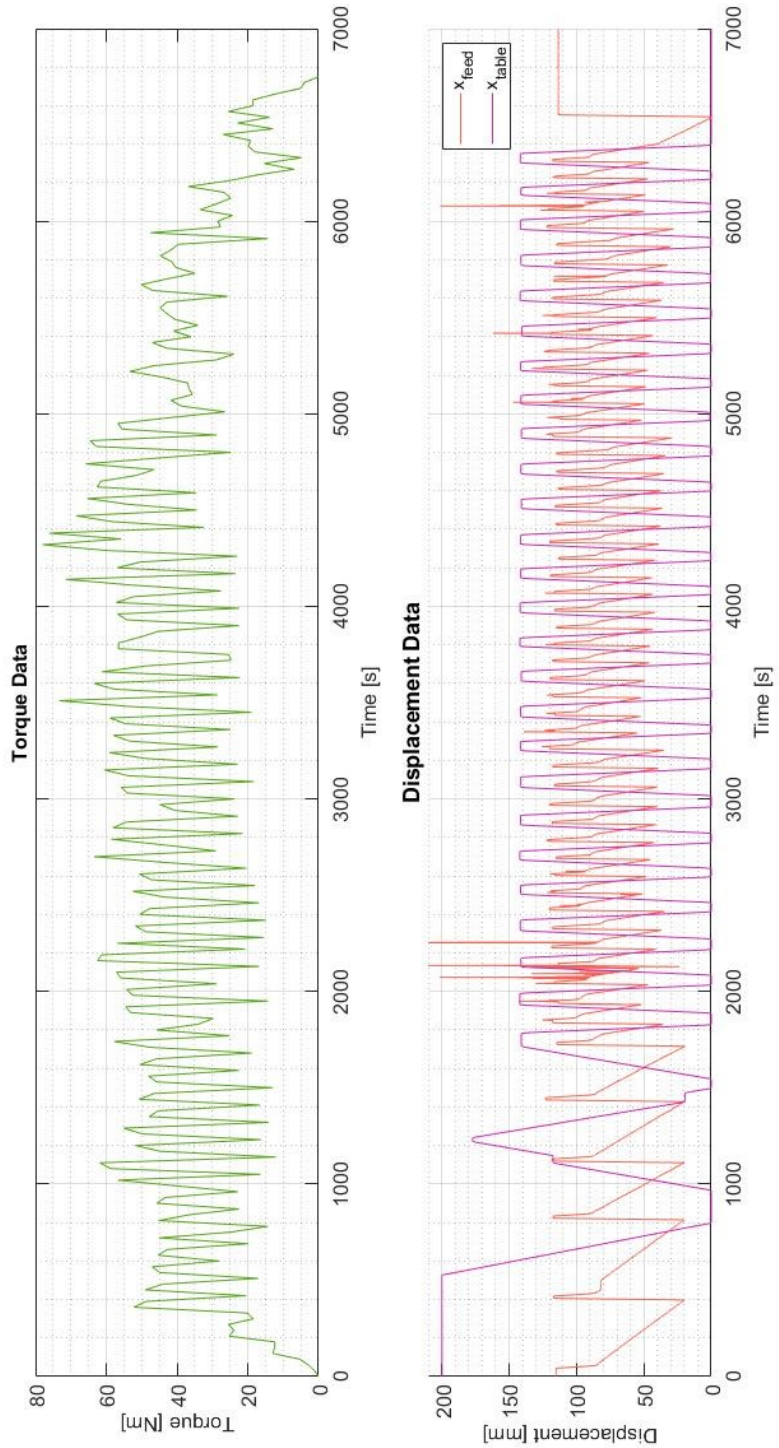
Torque Data
Torque [Nm]
Time [s]
Displacement Data
Displacement [mm]
Time [s]
x_feed
x_table

B.4 E4 - 250 mm/min, 400 RPM

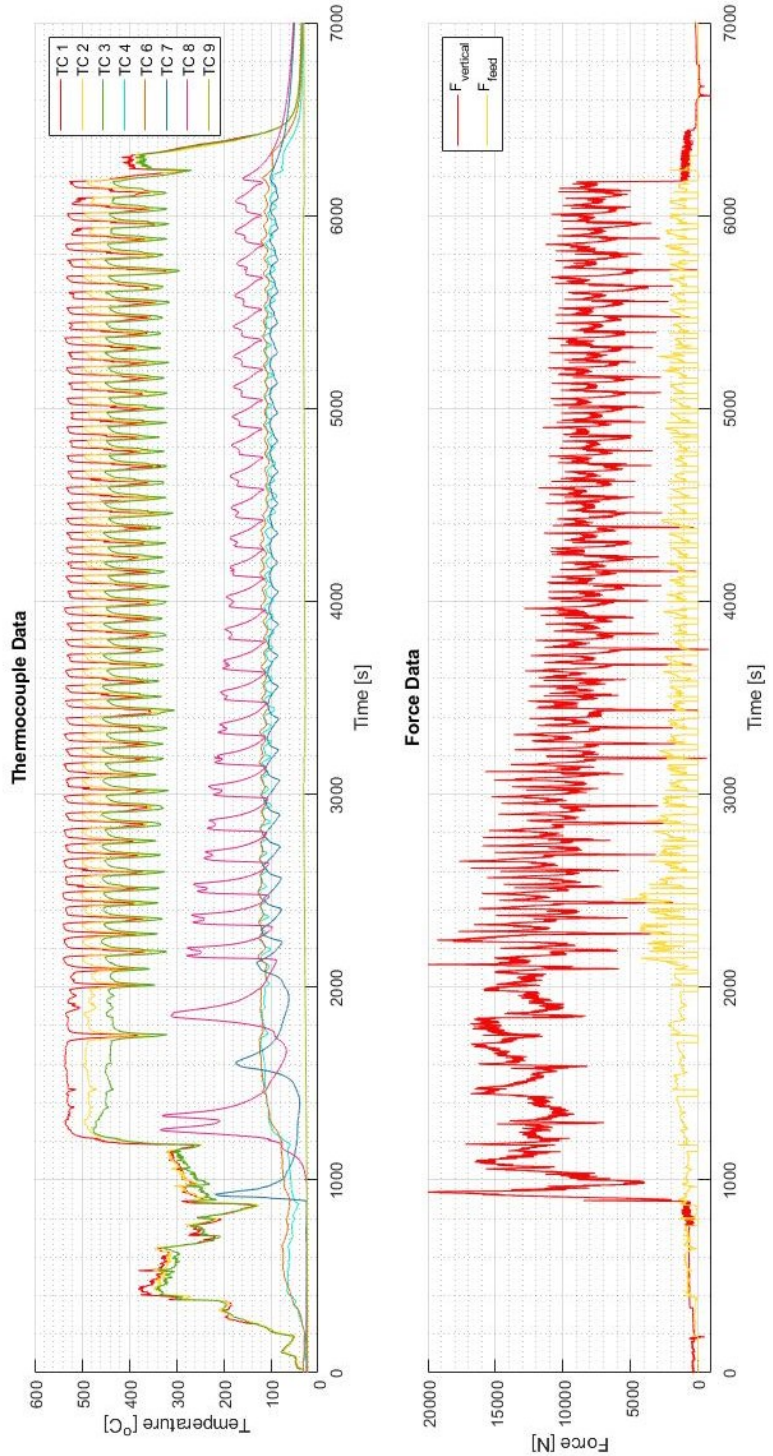

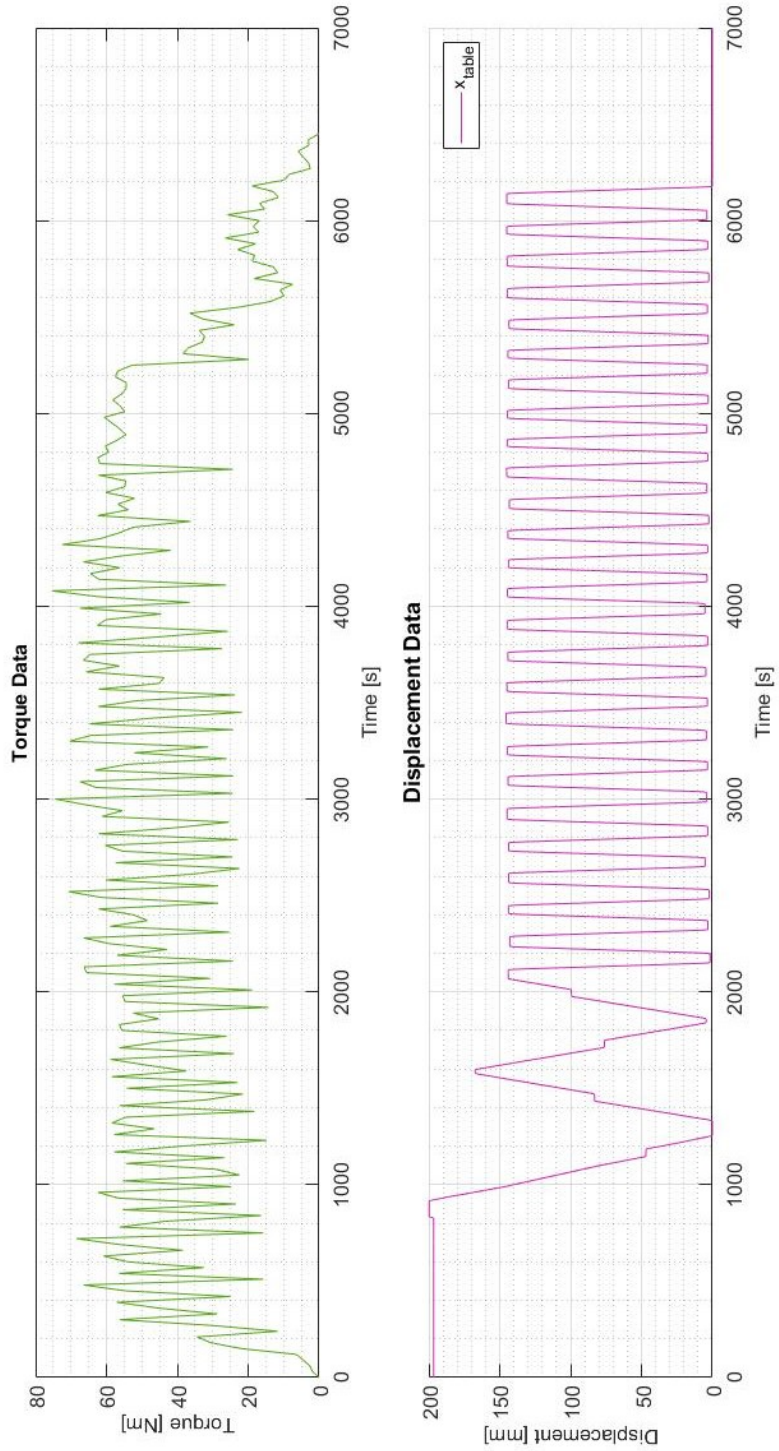
Torque Data
Torque [Nm]
Time [s]
Displacement Data
Displacement [mm]
Time [s]
x_table

Appendix C

Grain size distribution per experiment

C.1 E1 - 100 mm/min, 400 RPM

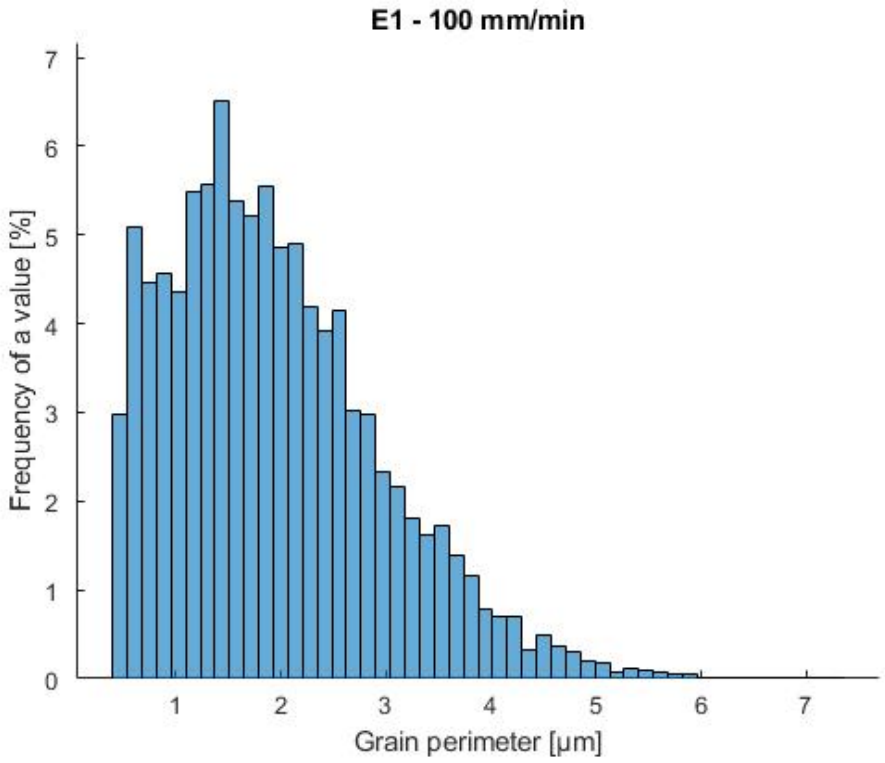

C.2 E2 - 150 mm/min, 400 RPM

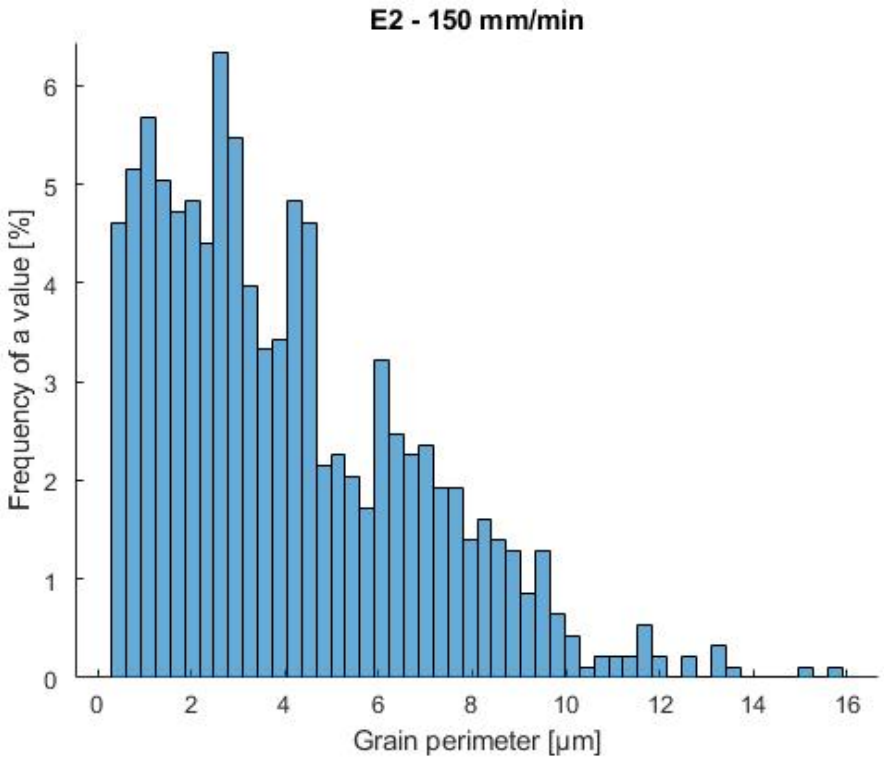

C.3 E3 - 200 mm/min, 400 RPM

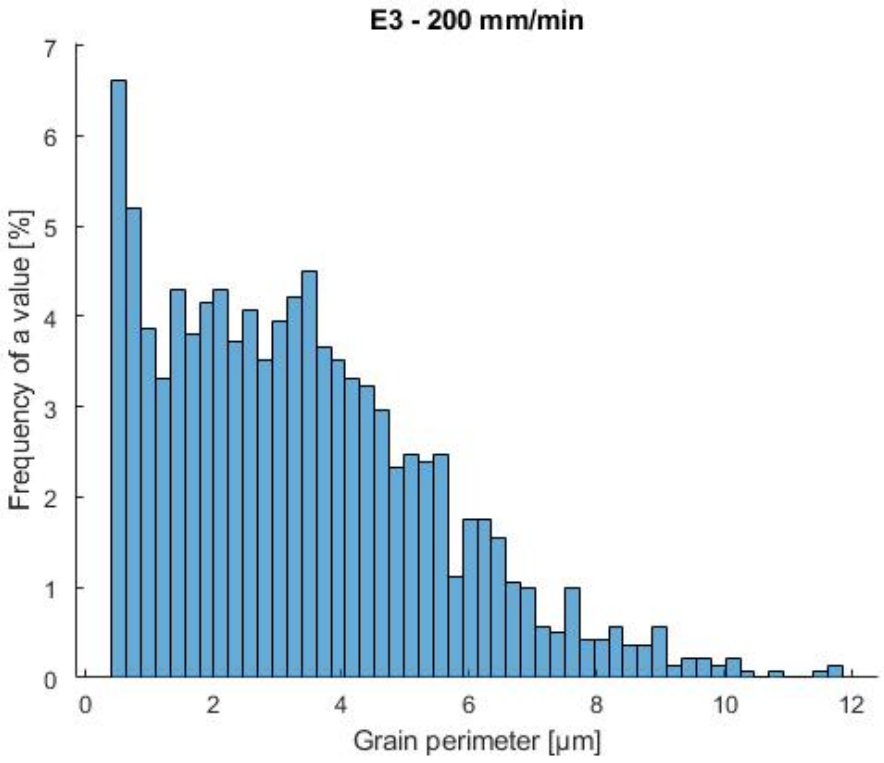

C.4 E4 - 250 mm/min, 400 RPM

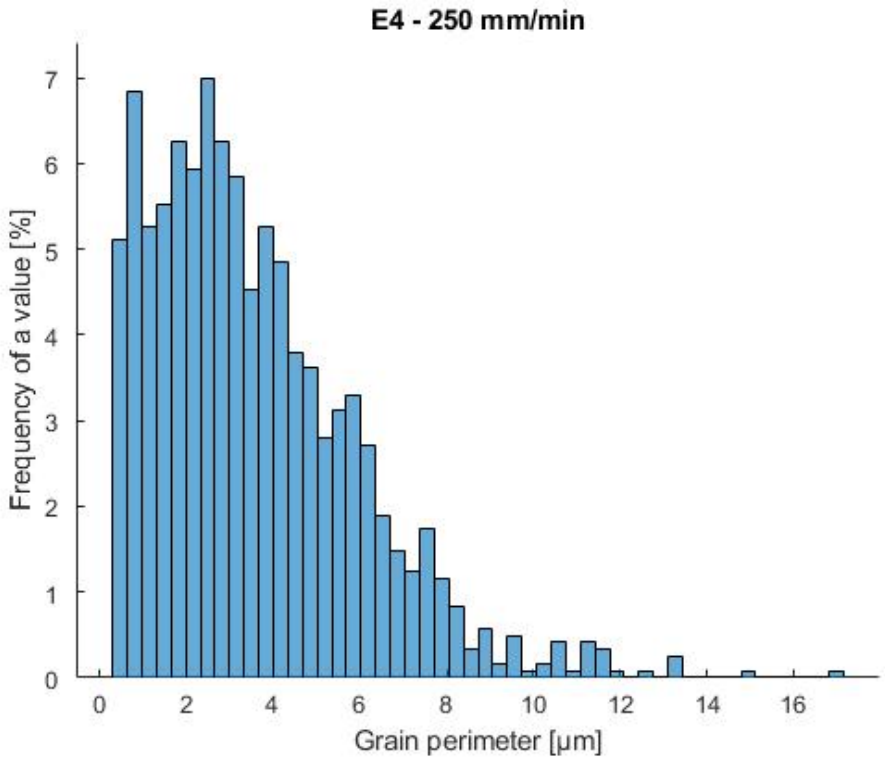

Appendix D

Error estimation models

To check whether the model is a good approximation of reality, two error approximations are made and discussed down below. For these approximations some values for the material properties are necessary, which can be found in Table D.1.

Table D.1: Properties used for error approximations

h_{air}	$10\,\mathrm{W/m^2K}$
λ_{AA6060}	$210\,\mathrm{W/mK}$
ρ_{AA6060}	$2700\,\mathrm{kg/m^3}$
$c_{pAA6060}$	$900\,\mathrm{J/kgK}$

D.1 Thermal penetration depth

First the thermal penetration depth is evaluated. The exact solution is given for a one-sided infinite system. Here, a solid aluminium block of AA6060. For which at t_0 the temperature of the build is at the uniform temperature T_0 and one side is at T_{wall}. All the other sides are fully insulated, as can be seen in Figure D.1a.

Since this is a one dimensional problem, the heat equation of the system becomes D.1. Furthermore, the initial and boundary conditions are prescribed to the system.

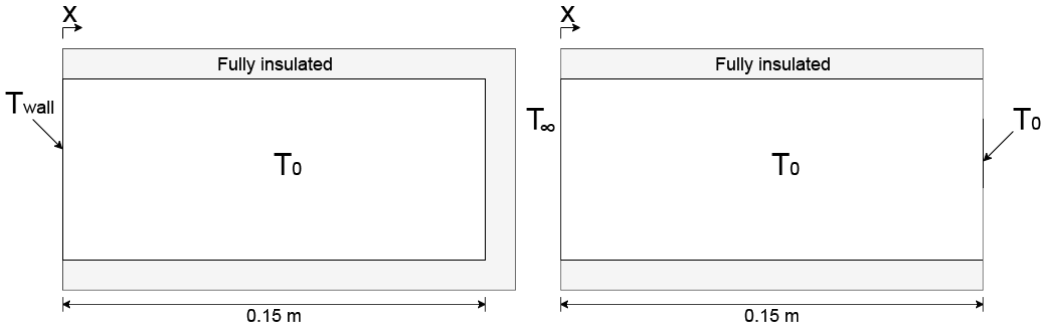

(a) Thermal penetration depth check *(b)* Stable convection check

Figure D.1: Boundary and initial conditions of the error estimation models at t=0

$$\begin{gathered} \frac{\partial T}{\partial t} = \frac{\lambda}{\rho c_p} \frac{\partial^2 T}{\partial x^2} \\ with \\ x = 0,\ T = T_{wall}\ for\ t > 0 \\ x = \infty,\ T = T_0\ for\ t > 0 \\ t = 0,\ T = T_0\ for\ all\ x \end{gathered} \tag{D.1}$$

Solving the system with respect to the conditions results in D.2. In which erf is the standard error integral. Once plotted and compared with the model, the error can be examined in Figure D.2. Three models are plotted with a varying step size in the x-direction, the exact solution, and its slope are plotted for 1000 time steps. All values used for the error estimation can be found in Table D.2. It can be seen that the modeled systems are close to the exact solution and that they converge for a smaller step size, indicating a good approximation.

$$T(x,t) = T_{wall} - (T_{wall} - T_0) erf(\frac{x}{2\sqrt{\frac{\lambda}{\rho c_p} t}}) \tag{D.2}$$

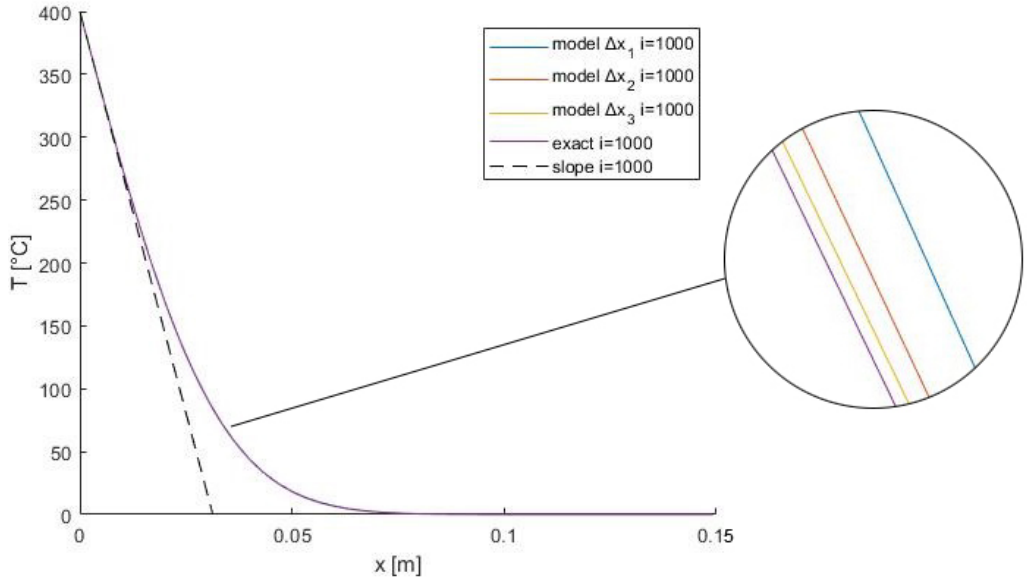

Figure D.2: Error evaluation thermal penetration depth theory

D.2 Convection check

Next, the boundary condition described to the system is evaluated. Again, the system starts at an initial temperature T_0, where the right side is kept constant at this temperature while the left side is cooled via convection with a room temperature of T_{inf}. The top and bottom wall are both fully insulated, an overview is given in Figure D.1b.

$$T_{wall} = T_{inf} + \frac{T_0 - T_{inf}}{\frac{\Delta x * h}{\lambda} + 1} \tag{D.3}$$

The computation is compared to the exact solution of a time independent problem (Equation D.3). Therefore, the duration of the simulation is set to approximately$1\,\mathrm{h}$ to simulate a time independent problem. All the values of the model can be found in Tables D.2 and D.1. As seen in Figure D.3, the model gives a close resemblance of the exact solution and converges

Table D.2: Variable data used in the models

	thermal penetration depth	stable convection
T_0 [°C]	0	400
T_{wall} [°C]	400	-
T_∞ [°C]	-	18
Δx_1 [m]	0.0033	0.0033
Δx_2 [m]	0.0017	0.0017
Δx_3 [m]	8.3333e-04	8.3333e-04
Δt [sec]	0.0036	0.0036

after a grid refinement. Again, indicating a good approximation.

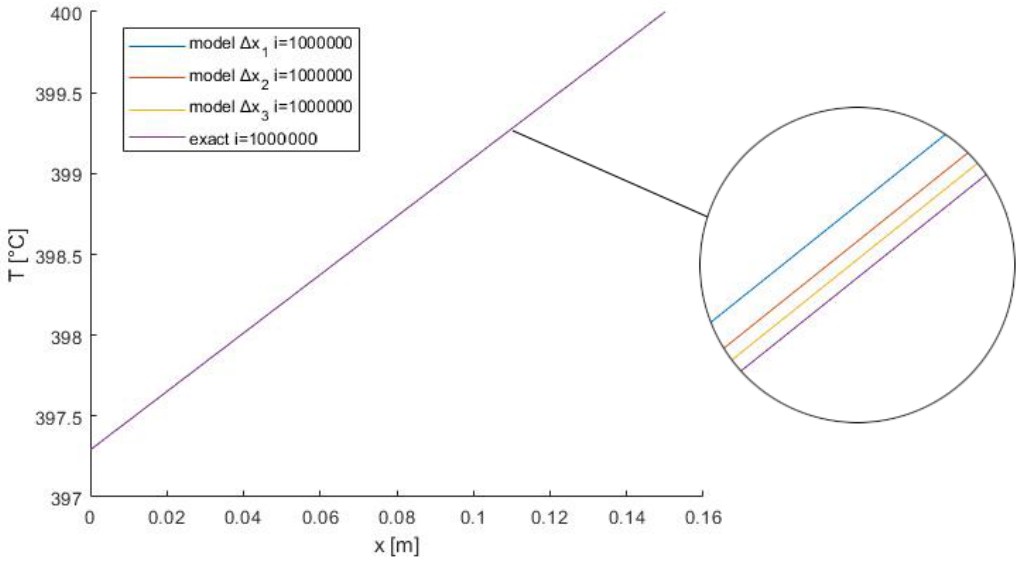

Figure D.3: Error evaluation convection boundary condition